Anisotropy and polarization effects in blazar emission

M Tisang

orcid.org 0000-0003-1588-1448

Dissertation accepted in partial fulfilment of the requirements for the degree *Master of Science in Astrophysical Sciences* at the North-West University

Supervisor: Prof M Böttcher

Graduation October 2023

27709167

Acknowledgements

I would like to sincerely praise and thank The Almighty God for making it all possible and for granting me the privilege to study under the guidance of Professor Markus Böttcher, a scientist affiliated with North-West University (NWU).

My heartiest thanks to Prof. Böttcher, my study leader and a distinguished leader among leaders, who believed, than I did, that I could successfully accomplish this study. Many thanks for his clear and patient guidance, as well as his unwavering support towards the completion of this study. Whenever I needed his help, he was always reachable and approachable and would give me a clear way forward. Prof. Böttcher serves as a remarkable role model who has inspired me to further my studies, and I am looking forward to continuing working with him. I could not have desired a better study leader. Most importantly, I am grateful for his understanding of my difficult situations during the pandemic, and I have benefited a lot from his positive attitude, enthusiasm, and vigorous energy.

I would like to thank Hester Schutte (an NWU ph.D student) and Ms Elanie van Rooyen (an NWU physics department staff member) for their assistance with some of the Python code and with my Turnitin report, respectively. Ms. van Rooyen ensured that I received my dissertation's Turnitin report on time, which alleviated my concerns and prevented any more worries.

Moreover, I express my sincere gratitude to the National Astrophysics and Space Science Programme (NASSP), the Centre for Space Research (CSR), and the NWU for their generous financial support.

Additionally, many thanks to my family (and friends) for being supportive when I needed them the most. I am truly humbled by the sacrifices they made so that I could pursue my educational journey.

Abstract

Blazars are radio-loud (RL) active galactic nuclei (AGNs) whose relativistic jets are directed at us. These sources are observed to have spectral energy distributions (SEDs) with two broad-humped components, significant variability throughout the electromagnetic (EM) spectrum, and high average polarization degrees (PDs) from radio to optical energy bands. This study constitutes the first step towards the development of a full angle- and polarization-dependent synchrotron and synchrotron self-Compton (SSC) blazar multi-wavelength emission model with relativistic electrons in a uniform magnetic field.

Using the code developed in this work, we simulate different orientations of the magnetic field w.r.t. the jet axis (such as parallel, perpendicular, and oblique field geometries) that may exist within a blazar jet, as well as different viewing angles relative to the jet axis, and study the impact on the synchrotron and SSC spectra and multi-wavelength polarization. We also report on the impacts of varying the electron power-law index on the synchrotron and SSC emission.

The results of this study demonstrate that, as expected, the synchrotron emission is dramatically affected by variations of both the magnetic field orientation and our line of sight (LoS) w.r.t. the jet axis, whereas the SSC emission is almost independent of them. This is evident, especially in an oblique magnetic field case, where synchrotron emission is substantially suppressed when our LoS and the magnetic field vector are closely aligned. On the other hand, in this field case, SSC emission shows a significant dependence on the magnetic field azimuthal angle. Furthermore, we demonstrate that, as the electron power-law index increases, the SSC emission becomes suppressed, whereas the average PD rises as well.

Keywords: generic blazar; linear polarization; magnetic field orientation; anisotropic synchrotron photon; nonthermal radiative mechanisms

Contents

List of Figures

List of Tables

Table of abbreviations

AGN	Active Galactic Nucleus
BH	Black Hole
BLR	Broad Line Region
BLRGs	Broad Line Radio Galaxies
Cen A	Centaurus A
EM	Electromagnetic
ERF	Electron-rest Frame
FRI	Fanaroff-Riley Type I
FRII	Fanaroff-Riley Type II
FSRQ	Flat Spectrum Radio Quasar
FWHM	Full Width at Half Maximum
HBL	High-sychrotron-peaked BL Lac object
HE	High-Energy
H.E.S.S.	High Energy Stereoscopic System
IACT	Imaging Atmospheric Cherenkov Telescope
IBL	Intermediate-synchrotron-peaked BL Lac object
IC	Inverse Compton
IR	In-frared
KN	Klein-Nishina
LBL	Low-synchrotron-peaked BL Lac object
LE	Low-Energy
LHS	Left-Hand-Side
LoS	Line of Sight
LSP	Low-synchrotron-peaked
MAGIC	Major Atmospheric Gamma Imaging Cherenkov
NLR	Narrow Line Region
NLRGs	Narrow Line Radio Galaxies
PA	Polarization Angle
PD	Polarization Degree
QSO	Quasi-Stellar Object
RHS	Right-Hand-Side

RGs	Radio Galaxies
RL	Radio Loud
RQ	Radio Quiet
SED	Spectral Energy Distribution
SMBH	Supermassive Black Hole
SSC	Sychrotron Self-Compton
SSRQ	Steep Spectrum Radio Quasar
UV	Ultraviolet
VERITAS	Very Energetic Imaging Telescope Array System
VHE	Very High Energy

Chapter 1

Introduction

Blazars are the most intense class of radio-loud active galactic nuclei (AGNs) that are jet-dominated, consisting of flat-spectrum radio quasars (FSRQs) and BL Lac objects. They show characteristic double-hump-shaped spectral energy distributions (SEDs), strong variability over the whole electromagnetic (EM) spectrum, and high degrees of polarization observed from radio through optical bands. Such radiation arises from relativistic jets produced by supermassive black holes (SMBHs) within the central engines of AGNs.

This chapter gives a brief discussion of AGN. The two populations of AGN, namely, radio-quiet (RQ) and radio-loud (RL) AGNs, will also be discussed with special attention to blazars. The focus of the thesis will then be introduced with previous related work. It closes with a problem statement, research goal, and the outline of the thesis.

1.1 Active Galactic Nuclei

AGNs are effectively accreting SMBHs within galactic cores. These objects emit enormous amounts of non-thermal radiation across the multi-wavelength bands. The galaxies hosting AGNs are said to be active galaxies. Active galaxies are extremely bright compared to inactive galaxies, galaxies powered by starlight (Padmanabhan, 2002; Schneider, 2006). The Milky Way, the galaxy that we live in, is one of those inactive galaxies. In addition to this feature, there are other observational features such as broad non-thermal radiation, high variability on a large range of timescales, high polarization in different wavebands, and strong, broad emission lines including semi-prohibited and prohibited emission lines that can as well differentiate AGNs from inactive galaxies, (Padmanabhan, 2002):

- **High Luminosity:** The luminosities of active galaxies, spanning from roughly 10^{42} erg·s^{-1} to roughly 10^{48} erg·s^{-1} (Padmanabhan, 2002), are more prominent than the luminosities of inactive galaxies. Since a typical inactive galaxy has a luminosity of about 10^{44} erg·s^{-1}, AGN can therefore be as high as 10,000 times brighter than all the stars in an inactive galaxy (Padmanabhan, 2002; Schneider, 2006).

- **Broad Non-thermal Radiation:** AGNs emit intense radiation of non-thermal origin within the radio, infrared (IR), optical, ultraviolet (UV), X-ray, and gamma-ray bands (Schneider, 2006; Urry and Padovani, 1995). This means that AGNs are observable through all wavelength (from gamma-ray to radio) bands (see Figure 1.1). Figure 1.2 shows images of the radio galaxy NGC 5128, known as Centaurus A (Cen A), in different wavelength bands. It tells how a single-band observation can provide insufficient information about an AGN.

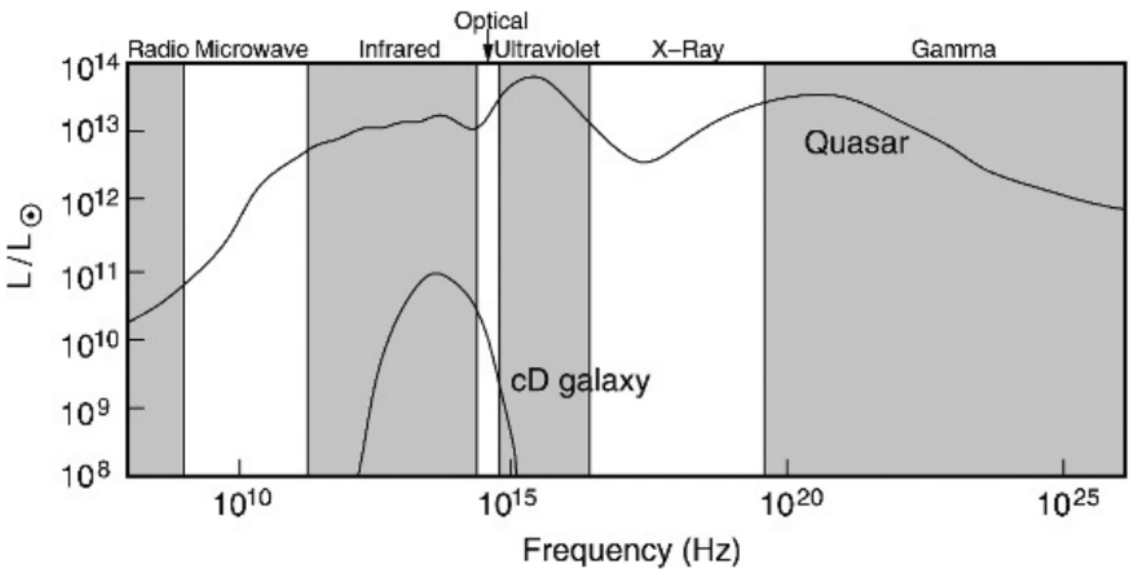

Figure 1.1: The spectra of the quasar 3C 273 and the cD galaxy, an elliptical galaxy. The radiation of the quasar spans the entire EM spectrum, whereas the elliptical galaxy emission is observed in a narrow range from infrared to ultraviolet. The plot is taken from Schneider (2006).

- **Emission Lines:** The optical spectrum of an AGN can display two types of emission lines, namely, broad and narrow emission lines. However, it is sometimes possible for the spectrum not to show any emission lines.

  Figure 1.3 demonstrates the average spectrum of quasars showing a variety of emission lines such as broad permitted lines (Lyα, CIV, MgII, Hδ, Hγ, and Hβ), semi-forbidden lines (CIII] and CII]), and narrow forbidden lines (Si[V/OIV], [NeV], [OII], [NeIII], and [OIII]). The square bracket(s) implies

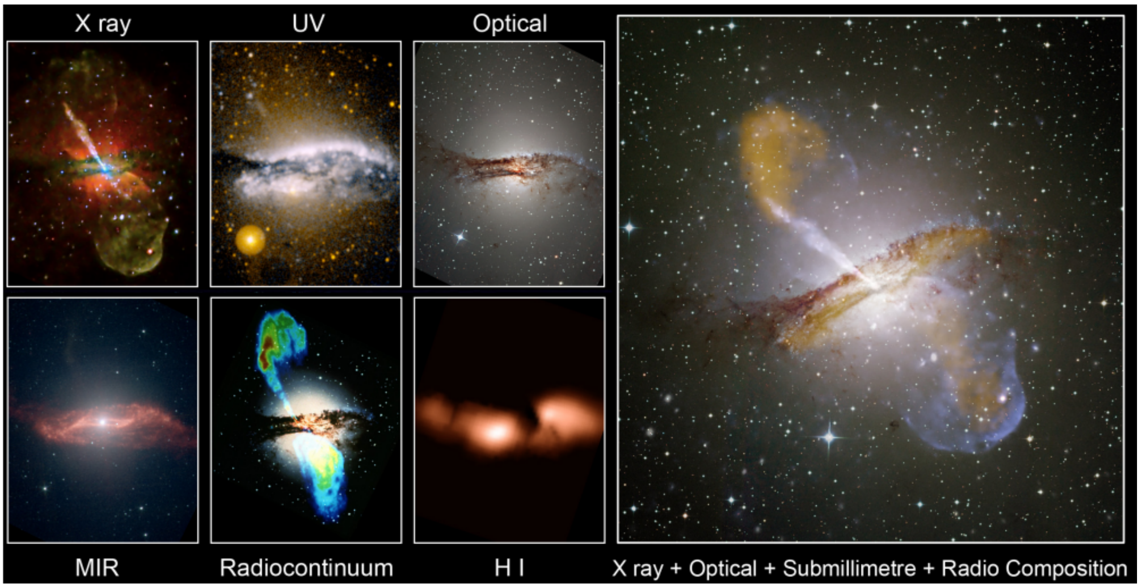

Figure 1.2: Images of the radio galaxy Cen A (NGC 5128), a jetted AGN, in different wavebands. (Azadi, 2017) This illustrates how the appearance of an AGN differs among different waveband regimes.

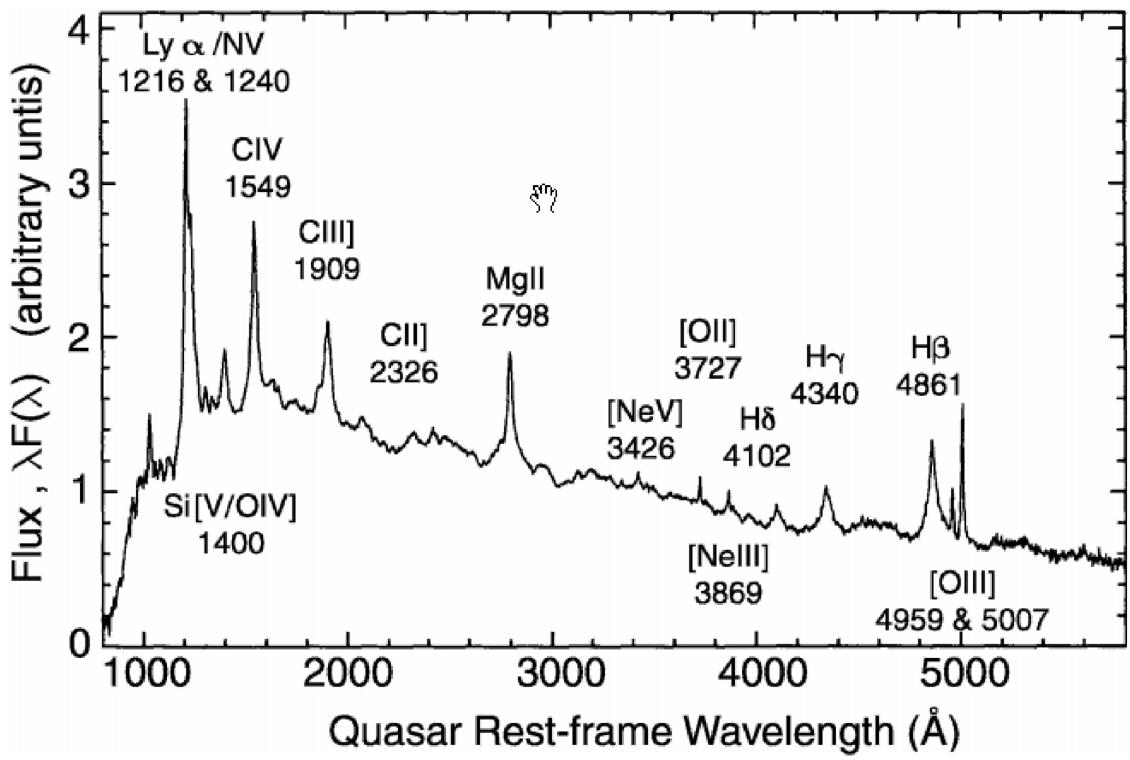

Figure 1.3: The mean spectrum of quasars showing the broad permitted (Lyα, CIV, MgII, Hδ, Hγ, and Hβ), semi-forbidden (CIII] and CII]), and narrow forbidden (Si[V/OIV], [NeV], [OII], [NeIII], and [OIII]) emission lines. Figure taken from Schneider (2006).

that a line is semi-forbidden (forbidden). Notably, among the broad emission lines, no forbidden lines are observed (Schneider, 2006). The broad emission lines can often reach a full width at half maximum (FWHM) of about 10^4 km$\cdot$s^{-1} (Padmanabhan, 2002; Schneider, 2006), whereas narrow lines can have a FWHM of a few 100 km/s (Schneider, 2006). These narrow emission lines are considerably wide compared to the characteristic velocities within inactive galaxies (Schneider, 2006).

Generally, it is accepted that the lines discussed above in AGN emerge from regions of high density, high orbital velocity (broad line region (BLR)) and low density, low orbital velocity (narrow line region (NLR)) that are orbiting with bulk motions around the SMBH (see Figure 1.4; Böttcher et al., 2012; Padmanabhan, 2002; Schneider, 2006). The BLR and NLR are discussed in the next section.

- **Variability:** The optical luminosities of inactive galaxies do not vary much compared to those of active galaxies that are highly variable, fluctuating with nearly a factor of 2 or more (Padmanabhan, 2002). The spectra and luminosities of AGNs are significantly variable on timescales of years down to minutes (Böttcher, 2019; Schneider, 2006; Urry and Padovani, 1995). The shortest variability time scales, down to minutes, were discovered in the observations of very high-energy (VHE) gamma-rays using the ground-based Imaging Atmospheric Cherenkov Telescope facilities (IACT; H.E.S.S., MAGIC, VERITAS) (Böttcher, 2019). Generally, the variability of an AGN is different in different wavelength bands across the entire EM spectrum. As we move from lower through higher frequencies of the observed emission, the variability timescale is smaller and its variability amplitude becomes larger (Böttcher, 2019; Padmanabhan, 2002; Netzer, 2015).

- **Polarization in Different Wavebands:** An AGN is observed to be radio, IR, and optically polarized. The radio and optical polarization measurements provide us with direct constraints on the geometry and the evolution of the jet magnetic field (Böttcher, 2019; Liodakis et al., 2022; Zhang, 2019). However, measurements of optical polarization are the best probes of the magnetic field geometry in the high energy emission regime (Böttcher, 2019; Zhang, 2019). In addition to radio and optical polarization, there are intense AGNs, e.g., blazars, that are observed to be polarized in the X-ray (Liodakis et al., 2022) and gamma-ray bands (Böttcher, 2019; Zhang and Boettcher, 2013; Zhang, 2019).

- **Radio Jets:** All radio galaxies (RGs) have jets or lobes along the poles of the accretion disk (Böttcher et al., 2012). These jets are very relativistic and extend over distances on scales up to Mpc, which is much larger than the size of the host galaxy itself. Often only one jet is observed (e.g., M87), and in most RGs where two jets are observed, one is much fainter than the other (Schneider, 2006). Furthermore, the appearance of the jet strongly depends on its viewing angle, which is the angle between our LoS and the axis of the jet itself (Netzer, 2015).

1.1.1 The Unified Model of AGN

From the smallest to larger scales, the major components of an AGN, according to Urry and Padovani (1995), are (see Figure 1.4):

Supermassive Black Hole: According to the standard unified model (Figure 1.4), there exists a central compact supermassive object with a strong gravitational field within the center of an AGN (Reynolds et al., 2014). This object is commonly known as an SMBH, or sometimes the massive accreting BH, with mass ranging from about 10^6 $M_\odot$ to about 10^9 $M_\odot$ (Böttcher et al., 2012). The SMBHs evolve due to the consumption of the adjacent matter that falls into the BH's gravitational field (Longair, 2010). It is concluded that the massive accreting BH is the fundamental component of the nuclear engine that powers AGNs (Schneider, 2006).

The SMBH has a boundary called the event horizon, which can be described as a spherical region where the escape speed of a particle ought to surpass the speed of light (Frank, 2016). The size of the event horizon is characterized by Schwarzschild radius $R_s = 2GM_{BH}/c^2$ (Frank, 2016), where G is the universal gravitational constant, M_{BH} is the mass of the BH, and c is the speed of light. Around the horizon is the accretion disk, where internal (heat) energy can be converted into radiation (Frank, 2016).

Accretion disk: The astrophysical object that is optically thick and geometrically thin formed around the BH as the nearby gas matter with a small amount of angular momentum is attracted by the BH's gravitational field and consequently spirals inward (Abramowicz and Straub, 2014; Frank, 2016; Hartle, 2003). As the gas matter spirals inward, it rotates faster than the gas further away from the BH (Bruss, 2012). These nearby and further gaseous matter interact with each other (Bruss, 2012). The matter in the accretion disk will then be heated to extreme temperatures by viscous forces (e.g., internal friction; Bruss, 2012; Schneider, 2006). In addition, the very same viscous forces cause a gradual loss of energy and angular momentum (Abramowicz and Straub, 2014; Frank, 2016; Longair, 2010; Urry and

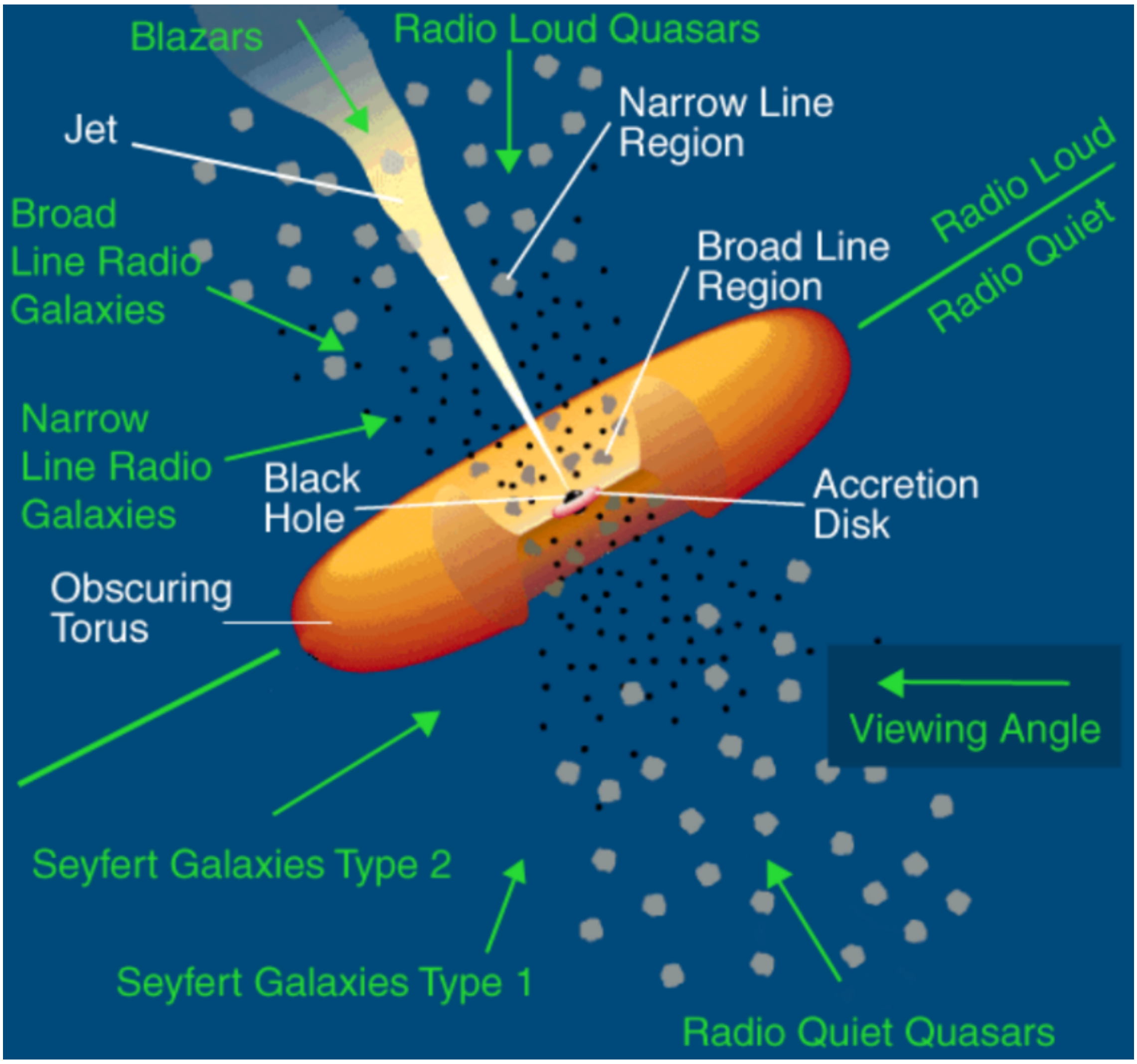

Figure 1.4: Illustration of the zoology of an AGN by the basic unified model. Figure from Urry & Padovani (1995) as cited by Reynolds et al. (2014).

Padovani, 1995), whereby gas matter will slowly spiral inward until they reach the innermost stable orbit where they fall straight into the BH (Hartle, 2003). As the disk matter spirals onto the BH, its gravitational potential energy is subsequently converted into kinetic energy, then into thermal blackbody radiation (Schneider, 2006). A portion of the thermal energy is transformed into EM radiation, which then escapes the disk and cools it down (Abramowicz and Straub, 2014; Hartle, 2003; Netzer, 2015). Accretion generates thermal optical-UV-X-ray emission that typically outshines the entire host galaxy (Abramowicz and Straub, 2014; Frank, 2016).

Additionally, strong magnetic fields can arise from the plasmas within the accretion disk or be frozen within the accreting BH (Blandford et al., 2019). The disk revolution is the cause of helical field lines, see Figure 1.5. These field lines play a significant role in the jet collimation (Schneider, 2006; Blandford et al., 2019).

Corona: It is generally believed that there might be a low-density plasma of highly energetic electrons surrounding or as a part of the disk. This plasma causes the disk optical/UV photons to undergo inverse Compton (IC) scattering to produce continuum X-ray radiation, and it is said to be an X-ray corona. (Böttcher et al., 2012; Urry and Padovani, 1995)

Broad line region: In the close vicinity of the corona is the BLR, the region consisting of partially ionized gas clouds of high electron densities of $n_e \gtrsim 10^9$ cm^{-3} (Padmanabhan, 2002; Schneider, 2006). These gas clouds orbit the core at high bulk velocities ranging from roughly $(1,000 - 10,000)$ km·s^{-1} (Padmanabhan, 2002; Schneider, 2006). Moreover, due to these high densities of the clouds, the forbidden emission lines are not observed in this region, as they are suppressed by collisions (Padmanabhan, 2002; Schneider, 2006). The temperature of the BLR can be as high as 20,000 K (Schneider, 2006).

Obscuring torus: Encircling the BLR is the obscuring torus, the optically thick dusty structure that obscures the SMBH from certain angles (Reynolds et al., 2014; Urry and Padovani, 1995). It is through the obscuration of the core that we can classify AGN as Type 1 AGNs when an AGN is observed at angles where the inner core is directly seen, and Type 2 AGNs when the very same AGN is observed at angles that the torus obscures the BLR and the emission from the disk (Reynolds et al., 2014; Urry and Padovani, 1995). Its radial extent ranges from approximately (0.1 - 10) pc.

Narrow line region: Outside the obscuring torus is the so-called NLR, the region composed of clouds of low electron densities of $n_e \leq (10^3 - 10^6)$ cm^{-3}, orbiting at low bulk velocities in the range of $(300 - 1000)$ km·s^{-1} (Padmanabhan, 2002). Unlike the BLR, the NLR does not suppress forbidden lines collisionally due to the lower densities of the clouds (Schneider, 2006). NLR clouds have a characteristic temperature of about 16,000 K, which is a bit lower than in the BLR (Schneider, 2006).

Relativistic jet: The formation of jets takes place in the vicinity of the massive accreting BH, where energetic particles are released along the poles of the disk and escape spirally along the helical orientation of the magnetic fields (see Figure 1.5; Schneider, 2006; Urry and Padovani, 1995). These jets emit synchrotron radiation and are observable, in addition to RGs, in AGNs that are closely aligned to our line of sight (LoS), such as blazars. (Böttcher et al., 2012). The plasma in the jets streams outward on both the smallest and the largest (up to a few hundreds of kpc) scales at relativistic velocities, beaming the radiation forwardly. (Urry and Padovani, 1995).

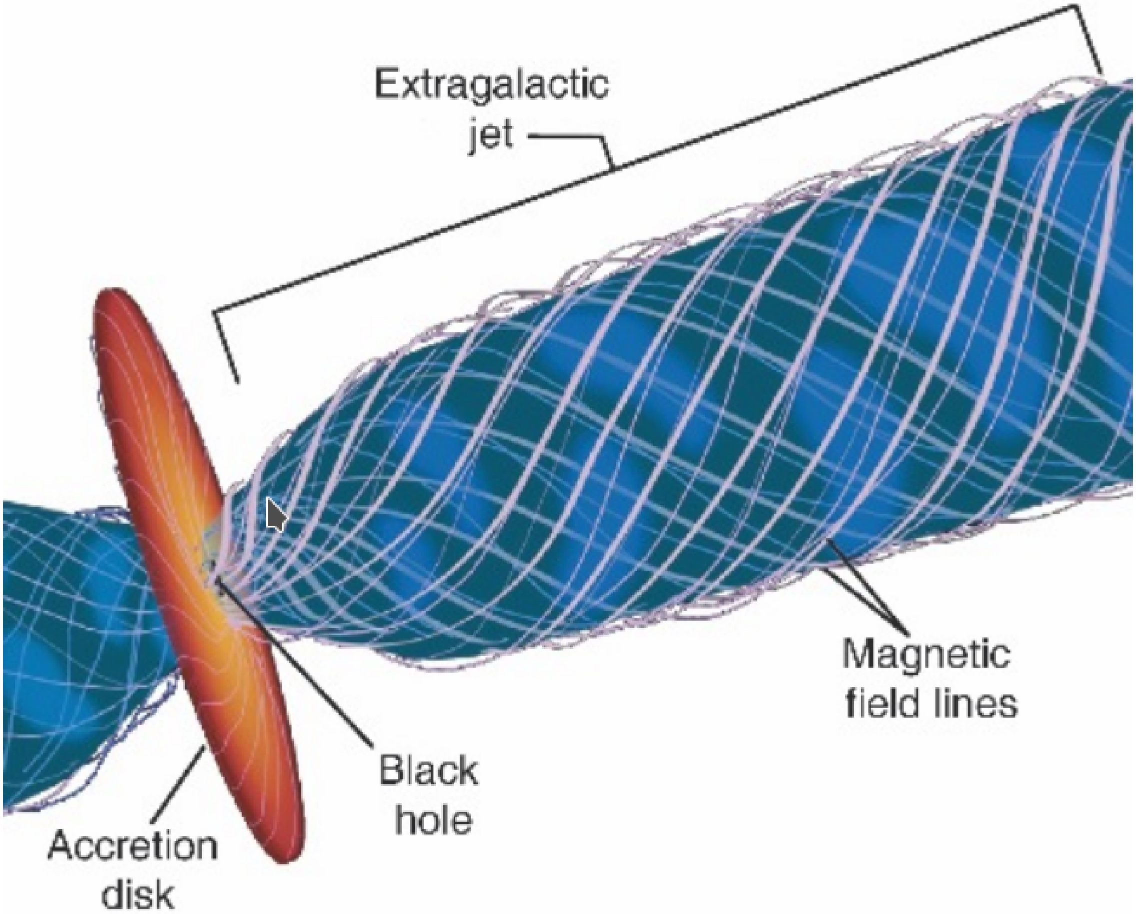

Figure 1.5: Demonstration of the jet model. The jet acceleration to relativistic velocities is due to a combination of strong gravitational fields within the vicinity of the SMBH and strong magnetic fields within the accretion disk that rotate rapidly. The field lines are helical. Moreover, shock fronts within the jet cause relativistic electrons to accelerate, which then strongly emit and appear as blobs within the jets. Figure from Schneider (2006).

Jets carry energy, linear and angular momenta over long distances ranging from the BH radius of $R_{BH} = (10^{-4} M_{BH})/(10^{9} M_{\odot})$ pc to Mpc or more, to radio hotspots, hotspot complexes, and radio lobes surrounding the jets (Böttcher et al., 2012; Schneider, 2006). Jets often have an internal structure such as knots, the high brightness areas that are interspersed with segments of low brightness (Schneider, 2006).

How jets form and accelerate and what collimates them over long distances, is not yet well understood.

1.1.2 The Classification of AGN

There are two major classes of AGN based on the power of their synchrotron-emitting radio jets, namely the radio-loud (RL, jetted) and the radio-quiet (RQ, non-jetted) AGNs. RL AGNs make up the minority (about 10%) of the AGN population while the majority are RQ AGNs (Netzer, 2015; Padovani, 2016, 2017). Most RL AGNs emit their energy non-thermally across the entire EM spectrum while the multiwavelength emission of RQ AGN is thermal-dominated emission, directly or indirectly related to the disk (Padovani, 2016, 2017). However, RL and RQ AGNs show similar spectra in the range of mid-IR to soft X-ray bands (see Figure 1.6; Schneider, 2006).

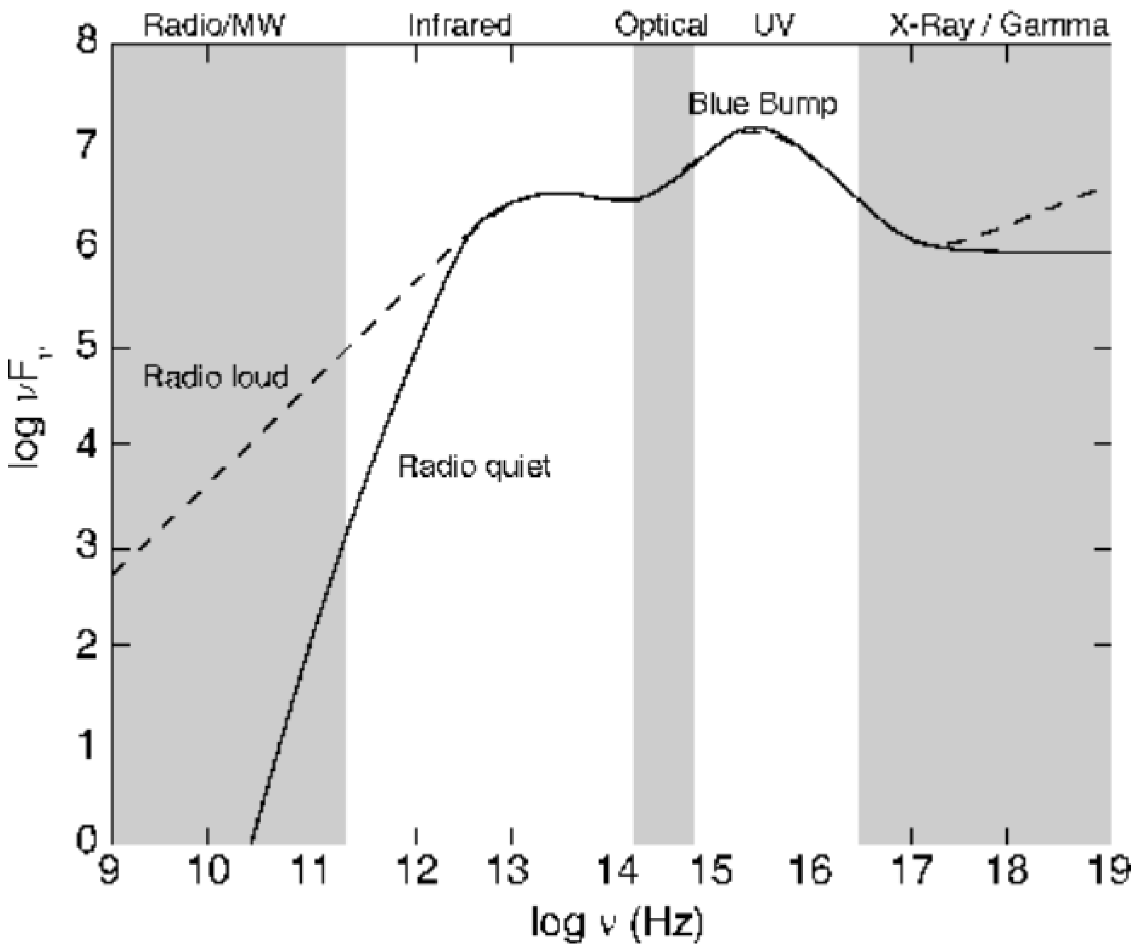

Figure 1.6: The typical spectral behavior of radio-loud (dashed line) and radio-quiet (solid line) AGNs. It shows a prominent maximum, the blue bump, and a secondary maximum from the UV through the soft X-ray and in the infrared bands, respectively. The spectrum depends very much on the type of AGN. (Schneider, 2006)

Moreover, Urry and Padovani (1995) divided AGNs according to both their radio loudness (RL and RQ AGNs) and their optical emission lines, i.e., whether they

		Optical emission line properties		
		Type 2 (narrow lines)	Type 1 (broad lines)	Type 0 (unusual)
Radio loudness	radio–quiet	Sy2 Type–2–QSO IR–Quasar?	Sy1 QSO	BAL QSO?
	radio–loud	NLRG < FR I, FR II	BLRG SSRQ FSRQ	Blazars < BL Lac, (FSRQ)

Black hole spin

Decreasing angle to line of sight

Table 1.1: The AGNs classification scheme based on the BH spin and the angle between the accretion disk and our line of sight (LoS). In this particular scheme, the radio emission strength is associated with the BH spin, which increases towards the bottom of the table. Moreover, the smaller the jet orientation, the stronger core dominance. Table from Urry and Padovani (1995) as cited by Schneider (2006).

show narrow emission lines (Type II), broad lines (Type I), or unusual or weak emission lines (Type 0; see Table 1.1).

1.1.3 Radio-quiet

The RQ sources are characterized by significantly low ratios of radio-optical flux density of $R = \log(S_{1.4}/S_{\rm V}) \lesssim 10$ and radio luminosities of $L_{1.4} \lesssim 10^{32}$ erg s^{-1} Hz^{-1} at a frequency of 1.4 GHz (Padovani et al., 2011; Padovani, 2016, 2017). Here, $S_{1.4}$ and $S_{\rm V}$ are both flux densities at a frequency of 1.4 GHz and in the V-band, respectively (Padovani et al., 2011). R values were chosen by Schmidt (1970) to indicate the radio-loudness of a galaxy.

In the Type I AGN class, these are the relatively low-luminosity Seyfert I galaxies, which are closely observed, and the more luminous RQ quasars (QSO), which are generally observed at large distances. RQ Type II AGNs are Seyfert II galaxies that are low luminous and are observed close by as well. The only distinction observed between Seyfert 1s and IIs is due to the different orientations of an AGN w.r.t. our LoS (Schneider, 2006).

1.1.4 Radio-loud

1.1.4.1 Radio Galaxies

Radio galaxies (RGs) are usually identified with luminous ellipticals and are often associated with radio-emitting jets and lobes that can extend up to distances of 10 pcs to 1 Mpc from the central region.

RL Type II AGNs are narrow line RGs (NLRGs) which are further subdivided based on their luminosity at frequency $\nu = 1.4$ GHz. If $L_{1.4} \lesssim 10^{32}$ erg·s^{-1}·Hz^{-1}, they are called low-luminosity Fanaroff-Riley Type I (FRI), which often have symmetric radio jets and whose surface brightness decreases away from the nucleus, and if $L_{1.4} \gtrsim 10^{32}$ erg· s^{-1}·Hz^{-1}, they are called high-luminosity FRII, whose jets are highly collimated and their surface brightness increases away from the nucleus (Netzer, 2015; Padmanabhan, 2002; Schneider, 2006).

RL Type I AGNs are called low-luminosity broad line RGs (BLRGs) and high-luminosity RL quasars, depending on the radio spectral index α_R, either flat spectrum radio quasars (FSRQs) with $\alpha_R \lesssim 0.5$ or steep spectrum radio quasars (SSRQs) with $\alpha_R \gtrsim 0.5$ (Padmanabhan, 2002; Padovani, 2016; Netzer, 2015; Urry and Padovani, 1995). The variation in the α_R measurement is due to the viewing angle of the radio jet w.r.t. our line of sight (Netzer, 2015).

1.1.4.2 Blazars

Blazars are RL, jetted AGNs whose jets point at small orientations (about $< 15^o - 20^o$, Padovani, 2016, 2017) w.r.t. our line of sight, with a set of characteristic properties including a highly variable radio emission, strongly-variable high-energy gamma-ray emission (Ghisellini, 2013; Netzer, 2015; Schneider, 2006), a double-peak SED with a low-energy peak at radio-X-ray energies and a high-energy peak at X-ray through gamma-ray energies (see Figures 1.7 and 1.8), and high polarization at both optical and radio frequencies in most objects (Böttcher et al., 2012).

Blazars are subdivided into FSRQs and BL Lacertae (BL Lac) objects. The FSRQs, the quasar-type blazars, which are sometimes called optically violent variables, have strong emission lines with an equivalent width of their lines being EW > 5 Å(Ghisellini, 2013; Urry and Padovani, 1995). However, they are noted as Type 0 sources in Table 1.1 because as BL Lacs they have the same blazar-like continuum emission. BL Lacs lack strong, broad optical emission lines with EW < 5 Å.

The multiwavelength SEDs of blazars are generally dominated by two broad, non-thermal components, i.e., the low-energy component from radio to UV or in some

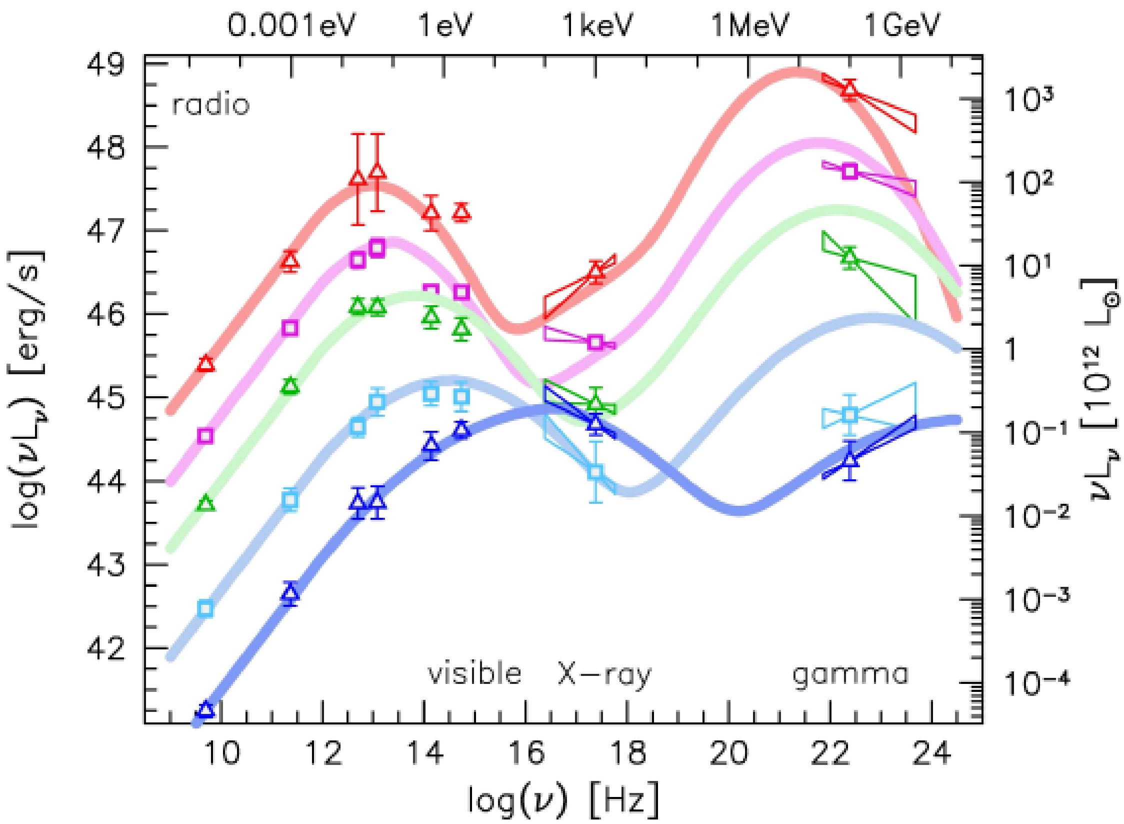

Figure 1.7: The multi-frequency spectra of blazars; flat spectrum radio quasars (FSRQs, red), low-synchrotron-peaked BL Lacs (LBL, pink), intermediate-synchrotron-peaked BL Lacs (IBL, green), high-synchrotron-peaked BL Lacs (HBL, light blue), and low-powered extreme HBL (dark blue). From Fossati et al. (1998) cited by Blandford et al. (2019).

cases, X-rays, and the high-energy component from X-rays through gamma-rays (Blandford et al., 2019; Böttcher et al., 2013b). Figure 1.7 shows mean SEDs of blazar classes. This is said to be the blazar sequence by Fossati et al. (1998), who identified this first. The shift of the SED peaks towards lower frequencies goes in tandem with a higher gamma-ray dominance (Compton dominance). The location of the synchrotron-peak frequencies varies from one source to another. Low-synchrotron-peaked (LSP) blazars defined by the synchrotron-peak frquency $\nu < 10^{14}$ Hz, are FSRQs and low-frequency-peaked BL Lacs, intermediate-synchrotron-peaked BL Lacs (IBLs) have frequencies 10^{14} Hz $\leq \nu < 10^{15}$ Hz, and high-synchrotron-peaked BL Lacs (HBLs) have frequencies $\nu > 10^{15}$ Hz (Böttcher et al., 2013b; Böttcher, 2019; Zhang and Boettcher, 2013).

Variability of Polarization: It is well known that the radio-optical emission of blazars is polarized with crucial variability in both the polarization degree (PD) and angle of polarization (Böttcher, 2019; Zhang et al., 2015; Zhang, 2019). Optical polarization in blazars varies from nearly unpolarized to highly polarized sources/s-

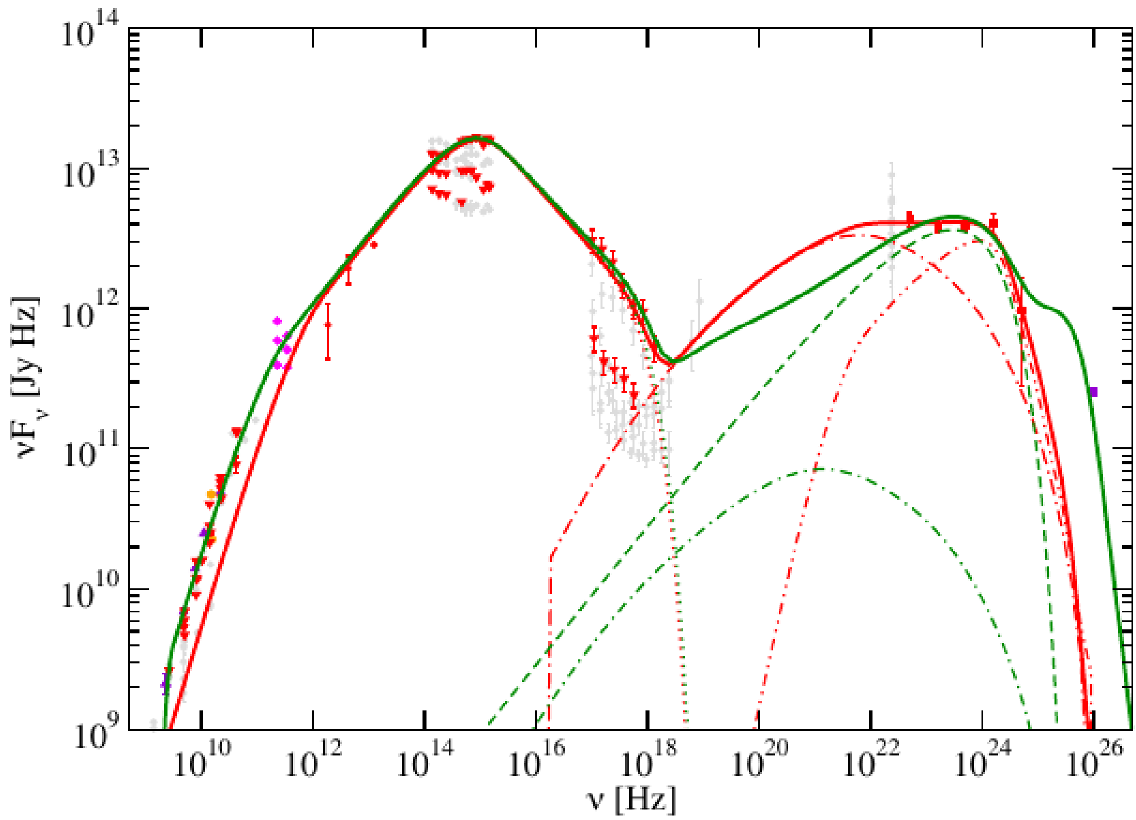

Figure 1.8: The fits of leptonic (red) and hadronic (green) models to the spectral energy distribution (SED) of BL Lac S5 0716+714. (Böttcher et al., 2013b)

tates with degrees of polarization of less than or roughly 50 percent (Böttcher, 2019; Zhang, 2019). This dissertation will focus on the degree of polarization across the entire SED of blazars.

It has been found that the average PD for gamma-ray loud blazars is systematically larger than for gamma-ray quiet blazars due to the fact that gamma-ray loud blazars are observed to be more strongly Doppler boosted and therefore more strongly synchrotron-dominated in the optical band (Angelakis et al., 2016; Böttcher, 2019). The mean optical PD is systematically inversely proportional to the peak of synchrotron frequency (Angelakis et al., 2016; Böttcher, 2019; Zhang, 2019). This can be attributed to the fact that in LSP blazars the optical range is at or near the synchrotron radiation peak, causing freshly accelerated electrons to be contained in a presumably very confined region in the jet, whereas in HSP blazars, electrons emitting the optical synchrotron radiation have already cooled substantially and are presumably distributed over a larger fraction of the jet (Böttcher, 2019).

While the polarization angles (PAs) typically show small, arbitrary angular variations during blazar flares, they are observed to have large rotations of about or more than 180° (Konigl and Choudhuri, 1985; Marscher et al., 2008; Quirrenbach et al., 1989), usually over the course of a few days (Böttcher, 2019; Marscher et al., 2008, 2010). Statistical studies of the RoboPol project demonstrated that the PA rotations are correlated with gamma-ray flares detected by Fermi-LAT and that the correlation is stochastic in a turbulent jet environment (Blinov et al., 2016a,b, 2018). The PA swings can occur in either direction in any given source and therefore there is no preferred direction for PA swings. Furthermore, PA rotations might be produced by a change in the jet geometry with a helical magnetic field (Böttcher, 2019; Marscher et al., 2010).

1.2 Framework

Finally, based on the subject of this thesis, we present a few selected previous related works and the problem statement along with the research aims.

1.2.1 Previous Related Work

Jamil and Boettcher (2012) constructed a multi-zone model with ordered magnetic fields, fit to the multi-wavelength data of Markarian 421, and found that the orientations of the magnetic field play a significant role in the normalization of the synchrotron spectrum. In contrast, the Compton emission is almost unaffected by the magnetic field orientations. This is because the photon distribution anisotropies induced by the magnetic field orientation are lost when scattering off an isotropic distribution of relativistic electrons.

Böttcher et al. (2013b) used single-zone leptonic and hadronic models to fit the SEDs of 12 blazars detected by Fermi-LAT. They found out that the SEDs of blazars can be well represented in the leptonic model with parameters close to the equipartition between the magnetic field and the relativistic electrons in the emission region. Here, magnetic field orientation and polarization effects have been ignored.

Joshi et al. (2016) used the multi-zone radiation feedback model of Joshi et al. (2014) to study the effects of the magnetic field orientation on the SEDs of a typical blazar. They demonstrated that a low-energy SED component that follows a reciprocal relationship with the boosting of the viewing angle may be produced by a magnetic field that is parallel to the jet axis. Effects of viewing angle and polarization have been ignored.

The fitting of a one-zone synchrotron and synchrotron self-Compton (SSC) model to the SEDs of blazars by taking into account the anisotropy of the radiation produced and the polarization under the influence of the synchrotron radiation and SSC scattering has never been performed. This is the main purpose of the modeling developments in this thesis.

1.2.2 Problem Statement

For SEDs of blazars, a non-thermal distribution of relativistic electrons emits synchrotron radiation in the low-frequency component and produces high-energy emission through Compton scattering. It is typically known that in a perfectly uniform magnetic field, linear polarization arises from synchrotron emission of relativistic charged particles and IC scattering of relativistic electrons will only decrease the degree of polarization of the target photon field by a factor of about 1/2 (Bonometto and Saggion, 1973).

Most previous work on models ignores any angle dependence of the emission in the rest frame of the emission region and assumes everything to be isotropic. In this work, we will explore the angle dependence of synchrotron and SSC spectra in a perfectly uniform magnetic field, taking into account the polarization-dependence of IC scattering of synchrotron radiation. We will compare our results to the selected previous anisotropic-emission models.

1.2.3 Research Aims

In this dissertation, we will focus on the development of a single-zone synchrotron/SSC blazar multiwavelength emission model with relativistic electrons in a perfectly uniform magnetic field. We aim at exploring the parameter space, such as magnetic-field orientation w.r.t. the jet axis, magnetic-field strength, electron distribution parameters, etc., and compare the results with those obtained in past papers.

In **Chapter 2** we discuss non-thermal emission processes that give rise to the multiwavelength SED and polarization of blazars. **Chapter 3** describes our single-zone synchrotron/SSC blazar emission model. The results with discussion are given in **Chapter 4**. The dissertation's summary and conclusions are presented in **Chapter 5**. Finally, future work is discussed in **Chapter 6**.

Chapter 2

Non-thermal mechanisms and polarization in blazars

A brief background on non-thermal mechanisms that give rise to the multi-wavelength SED and polarization of blazars is presented here. We begin by introducing the non-thermal distribution of particles that will be considered throughout the study. In the subsequent sections, we will examine formulae for emission coefficients relevant to the synchrotron radiation and Compton scattering mechanisms, and the features of the radiation spectra produced by distributions of non-thermal, relativistic particles. We end the background of the 'non-thermal mechanisms' with a discussion of high-energy blazar emission models, namely leptonic and hadronic models.

Finally, the concept of polarization is explained briefly, followed by a specific discussion of the polarization of synchrotron radiation together with a brief explanation of X-ray and gamma-ray polarization.

2.1 Non-thermal Emission Mechanisms

If emission has a spectrum that cannot be represented as the black-body radiation spectrum, then it is said to be a non-thermal emission, such as the power-law synchrotron spectra or relativistic Compton scattering. In this section, we will demonstrate the general shapes of the radiation spectra that correspond to specific radiation mechanisms by taking into account the relativistic electrons with a basic power-law energy distribution of

$$n_e(\gamma)d\gamma = n_0\gamma^{-p}d\gamma \quad \text{for} \quad \gamma_{\min} \leq \gamma \leq \gamma_{\max}. \tag{2.1}$$

Here, $n_e(\gamma)$ is the electron number density in the interval $[\gamma, \gamma + d\gamma]$ of Lorentz-factor (electron energies) γ, n_0 is the power-law electron distribution normalization factor in units cm^{-3}, p is the spectral index, and $\gamma_{\rm min}$ and $\gamma_{\rm max}$ are low-energy and high-energy cutoffs. The p values commonly run from $2-3$, but in some cases, they can be either smaller or larger. While the photon energy index for both synchrotron and Compton spectra can be related to p as

$$\alpha = \frac{p-1}{2}, \tag{2.2}$$

the emitted radiation spectrum of each mechanism at a specific frequency ν may be related to α as

$$j_\nu \propto \nu^{-\alpha}. \tag{2.3}$$

This tells us that the emitted synchrotron and Compton spectra by power-law distributions of non-thermal particles follow a power-law spectrum. A detailed discussion of non-thermal emission processes can be found in Dermer and Menon (2009), Longair (2010), and Rybicki and Lightman (1991).

2.1.1 Synchrotron Radiation

Synchrotron radiation is non-thermal EM radiation produced when energetic charged particles, such as relativistic electrons, move along a spiral path in a uniform magnetic field (as shown in Figure 2.1). This spiraling motion is due to the Lorentz force, which causes a constant change in the direction of the velocity vector of the particle without altering its absolute value. The acceleration vector associated with this force is always perpendicular to the particle's velocity vector. As these charged particles experience acceleration, they emit EM radiation and consequently lose energy. The radiation is beamed along the direction of the electrons (Longair, 2010; Netzer, 2015). This type of EM radiation has several distinctive features, including high degrees of linear polarization (see subsection 2.3.1) which refers to the uniform orientation of the electric field in a specific direction.

In this subsection, we discuss the synchrotron radiation spectra produced by both a single relativistic electron and an ensemble of relativistic electrons.

2.1.1.1 Synchrotron Radiative Power

Imagine a relativistic electron with energy $E = \gamma m_e c^2$ moving in a helical trajectory with pitch angle φ in a perfectly ordered magnetic field with strength B. The angle φ is the angle that the magnetic field vector makes with the velocity of the electron (or commonly, with the LoS). The mean synchrotron spectral energy emitted by each electron per cycle at frequency ν averaged over polarizations, is described as (Böttcher et al., 2012; Dermer and Menon, 2009; Ghisellini, 2013; Rybicki and

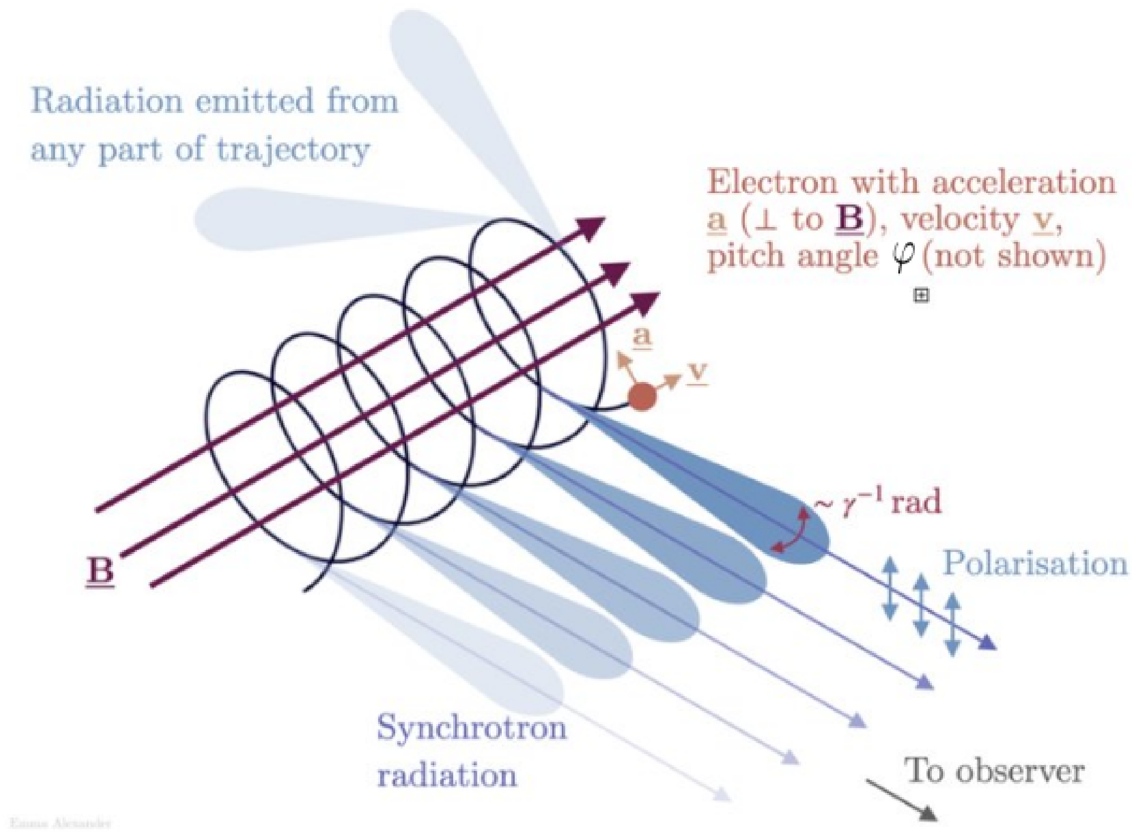

Figure 2.1: Synchrotron radiation arising from an electron moving along a helical path around an ordered magnetic field. The Lorentz force causing the acceleration $\vec{a}$ is perpendicular to the magnetic field vector $\vec{B}$, and both are also perpendicular to the circular component of the electron's velocity $\vec{v}$. The radiation is concentrated in the emission cones of angle $1/\gamma$ radians. From Alexander (2022).

Lightman, 1991):

$$P_\nu^{\rm syn}(\gamma,\varphi) = \frac{\sqrt{3}e^3}{m_e c^2} B \sin(\varphi) F(x) \tag{2.4}$$

in units of ergs$\cdot$s$^{-1}\cdot$Hz^{-1}, where

$$x = x_\varphi(\gamma) = \frac{\nu}{\nu_\varphi(\gamma)} \tag{2.5}$$

with the electron critical frequency

$$\nu_\varphi(\gamma) = \frac{3e}{4\pi m_e c} B\gamma^2 \sin(\varphi) \approx 4.2 \times 10^6 \gamma^2 \frac{B}{[\rm Gauss]} \sin(\varphi)\ [\rm Hz] \tag{2.6}$$

and the spectral function

$$F(x) = F(x_\varphi(\gamma)) = x_\varphi(\gamma) \int_{x_\varphi(\gamma)}^{\infty} K_{5/3}(\xi) d\xi. \tag{2.7}$$

Here, e refers to the charge of an electron, m_e represents the mass of an electron, c is the speed of light, and $K_{5/3}$ denotes the modified Bessel function of the second kind with an order of 5/3. Figure 2.2 shows the spectrum of a single electron denoted by $F(x)$, which reaches its maximum at approximately $x = 0.29$ as shown in the upper panel. The low-frequency portion (when $x \ll 1$) of this spectrum can be reasonably approximated by a power law with a slope of 1/3, whereas toward higher frequencies (when $x \gg 1$), the spectrum falls exponentially (see lower panel of Figure 2.2; Rybicki and Lightman, 1991):

$$F(x) \to \frac{4\pi}{\sqrt{3}\Gamma(\frac{1}{3})}\left(\frac{x}{2}\right)^{1/3} \quad \text{for} \quad x \ll 1, \tag{2.8a}$$

$$F(x) \to \left(\frac{\pi x}{2}\right)^{1/2} e^{-x} \quad \text{for} \quad x \gg 1. \tag{2.8b}$$

2.1.1.2 Synchrotron Emissivity

For a power-law distribution of electron energies γ (Equation 2.1), the coefficient of synchrotron radiation per unit volume per unit frequency can be calculated by integrating the product of electron energy distribution function $n_e(\gamma)d\gamma$ and the single-particle synchrotron power $P_\nu^{\text{syn}}(\gamma, \varphi)$ over all possible values of γ in units of ergs·cm^{-3}·s^{-1}·Hz^{-1} (Rybicki and Lightman, 1991):

$$j_\nu^{\text{syn}}(\varphi) = \int d\gamma n_e(\gamma) P_\nu^{\text{syn}}(\gamma, \varphi). \tag{2.9}$$

By substitution of Equations (2.1), (2.4), and (2.7), this expression can be written as

$$j_\nu^{\text{syn}}(\varphi) = \frac{\sqrt{3}e^3 n_0}{m_e c^2} B\sin(\varphi) \int_{\gamma_{\text{min}}}^{\gamma_{\text{max}}} \gamma^{-p} F(x) d\gamma \tag{2.10a}$$

or

$$j_\nu^{\text{syn}}(\varphi) = \frac{\sqrt{3}e^3 n_0}{m_e c^2} B\sin(\varphi) \int_{\gamma_{\text{min}}}^{\gamma_{\text{max}}} \gamma^{-p} x_\varphi(\gamma) \int_{x_\varphi(\gamma)}^{\infty} K_{5/3}(\xi) d\xi d\gamma. \tag{2.10b}$$

For simplicity, following Longair (2010) and Rybicki and Lightman (1991), change the variables of integration to $x = \nu/\nu_\varphi(\gamma)$, keeping in mind $\nu_\varphi(\gamma) \propto \gamma^2$;

$$j_\nu^{\text{syn}}(\varphi) \propto \nu^{-\frac{p-1}{2}} \int_{x_{\text{min}}}^{x_{\text{max}}} x^{\frac{p-3}{2}} F(x) dx. \tag{2.11}$$

The integration limits x_{min} and x_{max} correlate with the boundaries γ_{min} and γ_{max}, repectively. Nevertheless, if the energy range is large enough, we can estimate x_{min} to be 0 and x_{max} to be infinity. This allows us to roughly assume that the integral remains constant, e.g.,

$$\int_0^\infty x^{\frac{p-3}{2}} F(x) dx \sim \text{constant}. \tag{2.12}$$

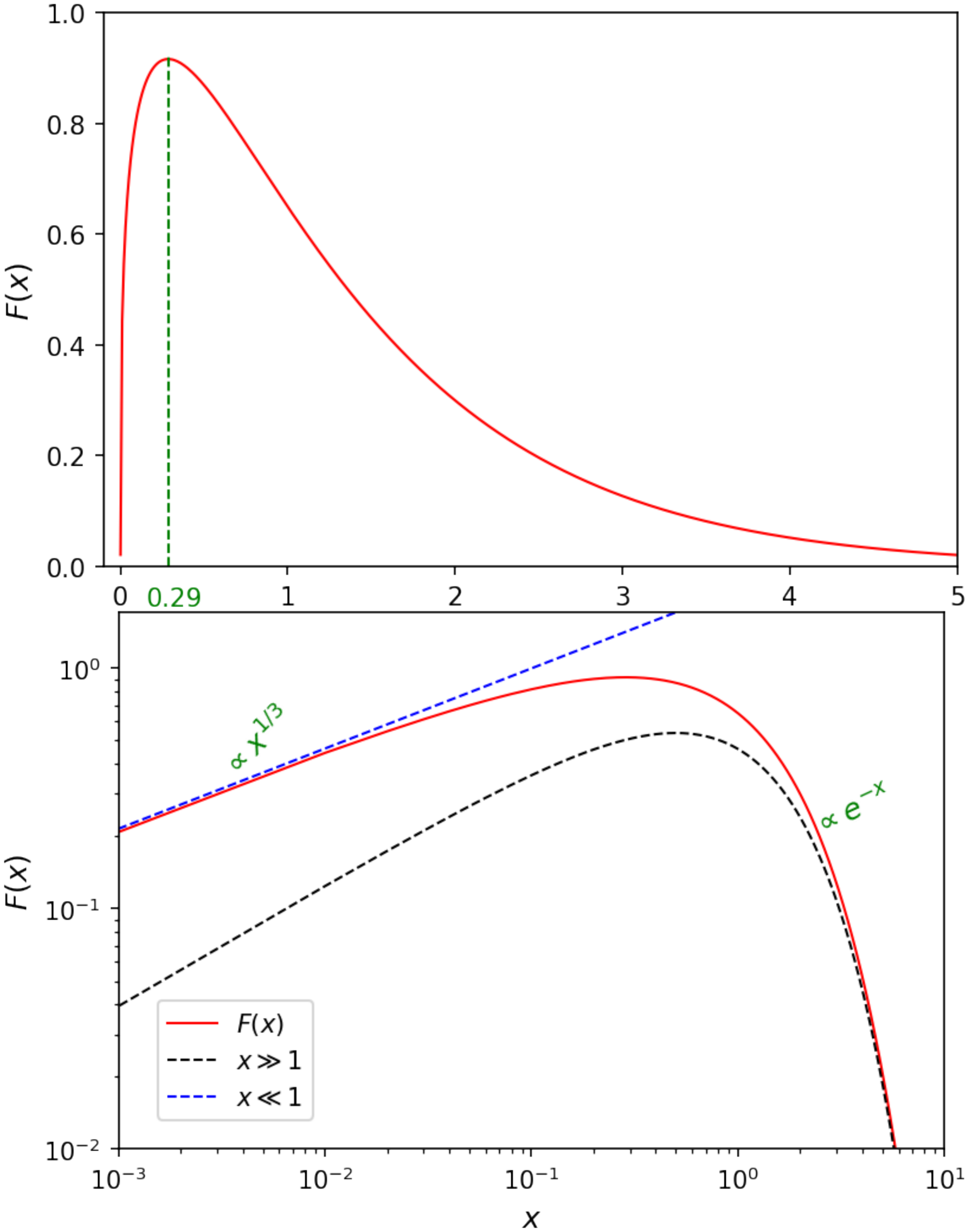

Figure 2.2: The single-electron synchrotron spectrum $F(x)$ displaying its peak at around $x-$value of 0.29 (top panel) and compared with its low-energy ($x \ll 1$) and high-energy ($x \gg 1$) approximations (lower panel).

Thus, the power-law distribution $n_e(\gamma) \propto \gamma^{-p}$ (Equation 2.1) of electron energies emits a synchrotron radiation spectrum following a power-law function (Longair, 2010; Rybicki and Lightman, 1991):

$$j_\nu^{\rm syn}(\varphi) \propto \nu^{-\frac{p-1}{2}} = \nu^{-\alpha}, \tag{2.13}$$

which is the result of a collection of the synchrotron power spectra of individual electrons, as illustrated in Figure 2.3.

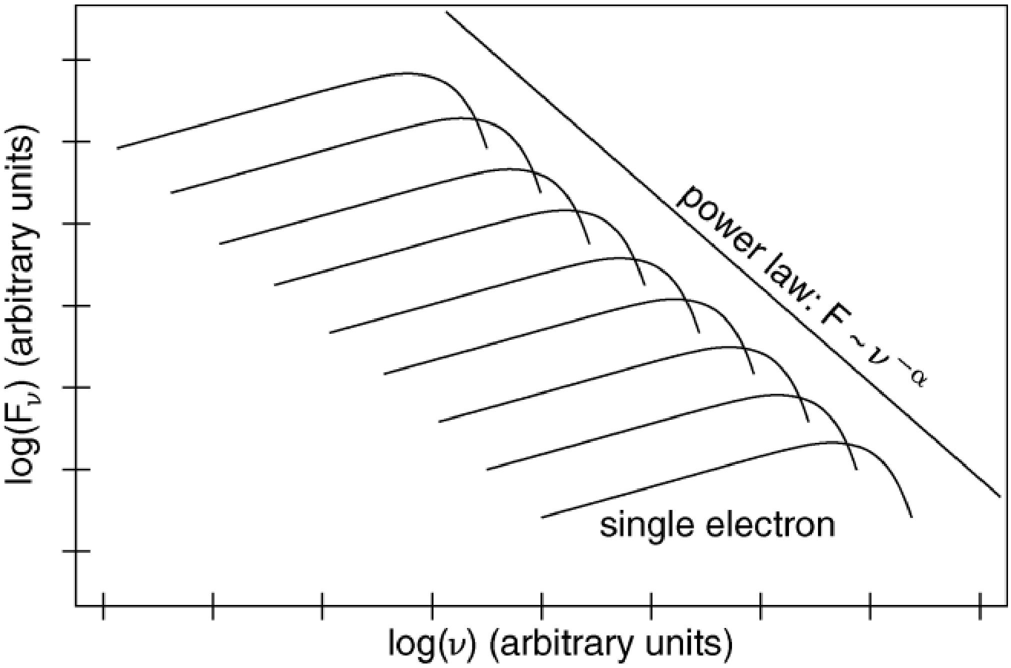

Figure 2.3: The characteristic synchrotron radiation spectrum traces a power-law function and is produced by summing the single-electron synchrotron spectra. From Schneider (2006).

Now, in order to simply describe $j_\nu^{\rm syn}(\varphi)$, we need to calculate the integral (2.12). Hence, with the use of the relation

$$\int_0^\infty x^\delta F(x)dx = \frac{2^{\delta+1}}{\delta+1}\Gamma\left(\frac{\delta}{2}+\frac{7}{3}\right)\Gamma\left(\frac{\delta}{2}+\frac{2}{3}\right) \tag{2.14}$$

with $\delta = (p-3)/2$, the coefficient of synchrotron radiation can be described as (Jamil and Boettcher, 2012; Longair, 2010; Rybicki and Lightman, 1991):

$$j_\nu^{\rm syn}(\varphi) = \frac{\sqrt{3}e^3 n_0 B\sin(\varphi)}{2m_e c^2(p+1)}\left(\frac{4\pi\nu m_e c}{3eB\sin(\varphi)}\right)^{-\frac{p-1}{2}}\Gamma\left(\frac{p}{4}+\frac{19}{12}\right)\Gamma\left(\frac{p}{4}+\frac{1}{12}\right), \tag{2.15}$$

where $\Gamma(a)$ represents the gamma function of argument a. For calculations of synchrotron emissivity in our study, we only use Equation 2.10 for any specific electron energy γ at a critical frequency $\nu_\varphi(\gamma)$ as given by Equation 2.6. Additionally, the low-energy and high-energy cutoffs of the synchrotron spectrum, which correspond to the points where the gradients change, could be related to the minimum (low) cutoff frequency $\nu_{\rm cut\ min}$ and the maximum (high) cutoff frequency $\nu_{\rm cut\ max}$ as

$$\nu_{\rm cut\ min,max} \approx 4.2\times 10^6 B\gamma^2_{\rm min,max}\sin(\varphi)\ [{\rm Hz}]. \tag{2.16}$$

2.1.2 Compton Scattering

The inelastic scattering mechanism between a photon and a free-charged particle (typically an electron) at rest as shown by Figure 2.4, is generally known as Compton scattering. The incoming photon with energy ϵ^{e^-} transfers part of its energy to the stationary electron, resulting in a low-energy photon and a high-energy electron. The scattered photon with energy $\epsilon_s^{e^-}$ has an arbitrary direction of motion specified by the scattering angle χ^{e^-} w.r.t. the incoming photon direction. The scattering angle is related to the incoming and the scattered photon energies as (Dermer and Menon, 2009; Rybicki and Lightman, 1991):

$$\cos\chi^{e^-} = 1 + \frac{1}{\epsilon^{e^-}} - \frac{1}{\epsilon_s^{e^-}} \tag{2.17}$$

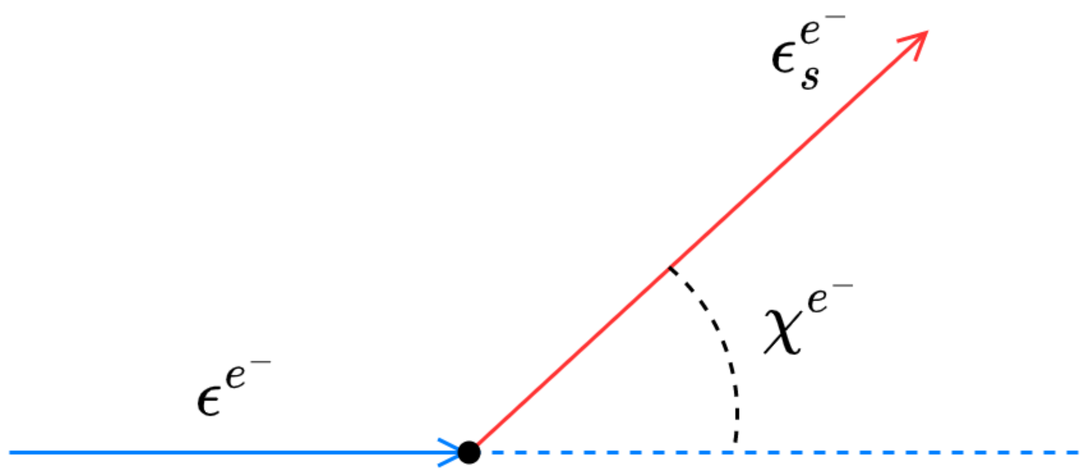

Figure 2.4: The Compton scattering mechanism geometry of the high-energy photon in the electron rest-frame. See Böttcher et al. (2012).

For an electron at rest, the incoming photon energy in the electron rest frame (ERF) and the Lab frame are equal, e.g., $\epsilon^{e^-} = \epsilon$. Here and after, we define $\epsilon = h\nu/m_ec^2$ to be the normalized photon energy in the electron rest mass-energy m_ec^2 units. The Compton scattering mechanism for relativistic electrons is treated in the following subsection.

2.1.3 Inverse Compton Scattering

The top panel of Figure 2.5 illustrates a mechanism called inverse Compton scattering, where a relativistic charged particle, such as an electron, up-scatters a low-energy photon to high-energy photons, i.e., X-rays and gamma-rays. In comparison to Compton scattering, here, is a relativistic electron that transfers part of its energy to low-energy photons. For small values of the target photon energy in the ERF, e.g., when $\epsilon^{e^-} \ll 1$, the scattered photon will have an energy of $\epsilon_s \approx \gamma^2 \epsilon$ in the rest frame of the emission region (Lab frame; Böttcher et al., 2012). This is referred to as a non-relativistic regime and is generally known as the Thomson regime. In contrast, when $\epsilon^{e^-} \gg 1$, the IC scattering is said to take place in the relativistic regime, usually referred to as the Klein-Nishina (KN) regime. In this regime, the scattered photon will have an energy of $\epsilon_s = \gamma m_e c^2$. Thus, in the Thomson regime, IC scattering is an efficient mechanism to generate high-energy photons. In this study, we consider only the scattering of the synchrotron photon fields in the Thomson regime.

Here and in the following, we denote quantities measured after the scattering by the subscript "s", quantities measured in the ERF by the superscript "e^-", and quantities measured in the Lab frame are characterized by non-superscript symbols.

2.1.3.1 Compton Scattering Cross-section

The Klein-Nishina (KN) cross-section, which is commonly known as the Compton scattering cross-section, is used to calculate the scattering between an electron with energy γ and a photon with energy ϵ. In the evaluation of the Compton scattering cross-section, the ERF (electron rest frame) is the most practical reference frame to use. Therefore, in the ERF, we can express the differential KN cross-section as (Böttcher et al., 2012; Dermer and Menon, 2009):

$$\begin{aligned} \frac{d\sigma_C}{d\Omega_s^{e^-} d\epsilon_s^{e^-}} = \frac{r_e^2}{2} \left(\frac{\epsilon_s^{e^-}}{\epsilon^{e^-}} \right)^2 \left(\frac{\epsilon_s^{e^-}}{\epsilon^{e^-}} + \frac{\epsilon^{e^-}}{\epsilon_s^{e^-}} - \sin^2 \chi^{e^-} \right) \\ \delta \left(\epsilon_s^{e^-} - \frac{\epsilon^{e^-}}{1 + \epsilon^{e^-}(1 - \cos \chi^{e^-})} \right). \end{aligned} \tag{2.18}$$

Here, σ_C denotes the total Compton scattering cross-section, $d\Omega_s^{e^-} = d\cos\chi^{e^-} d\phi_s^{e^-}$ represents the scattered photon solid angle element, $r_e = e^2/m_e c^2$ is the classical electron radius, ϵ^{e^-} and $\epsilon_s^{e^-}$ are energies of a photon before and after the scattering, and χ^{e^-} is the scattered photon angle w.r.t. the direction of the incoming photon. The δ function results from the conservation of energy and momentum. According to Böttcher et al. (2012) and Dermer and Menon (2009) the target (incoming) photon

energy in the ERF ϵ^{e^-} and the lab frame ϵ can be related as

$$\epsilon^{e^-} = \gamma \epsilon (1 - \beta \mu), \tag{2.19}$$

whereas the scattered photon energy in the ERF is related to the lab-frame scattered photon energy ϵ_s through

$$\epsilon_s^{e^-} = \gamma \epsilon_s (1 - \beta \mu_s^{e^-}). \tag{2.20}$$

Figure 2.5 demonstrates the angles and their cosines of the Compton scattering mechanism in the lab frame and the ERF. In Equation 2.19, $\mu = \cos(\theta)$ is the cosine

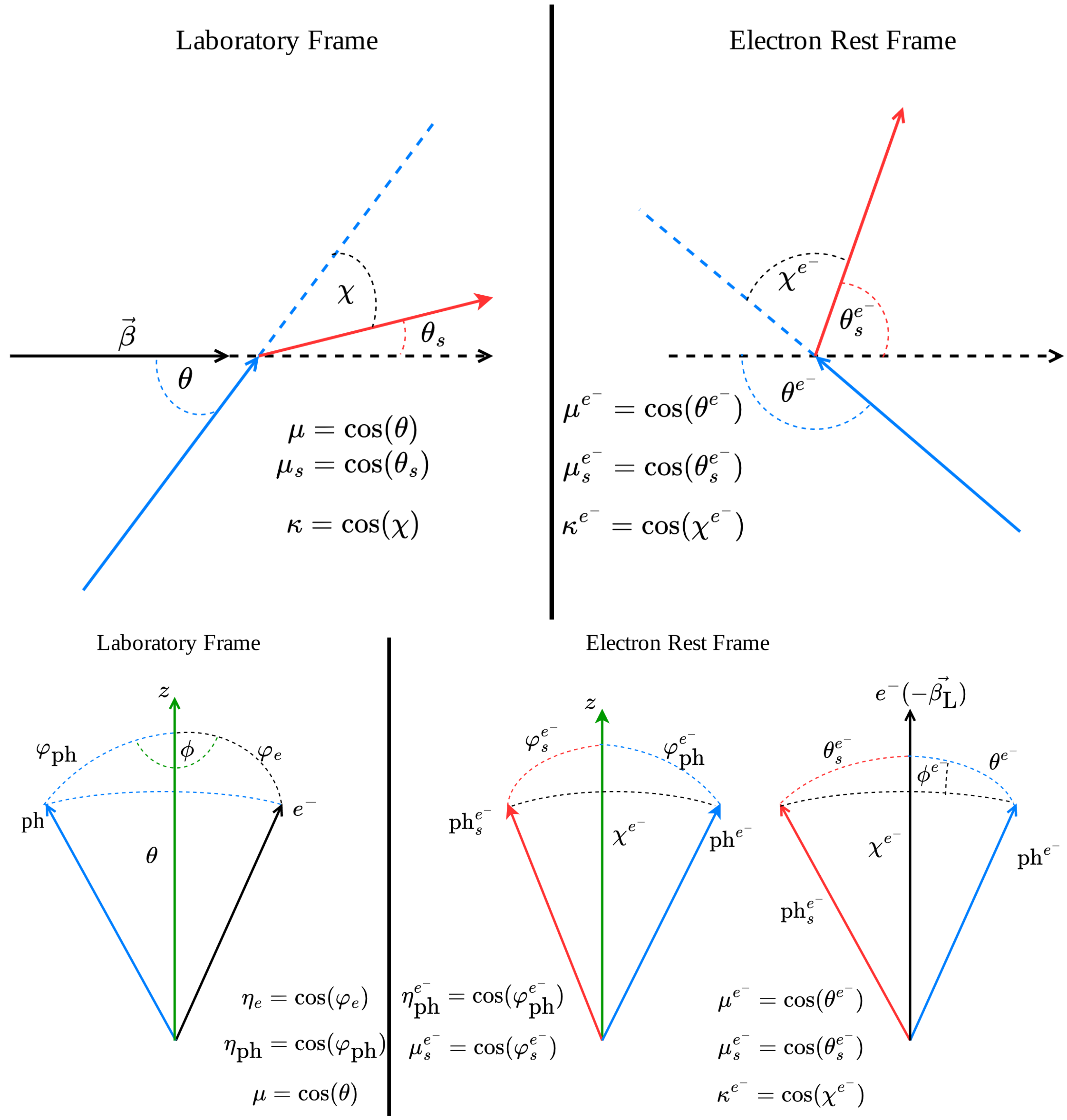

Figure 2.5: Angles of the Compton scattering geometry in the lab frame and the ERF (upper panel), and their transformations between the lab frame and the ERF (lower panel). See Böttcher et al. (2012).

of the angle between an electron and the incoming photon directions (see Figure 2.5) which is given as by Böttcher et al. (2012) and Dermer and Menon (2009) as

$$\mu = \eta_e \eta_{\rm ph} + \sin(\varphi_e)\sin(\varphi_{\rm ph})\cos(\phi_{\rm ph}), \tag{2.21}$$

where φ_e and $\varphi_{\rm ph}$ are angles of an electron and the target photon w.r.t. the $z-$axis in the lab frame, as shown in Figure 2.5. For the transformation of angles between the two frames, we use the photon relativistic aberration expressions given by as (Böttcher et al., 2012; Dermer and Menon, 2009):

$$\mu^{e^-} = \frac{\mu - \beta}{1 - \beta\mu}, \tag{2.22a}$$

and

$$\mu_s^{e^-} = \frac{\mu_s - \beta}{1 - \beta\mu_s}. \tag{2.22b}$$

The Compton scattering regimes are determined by the value of the invariant ϵ^{e^-} (2.19). The Thomson regime is associated with $\epsilon^{e^-} \ll 1$, whereas KN regime is characterized by $\epsilon^{e^-} \gg 1$. In the Thomson regime, the scattering is elastic in the ERF, i.e., the scattered photon energy is almost equal to the target photon energy ($\epsilon_s^{e^-} \approx \epsilon^{e^-}$; Böttcher et al., 2012; Rybicki and Lightman, 1991).

Although the ERF is generally a convenient frame to evaluate the KN cross-section, for the interests of our study, we now need to calculate the differential KN cross-section in the lab frame, and then approximate it while considering the head-on approximation limits. The KN cross-section in the lab frame is described as (Böttcher et al., 2012; Dermer and Menon, 2009):

$$\frac{d\sigma_C}{d\Omega_s d\epsilon_s} = \frac{\epsilon_s}{\epsilon_s^{e^-}} \left(\frac{d\sigma_C}{d\Omega_s^{e^-} d\epsilon_s^{e^-}} \right). \tag{2.23}$$

Head-on Approximation: Consider electron energy for $\gamma \gg 1$, as its normalized speed approaches 1, e.g., $\beta \to 1$, such that the incoming photon will appear to be moving in nearly the opposite direction of the scattering electron in the ERF due to photon relativistic aberration, which is described as $\mu^{e^-} \approx -1$ (Equation 2.22a) in the limit $\gamma \gg 1$ (Böttcher et al., 2012; Dermer and Menon, 2009). Therefore, when electrons are highly relativistic, it is generally accepted that all scattered photons will have the same direction as the scattering electron, which means $\Omega_s = \Omega_e$. The head-on approximation of the differential KN cross-section in the lab frame is described as (Böttcher et al., 2012; Dermer and Menon, 2009):

$$\left(\frac{d\sigma_C}{d\Omega_s d\epsilon_s} \right)_{\text{head-on}} = \delta(\Omega_s - \Omega_e) \frac{d\sigma_C}{d\epsilon_s} \tag{2.24}$$

where

$$\frac{d\sigma_c}{d\epsilon_s} = \frac{\pi r_e^2}{\gamma \epsilon^{e^-}} \left[y + \frac{1}{y} - \frac{2\epsilon_s}{\gamma \epsilon^{e^-} y} + \left(\frac{\epsilon_s}{\gamma \epsilon^{e^-} y} \right)^2 \right] H\left(\epsilon_s; \frac{\epsilon^{e^-}}{2\gamma}, \frac{2\gamma \epsilon^{e^-}}{1 + 2\epsilon^{e^-}} \right) \tag{2.25}$$

with $y = 1 - \epsilon_s/\gamma$ and $\epsilon^{e^-} = \gamma\epsilon(1 - \beta\mu)$ (Equation 2.19), and the Heaviside function is described as

$$H(x; x_1, x_2) = \begin{cases} 1 & \text{for } \; x_1 \leq x \leq x_2 \\ 0 & \text{otherwise} \end{cases}. \tag{2.26}$$

Following is the calculation of the Compton spectrum in the head-on approximation.

2.1.3.2 Inverse Compton Emissivity

Now, our objective is to determine the emission coefficient of the IC scattering in the head-on approximation. To do this, we will examine an electron distribution represented by $n_e(\gamma, \Omega_e)$ and a target photon distribution denoted by $n_{\mathrm{ph}}(\epsilon, \Omega_{\mathrm{ph}})$, both of which have directions denoted by angles $\Omega_e = (\varphi_e, \phi_e)$ and $\Omega_{\mathrm{ph}} = (\varphi_{\mathrm{ph}}, \phi_{\mathrm{ph}})$, as demonstrated in Figure 2.5. As commonly assumed, let the $z-$axis be aligned with the bulk motion of the jet along β_Γ. In general, we can describe the spectrum of IC scattered photons in the direction of $\Omega_s = (\varphi_s, \phi_s)$ at frequency $\nu = m_e c^2 \epsilon_s / h$ as (Böttcher et al., 2012):

$$j_{\mathrm{IC}}(\epsilon_s, \Omega_s) = hc\epsilon_s \int_{4\pi} d\Omega_e \int_1^\infty n_e(\gamma, \Omega_e) d\gamma \int_{4\pi} d\Omega_{\mathrm{ph}} \int_0^\infty n_{\mathrm{ph}}(\epsilon, \Omega_{\mathrm{ph}})(1 - \beta\mu) \frac{d\sigma_C}{d\Omega_s d\epsilon_s} d\epsilon. \tag{2.27}$$

Here, $d\sigma_C/d\Omega_s d\epsilon_s$ represents the differential Compton scattering cross-section in the lab frame (Equation 2.23), and μ is determined by Equation 2.21. Finally, assuming the isotropic electron distribution as $n_e(\gamma, \Omega_e) = n_e(\gamma)/4\pi$ in the Lab frame, and applying the head-on approximation on Equation 2.27, one may describe the emission coefficient of the IC scattered high-energy photon as (Böttcher et al., 2012):

$$j_{\mathrm{IC}}^{\text{head-on}}(\epsilon_s, \Omega_s) = \frac{hc\epsilon_s}{4\pi} \int_1^\infty n_e(\gamma) d\gamma \int_{-1}^{+1} d\eta_{\mathrm{ph}} \int_0^{2\pi} d\phi_{\mathrm{ph}} \int_0^\infty n_{\mathrm{ph}}(\epsilon, \Omega_{\mathrm{ph}})(1 - \beta\mu) \frac{d\sigma_C}{d\epsilon_s} d\epsilon, \tag{2.28}$$

where $\eta_{\mathrm{ph}} = \cos\varphi_{\mathrm{ph}}$, as defined in Figure 2.5, and μ and $d\sigma_C/d\epsilon_s$ are given by Equations 2.21 and 2.25, respectively. Furthermore, without loss of generality, we chose $\phi_s = 0$, keeping in mind that $\Omega_s = \Omega_e$. We will use this expression to calculate the SSC spectrum for anisotropic (varying) target photon fields defined by spectrum denoted as

$$n_{\mathrm{ph}}(\epsilon, \varphi) = \frac{j_\nu^{\mathrm{syn}}(\varphi)}{m_e c^2 \epsilon} \langle t_{\mathrm{esc}} \rangle \tag{2.29a}$$

or

$$n_{\mathrm{ph}}(\nu^{\mathrm{syn}}, \varphi) = \frac{j_\nu^{\mathrm{syn}}(\varphi)}{h\nu^{\mathrm{syn}}} \langle t_{\mathrm{esc}} \rangle, \tag{2.29b}$$

where ν^{syn} is the synchrotron frequency, $j_\nu^{\mathrm{syn}}(\varphi)$ is given by Equation 2.10, h denote the Planck constant, and $\langle t_{\mathrm{esc}} \rangle = \tau_{\mathrm{esc}}(R_{\mathrm{b}}/c)$ represent the average photon escape time for a sphere with τ_{esc} the parameter of the escape time scale and R_{b} the blob radius, i.e., the radius of the emitting region. As implied by this equation, the SSC emission level is therefore in direct relationship with $\langle t_{\mathrm{esc}} \rangle$. Thus, the longer a photon takes to escape, the higher the emission levels.

2.2 Blazar Emission Models

As previously mentioned, the blazar SEDs are defined by two broad prominent humps. The first hump is related to the low-frequency (radio−UV/X-ray) emission component, whereas the second hump is associated with the high-frequency (X-ray−gamma-ray) emission component. The first hump is the consequence of a non-thermal distribution of relativistic electrons producing synchrotron radiation (Böttcher, 2007; Böttcher et al., 2012, 2013a). Evidence supporting the notion that the first hump is due to synchrotron radiation comes from measurements of very high PDs, which can reach up to 50% in the energy bands ranging from radio to optical (Böttcher et al., 2012).

Regarding the second hump, it is generally believed that there exist two fundamentally distinct blazar emission models that can account for it, namely, leptonic models and hadronic models. Figure 1.8 demonstrates the spectral fitting of both models. These models are discussed in the two following subsections.

2.2.1 Leptonic Models

In these models, the radiation mechanism is dominated by relativistic leptons (electrons and positrons) throughout the entire EM spectrum (Böttcher et al., 2013a). The high-frequency emission component results from the IC scattering by the same relativistic electrons (and/or positrons) that produce the first SED hump. The scattering can occur on the synchrotron photons produced in the jet, e.g., SSC mechanism, or on external target photon fields found near the accreting SMBH (Böttcher, 2007). Although hadrons such as protons and nuclei may be present in the jet, they do not contribute to the emission as they cannot be accelerated to sufficiently high energies (Böttcher et al., 2012, 2013a). However, it is important to note that since protons can sometimes carry more kinetic energy and dominate the momentum of the jet, their energy must be included in the total energy calculations. In spectral fitting with leptonic models, a relatively low magnetic field strength is usually assumed, typically in the range of milli-Gauss to Gauss levels (Böttcher et al., 2013a).

The synchrotron and SSC (S+SSC) leptonic blazar model typically defines the X-ray and gamma-ray emission component well, but only in the case of HBLs. In the case of FSRQs, LBLs, and IBLs, almost always an additional external Compton component is required to fit their X-ray and gamma-ray spectra (Boettcher, 2012; Böttcher et al., 2013a).

2.2.2 Hadronic Models

It is generally accepted in cases of hadronic emission models that the second hump observed in blazar SEDs is mainly caused by extremely energetic protons that exceed the threshold for photo-pion production on the target photon field in the emitting region (Böttcher et al., 2013a). These protons generate the radiation through either proton-synchrotron or photomeson mechanisms. Depending on the parameters of the model, the high-energy component in the hadronic model can also result from the relativistic electrons emitting SSC radiation (Böttcher et al., 2013a). In the proton synchrotron model, a strong magnetic field of approximately 10 Gauss or more is required to accelerate protons to the necessary extreme relativistic energies (Böttcher, 2007; Böttcher et al., 2013a). The production of neutrinos in jets is predicted by hadronic models.

2.3 Polarization

Polarization is a basic property of light that is defined by the direction of the electric field vector of an EM wave. A light wave is a transverse EM wave consisting of electric and magnetic vibrations occurring perpendicular to each other, and to the direction of propagation (Griffiths, 2021; Nave, 2017). With the use of Maxwell's equations in a vacuum (Griffiths, 2021; Jackson, 2021; Rybicki and Lightman, 1991):

$$\nabla \cdot \vec{E} = 0, \tag{2.30a}$$

$$\nabla \cdot \vec{B} = 0, \tag{2.30b}$$

$$\nabla \times \vec{E} = -\frac{\partial \vec{B}}{\partial t}, \tag{2.30c}$$

$$\nabla \times \vec{B} = \varepsilon_0 \mu_0 \frac{\partial \vec{E}}{\partial t} = \frac{1}{c^2}\frac{\partial \vec{E}}{\partial t}, \tag{2.30d}$$

we can calculate the wave equations of EM waves. Here, $\vec{E}$ and $\vec{B}$ are electric field and magnetic field vectors and $c = \frac{1}{\sqrt{\varepsilon_0 \mu_0}}$ (Griffiths, 2021) is the speed of light, together with permeability ε_0 and permittivity μ_0 of free space. This relation of c with both ε_0 and μ_0 tells us that EM waves travel at the speed of light in free space (Griffiths, 2021). Taking the curl of Equation (2.30c) and combining it with Equation (2.30d), and vice versa, we have

$$\nabla \times (\nabla \times \vec{E}) = \nabla \times \left(-\frac{\partial \vec{B}}{\partial t}\right) \tag{2.31a}$$

$$\nabla(\nabla \cdot \vec{E}) - \nabla^2 \vec{E} = -\frac{\partial}{\partial t}(\nabla \times \vec{B}) = -\frac{1}{c^2}\frac{\partial^2 \vec{E}}{\partial t^2} \tag{2.31b}$$

and

$$\nabla \times (\nabla \times \vec{B}) = \nabla \times \left(\frac{1}{c^2}\frac{\partial \vec{E}}{\partial t}\right) \tag{2.32a}$$

$$\nabla(\nabla \cdot \vec{B}) - \nabla^2 \vec{B} = \frac{1}{c^2}\frac{\partial}{\partial t}(\nabla \times \vec{E}) = -\frac{1}{c^2}\frac{\partial^2 \vec{B}}{\partial t^2}, \tag{2.32b}$$

with the use of vector identity $\nabla \times (\nabla \times \vec{A}) = \nabla(\nabla \cdot \vec{A}) - \nabla^2 \vec{A}$. Therefore, since $\nabla \cdot \vec{E} = 0$ (Equation 2.30a) and $\nabla \cdot \vec{B} = 0$ (Equation 2.30b), the homogeneous vector wave equations for $\vec{E}$ and $\vec{B}$ are

$$\nabla^2 \vec{E} = \frac{1}{c^2}\frac{\partial^2 \vec{E}}{\partial t^2}, \tag{2.33}$$

$$\nabla^2 \vec{B} = \frac{1}{c^2}\frac{\partial^2 \vec{B}}{\partial t^2}. \tag{2.34}$$

The real solutions of EM wave equations are given by Griffiths (2021) as

$$\vec{E}(\vec{r}, t) = E_0 \cos(\vec{k} \cdot \vec{r} - \omega t + \vartheta)\hat{\mathbf{n}}, \tag{2.35}$$

$$\vec{B}(\vec{r}, t) = B_0 \cos(\vec{k} \cdot \vec{r} - \omega t + \vartheta)(\hat{\mathbf{k}} \times \hat{\mathbf{n}}), \tag{2.36}$$

with E_0 and B_0 the amplitudes of the wave equations of $\vec{E}$ and $\vec{B}$, wave or propagation vector $\vec{k}$, polarization direction $\hat{\mathbf{n}}$, angular frequency ω, time t, arbitrary phase ϑ, propagation direction $\hat{\mathbf{k}}$, and position vector $\vec{r} = (x, y, z)$ in rectangular coordinates. For transverse EM waves, i.e., when the EM field vector is at right-angle to the propagation direction, one can conclude that $\hat{\mathbf{n}} \cdot \hat{\mathbf{k}} = 0$ and $\vec{B} = (\hat{\mathbf{k}} \times \vec{E})/c$ (Griffiths, 2021).

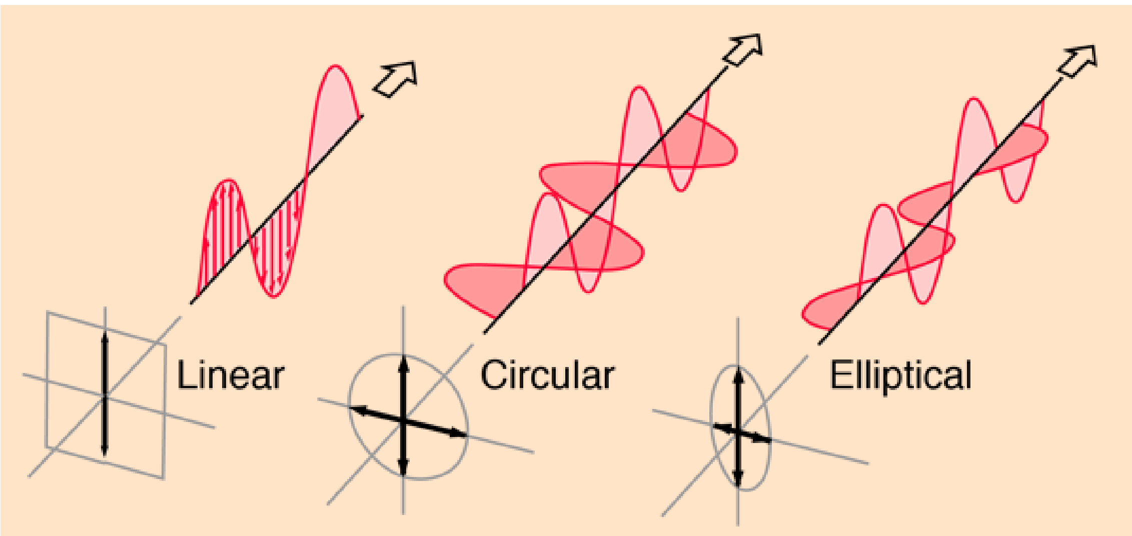

Figure 2.6: Three main types of polarization of an EM wave. From Nave (2017).

A light wave can either be (the general state) elliptically polarized, circularly polarized, or linearly polarized depending on the relative phase between oscillations in two perpendicular directions (see Figure 2.6). Say $\vec{E}$ is at an arbitrary point $\vec{r} = 0$, such that it can be decomposed into its $x-$ and $y-$directions (see Figure 2.7; Rybicki and Lightman, 1991; Trippe, 2014):

$$\vec{E}_x(t) = E_0^x \cos(\omega t - \vartheta_x)\hat{\mathbf{x}}, \tag{2.37a}$$
$$\vec{E}_y(t) = E_0^y \cos(\omega t - \vartheta_y)\hat{\mathbf{y}}, \tag{2.37b}$$

where $\vartheta_{x,y}$ are a priori arbitrary phases. The net electric field vector's tip in the

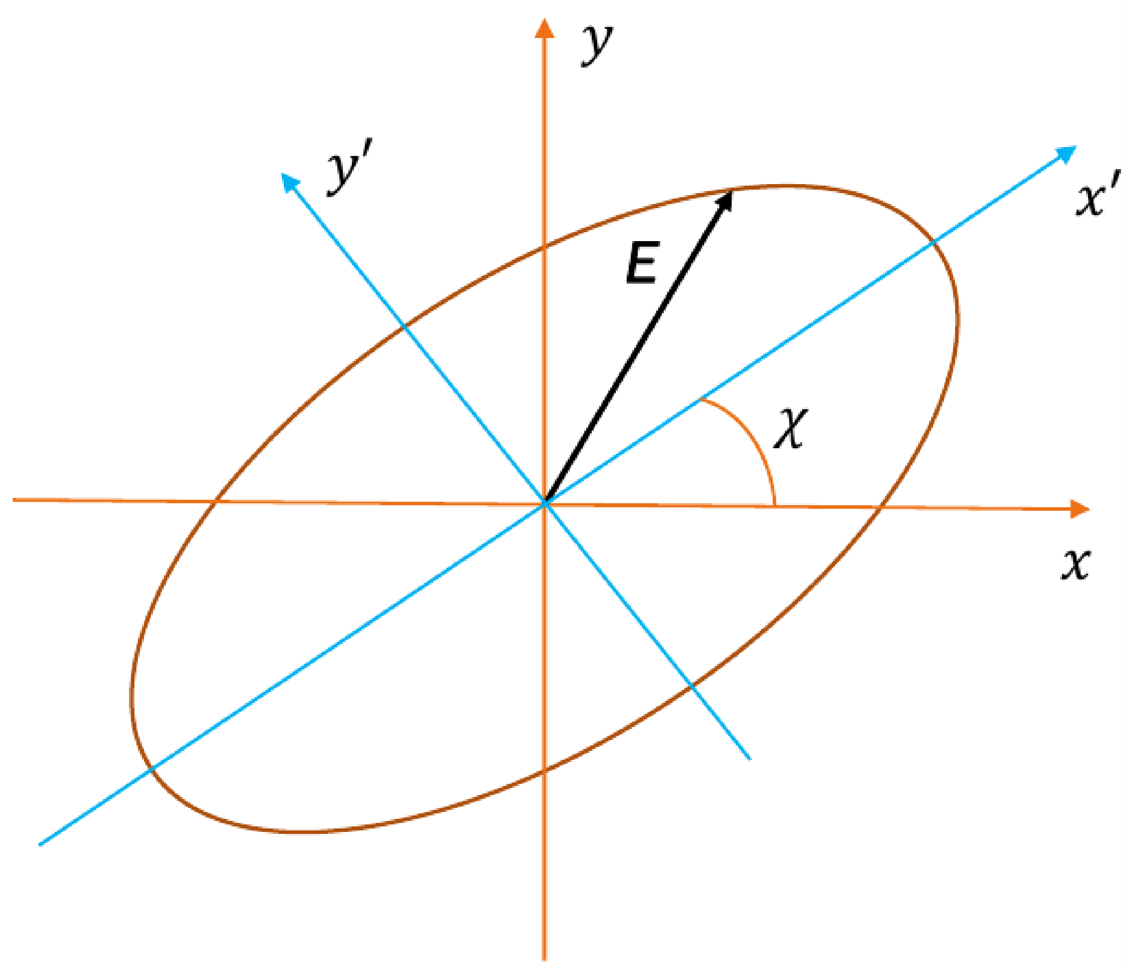

Figure 2.7: Electric field components in the $x-$ and $y-$directions rotating through the polarization angle χ to align with the primary axes of elliptical polarization. From Rybicki and Lightman (1991).

$x-y$ plane is described by these equations and therefore, it follows an elliptical path. Thus, the elliptical case of polarization of light is the most general form (Longair, 2010; Tinbergen, 2005; Trippe, 2014), for which between the two linear electric field vector components the amplitude and phase angle are not equal (Fitzpatrick, 2013; Nave, 2017), e.g., when $E_0^x \neq E_0^y$ and $\vartheta_x \neq \vartheta_y$. Circular and linear polarization are specialized cases of this general state. Circular polarization is the result of the polarization ellipse degenerating into a circle (Trippe, 2014); when $\vec{E}_x$ and $\vec{E}_y$ are equal in amplitude with a phase difference of 90° between them (Fitzpatrick, 2013; Nave, 2017), e.g., when $E_0^x = E_0^y$ and $\vartheta_y = \vartheta_x \pm 90°$. For linear polarization, the ellipse degenerates into a line (Trippe, 2014). This happens when $\vec{E}_x$ and $\vec{E}_y$ are in phase, e.g., if $\vartheta_x = \vartheta_y$, such that the magnitude of the transverse $\vec{E}$ at a specific location changes only in a sinusoidal manner over time, while keeping the same orientation.

The polarization of light waves can be determined with the use of a powerful tool called polarimetry. This tool gives us direct observations of the magnetic field geometry in the emission region (Böttcher et al., 2012), with the degree of polarization indicating the extent to which the EM radiation is polarized. Thus, EM radiation can have both polarized and non-polarized components. When the PD is 100%, the radiation is fully polarized, and when the PD is 0%, it is fully non-polarized. However, if the degree of polarization is between 0% and 100%, the radiation is said to be partially polarized (Tinbergen, 2005). In our study, we only consider linear polarization because synchrotron radiation, the non-thermal process being studied, is often linearly polarized with only a very small degree of circular polarization.

2.3.1 Synchrotron Polarization

The mechanism of synchrotron radiation produced by relativistic electrons is well-known for its highly linearly polarized. However, the emission of an electron is elliptically polarized as it moves along a magnetic field line (Rybicki and Lightman, 1991). When considering relativistic electrons with emission cones of an angle $1/\gamma$ along the LoS to the observer as shown in Figure 2.1, only radiation within an angle $1/\gamma$ is observed (Longair, 2010). If there is a distribution of pitch angles, all electrons within the $1/\gamma$ emission cone contribute to the observed radiation, which is elliptically polarized in opposite directions (left-handed and right-handed directions, normally) on either side within the cone (Longair, 2010; Rybicki and Lightman, 1991). Upon averaging over all electrons, the components of elliptical polarization parallel to the magnetic field vector cancel out, resulting in (mostly) linear polarization perpendicular to the magnetic field (Longair, 2010). Thus, the polarization can be calculated by measuring the radiative powers in radiation with electric-field vectors parallel $P_{\nu,||}$ and perpendicular $P_{\nu,\perp}$ to the magnetic field as projected onto the plane of the sky (Böttcher et al., 2012; Longair, 2010; Rybicki and Lightman, 1991), as shown in Figure 2.8. These powers are given by Rybicki and Lightman (1991) as

$$P_{\nu,||}(\gamma,\varphi) = \frac{\sqrt{3}e^3B}{2m_ec^2}\sin(\varphi)[F(x) - G(x)] \tag{2.38a}$$

and

$$P_{\nu,\perp}(\gamma,\varphi) = \frac{\sqrt{3}e^3 B}{2m_e c^2}\sin(\varphi)[F(x)+G(x)], \tag{2.38b}$$

where

$$G(x) = G(x_\varphi(\gamma)) = x_\varphi(\gamma)K_{2/3}(x_\varphi(\gamma)) \tag{2.39}$$

with $K_{2/3}$ being the modified Bessel function of the second kind with an order of 2/3. The synchrotron polarization for particles with a single energy γ is calculated as

$$\Pi_\nu^{\mathrm{syn}}(\gamma,\varphi) = F_B\left[\frac{P_{\nu,\perp}(\gamma,\varphi) - P_{\nu,||}(\gamma,\varphi)}{P_{\nu,\perp}(\gamma,\varphi) + P_{\nu,||}(\gamma,\varphi)}\right] = F_B\left[\frac{G(x)}{F(x)}\right] \tag{2.40}$$

by Longair (2010) and Rybicki and Lightman (1991), where F_B is the dimensionless constant that measures how well the magnetic field is ordered and is considered to be 1 throughout the study. $P_{\nu,\perp}(\gamma,\varphi)+P_{\nu,||}(\gamma,\varphi)$ gives the total synchrotron power emitted by single-electron (Equation 2.4). For an extended energy distribution of electrons, we have

$$\Pi_\nu^{\mathrm{syn}}(\varphi) = \frac{\langle G(x)\rangle}{\langle F(x)\rangle}, \tag{2.41}$$

where

$$\langle G(x)\rangle = \int n_e(\gamma)G(x)d\gamma = n_0\int_{\gamma_{\min}}^{\gamma_{\max}} \gamma^{-p}x_\varphi(\gamma)K_{2/3}(x_\varphi(\gamma))d\gamma, \tag{2.42a}$$

$$\langle F(x)\rangle = \int n_e(\gamma)F(x)d\gamma = n_0\int_{\gamma_{\min}}^{\gamma_{\max}} \gamma^{-p}x_\varphi(\gamma)\int_{x_\varphi(\gamma)}^{\infty} K_{5/3}(\xi)d\xi d\gamma \tag{2.42b}$$

For an electron distribution following a power-law with spectral index p, the theoretical maximum synchrotron polarization is (Böttcher et al., 2012; Longair, 2010; Rybicki and Lightman, 1991);

$$\Pi_{\max}^{\mathrm{syn}} = \frac{p+1}{p+7/3}, \tag{2.43}$$

which does not depend on the distribution of electron pitch angles. For a typical power-law index of $p = 2.5$, the highest degree of polarization in a perfectly ordered magnetic field is around 72.4%. However, variations in the magnetic field orientation result in a decrease on the total degree of polarization, causing the observed polarization to be much smaller (Böttcher et al., 2012). This polarization is particularly noticeable in RL AGNs, e.g., the polarization levels appear to decrease toward higher frequencies in the near-IR−optical−UV spectrum (Netzer, 2015).

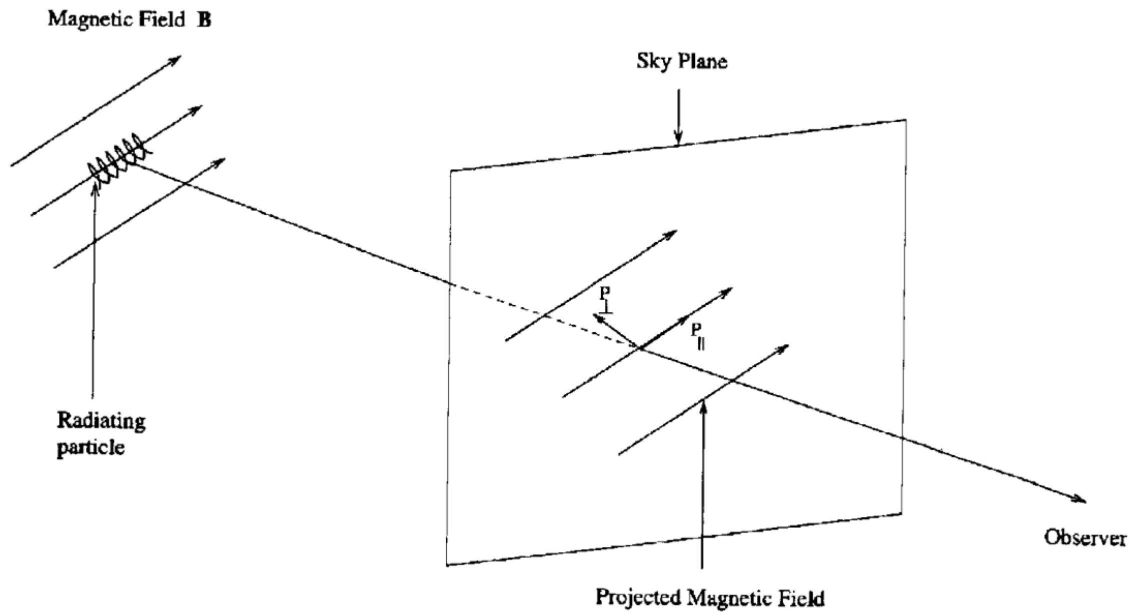

Figure 2.8: Projection of the vectors relevant to synchrotron radiation on the plane of the sky magnetic field. From Rybicki and Lightman (1991).

2.3.2 Synchrotron Self-Compton Polarization

Compton scattering, like synchrotron radiation, also has a dependence on polarization. Linear polarization is produced by synchrotron radiation from relativistic electrons in perfectly uniform magnetic fields, while Compton scattering from these same electrons will only decrease the PD of the target photon field by a minimum of 50% (Böttcher, 2019; Bonometto and Saggion, 1973). This decrease arises because the photons that were initially polarized in a specific direction are scattered in various directions due to the helical motion of the electrons in the magnetic field (see Section 2.1.1). Hence, the degree of polarization of IC scattering from relativistic electrons (or SSC radiation) Π^{SSC} and synchrotron radiation Π^{syn} may be related as

$$\Pi^{\mathrm{SSC}}(\nu^{\mathrm{SSC}}) \approx \frac{1}{2}\Pi^{\mathrm{syn}}(\nu^{\mathrm{syn}}), \tag{2.44}$$

where, in the context of the Thomson regime, $\nu^{\mathrm{SSC}} \sim \gamma^2 \nu^{\mathrm{syn}}$ is the SSC frequency with electron energy γ and synchrotron frequency ν^{syn}. Compton scattering may only produce polarization in the scenario where non-relativistic electrons are scattered (Böttcher, 2019; Krawczynski, 2011). When an isotropic distribution of relativistic electrons (and positrons) scatters non-polarized target photons, the resulting Compton emission will always be non-polarized.

Bonometto and Saggion (1973) developed formulae for determining the degree of polarization of SSC radiation in the Thomson regime. Krawczynski (2011) validated those formulae in detail through Monte-Carlo simulations. Zhang and Boettcher

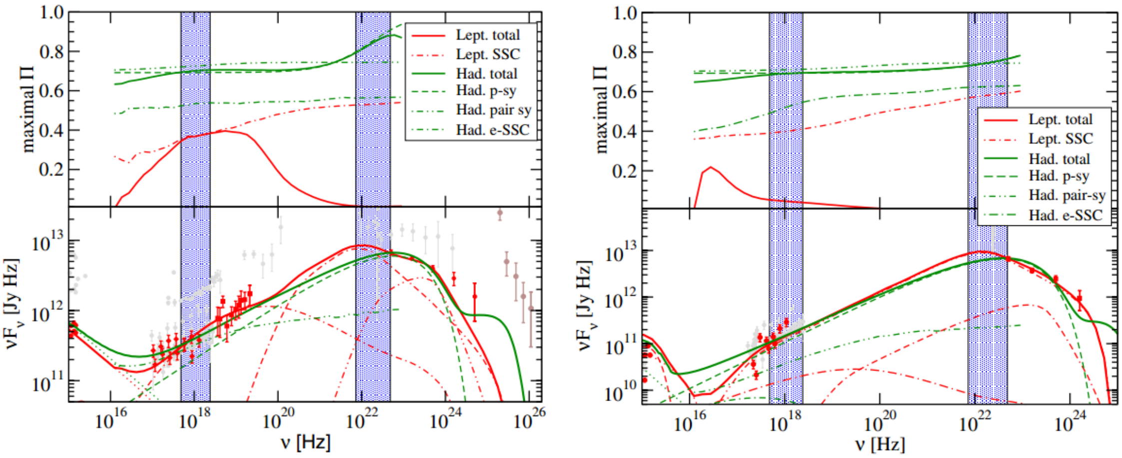

Figure 2.9: Leptonic (red) and hadronic model (green) fits to the SEDs (lower panels) and X-ray and gamma-ray polarization (upper panels) for FSRQs 3C 279 (left) and PKS 0528+134 (right) in the UV through gamma-ray energy bands. Blue vertical shaded regions show the $2-10$ keV X-ray band and $30-200$ MeV gamma-ray band. From Zhang and Boettcher (2013).

(2013) evaluated the theoretical upper limits of polarization signatures of blazar emission (leptonic and hadronic) models in the X-ray through gamma-ray bands. The results indicate that the leptonic model predicts a low upper limit of high-energy PD of 40% or less, in a perfectly ordered magnetic field, whereas the hadronic model predicts a high upper limit of X-ray and gamma-ray PD of 75% or less (see Figure 2.9). Moreover, the high-energy PD results from the Compton scattering in the leptonic models, whereas in hadronic models it results from proton and cascade synchrotron emission.

Chapter 3

Single-zone Synchrotron and Synchrotron Self-Compton Emission Model

In this chapter, we describe the formalism used to evaluate the angle-dependent spectra and degree of polarization from synchrotron radiation and IC scattering. These calculations will be advanced by taking into account the anisotropy of the radiation produced and the polarization under the influence of the synchrotron and SSC (and, for future analysis, synchrotron self-absorption, and gamma-ray absorption). To achieve this, we start with the inclusion of the effects of considered orientations of the magnetic field (oblique, parallel, and perpendicular fields) relative to the jet axis in the expression of the synchrotron emissivity (Equation 2.10), and the calculation of the pitch angle φ for each magnetic field geometry. Moreover, to save computation time, we will approximate $F(x)$ defined by Equation 2.7, and then calculate the normalization factor n_0 from Equation 2.1. We end this chapter with a presentation of fixed parameters for our generic blazar model.

3.1 Magnetic Field Geometries and Pitch Angle

Here, our objective is to calculate the pitch angle for oblique, parallel, and perpendicular magnetic field geometries. Consider a single spherical zone of the emission region moving along the jet with a relativistic speed of $\beta_\Gamma c$. This speed corresponds to the jet Lorentz factor Γ of the emitting region. Let the spherical coordinates be r, ψ, and ϕ, centered on the jet axis. The corresponding cartesian coordinates are defined as x, y, and z, with the $z-$axis being along the jet axis. As Jamil and Boettcher (2012) assumed, we as well assume that the only source of photons in our study is the synchrotron emission. The general form of propagation vector of the synchrotron photon in spherical coordinates is commonly written as

$$\hat{\boldsymbol{\kappa}} = (\sin\psi_{\text{ph}}\cos\phi_{\text{ph}}, \sin\psi_{\text{ph}}\sin\phi_{\text{ph}}, \cos\psi_{\text{ph}}). \tag{3.1}$$

We also assume that the chosen magnetic field geometry remains the same across the emitting region. Therefore, for any given magnetic field vector $\vec{B}$ with the unit vector $\hat{\mathbf{B}}$ along its direction, the cosine of the pitch angle is given as

$$\cos(\varphi) = \hat{\boldsymbol{\kappa}} \cdot \hat{\mathbf{B}}. \tag{3.2}$$

The general magnetic field geometry including both parallel and perpendicular fields is purely oblique fields which can be described as (Joshi et al., 2016, 2020):

$$\vec{B} = B(\sin\psi_B\cos\phi_B, \sin\psi_B\sin\phi_B, \cos\psi_B), \tag{3.3}$$

where the field vector with magnitude B is oriented at an angle ψ_B relative to the jet axis and at an angle ϕ_B in the $xy-$plane, and parallel and perpendicular field geometries are obtained when ψ_B is equal to $0°$ and $90°$, respectively. The cosine and the sine of the pitch angle for an oblique geometry are obtained as

$$\cos\varphi = \sin\psi_{\text{ph}}\cos\phi_{\text{ph}} \cdot x_B + \sin\psi_{\text{ph}}\sin\phi_{\text{ph}} \cdot y_B + \cos\psi_{\text{ph}} \cdot z_B, \tag{3.4a}$$
$$\sin\varphi = \sqrt{1 - (\sin\psi_{\text{ph}}\cos\phi_{\text{ph}} \cdot x_B + \sin\psi_{\text{ph}}\sin\phi_{\text{ph}} \cdot y_B + \cos\psi_{\text{ph}} \cdot z_B)^2}, \tag{3.4b}$$

where $x_B = \sin\psi_B\cos\phi_B$, $y_B = \sin\psi_B\sin\phi_B$, and $z_B = \cos\psi_B$. For a parallel magnetic field geometry, the field vector can be described as $\vec{B} = B(0, 0, 1)$ with its unit vector $\hat{\mathbf{B}} = (0, 0, 1)$. Thus, the cosine and sine of the pitch angle for the parallel field are given as

$$\cos\varphi = \cos\psi_{\text{ph}}, \tag{3.5a}$$
$$\sin\varphi = \sqrt{1 - \cos^2\psi_{\text{ph}}}. \tag{3.5b}$$

From these two equations, one can therefore simply conclude that φ is equivalent to ψ_{ph}. Thus, if the magnetic field is aligned with the jet axis, the expression of the synchrotron emissivity does not need to be modified, only the substitution of the pitch angle φ with the synchrotron photon angle ψ_{ph} relatively to the jet axis is necessary. In the case of a perpendicular magnetic field geometry, we have $\vec{B} = B(\cos\phi_B, \sin\phi_B, 0)$ with $\hat{\mathbf{B}} = (\cos\phi_B, \sin\phi_B, 0)$. In this case, the cosine and sine of the pitch angle can be expressed as

$$\cos\varphi = \sin(\psi_{\text{ph}})\cos(\phi_{\text{ph}} - \phi_B), \tag{3.6a}$$
$$\sin\varphi = \sqrt{1 - \sin^2(\psi_{\text{ph}})\cos^2(\phi_{\text{ph}} - \phi_B)}. \tag{3.6b}$$

Since the synchrotron spectrum is altered by the orientations of the magnetic field, the photon spectrum and the SSC/IC spectrum are also influenced by these orientations. Now, after the elimination of ψ_{ph} from the SSC emissivity (Equation 2.28) through the integration, e.g., after the calculations of the SSC emissivity, we set $\psi_{\mathrm{ph}} = \varphi_s = \psi_{obs}$, where φ_s is the scattered photon angle (see Section 2.1.3) and ψ_{obs} is our viewing angle in the plasma frame. This correspondence arises from the fact that the emissions resulting from both synchrotron radiation and SSC mechanisms can be observed along the same direction within the same physical region of the source. Consequently, this correspondence implies that $\phi_{obs} = \phi_{\mathrm{ph}}$, where ϕ_{obs} is the observer's azimuthal angle, and is consistently set to 0° throughout this study.

3.2 Approximation of $F(x)$ and n_0 Calculation

Due to the known computationally time-consuming nature of Bessel functions, we have approximated the synchrotron spectral function $F(x)$, e.g., Equation 2.7, in order to minimize computation time as

$$F_{\mathrm{approx}}(x) = 1.42\sqrt{\frac{\pi}{2}}x^{3/10}e^{-x}. \tag{3.7}$$

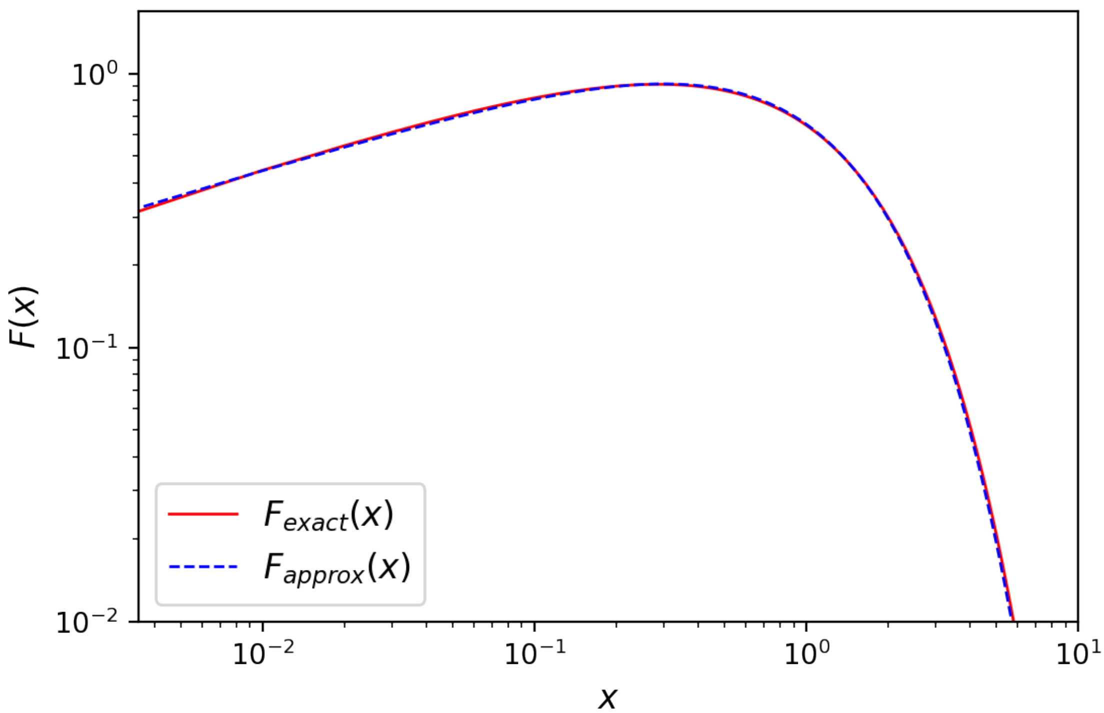

Figure 3.1: Illustration of the exact spectral power $F_{\mathrm{exact}}(x)$ with its approximation $F_{\mathrm{approx}}(x)$ in the range of 3.5×10^{-3} to 10.

Figure 3.1 displays the comparison of the synchrotron spectral function and its approximation function (Equation 3.7) in the range of 3.5×10^{-3} to 10. As can be seen, in this range, $F_{\text{approx}}(x)$ is sufficiently accurate for the purpose of our study. Therefore, in order to verify its accuracy, we compared the exact synchrotron emissivity with its approximated emissivity in the case of a parallel magnetic field w.r.t. the jet axis, as shown in Figure 3.2. The synchrotron low-energy and high-energy cutoffs are indicated by the orange and black dashed-vertical lines, respectively. These lines are determined by Equation 2.16 and are as well affected by the field geometry w.r.t. the jet axis. Based on both Figures 3.1 and 3.2, particularly Figure 3.2, we can conclude that our approximation of $F(x)$ is accurate and reliable.

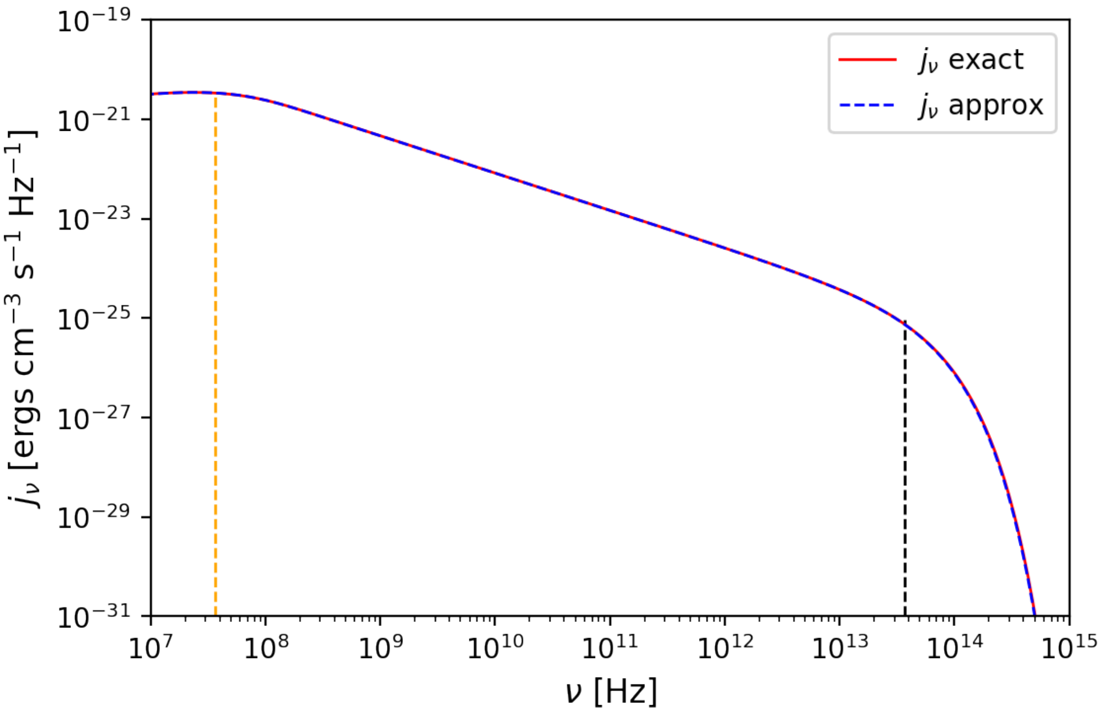

Figure 3.2: The comparison between the exact synchrotron emission coefficient (j_ν exact) and the approximated synchrotron emission coefficient (j_ν approx).

The parameters chosen for the creation of Figure 3.2 are the viewing angle of $\psi_{obs} = 5°$, the magnetic field strength of $B = 1$ G, the power-law index of $p = 2.5$, the low- and high-energy cutoffs of $\gamma_{\text{min}} = 10$ and $\gamma_{\text{max}} = 10^4$, and the normalization factor of $n_0 = 10^4$ cm^{-3}. The values of B, γ_{min}, and γ_{max} will remain the same throughout the study.

As far as the calculation of the power-law normalization factor n_0 is concerned, we start with the definition of the kinetic power in the relativistic electrons in the lab frame (Böttcher et al., 2013a):

$$L_e = \pi R_{\text{b}}^2 \Gamma^2 \beta_\Gamma c m_e c^2 \int n_e(\gamma)\gamma d\gamma, \tag{3.8}$$

where $\beta_\Gamma = \sqrt{1 - 1/\Gamma^2}$. Substituting Equation 2.1 into Equation 3.8 and solving the integral, we have

$$L_e = \pi R_{\rm b}^2 \Gamma^2 \beta_\Gamma c m_e c^2 n_0 f(p), \tag{3.9}$$

where

$$f(p) = \begin{cases} \ln\left(\frac{\gamma_{\rm max}}{\gamma_{\rm min}}\right), & p = 2 \\ \\ \frac{\gamma_{\rm max}^{2-p} - \gamma_{\rm min}^{2-p}}{2-p}, & \text{otherwise.} \end{cases} \tag{3.10}$$

Therefore, the power-law normalization factor can be calculated as

$$n_0 = \frac{L_e}{\pi R_{\rm b}^2 \Gamma^2 \beta_\Gamma c m_e c^2 f(p)}. \tag{3.11}$$

The following is a parameter study with our model.

3.3 Parameter Study

For the purpose of conducting a parameter study, Table 3.1 provides the fixed input parameter values that were chosen to construct our model for a generic (typical) blazar. The power-law index p will remain the same at a value of 2.5 in all considered cases, except in Section 4.5, where we are examining its impacts on the synchrotron and SSC spectra and polarization. Furthermore, for $p = 2.5$, we obtained the corresponding electron power-law normalization factor as $n_0 \approx 9.4 \times 10^4$ cm^{-3} with the use of Equation 3.11.

Parameter	Symbol	Value
Low-energy Cutoff	$\gamma_{\rm min}$	10
High-energy Cutoff	$\gamma_{\rm max}$	10^4
Power-law Index	p	2.5
Magnetic Field	B	1.0 G
Magnetic Field Order	F_B	1.0
Electron Kinetic Power	L_e	10^{44} erg·s^{-1}
Escape Time Scale Parameter	$\tau_{\rm esc}$	0.75
Emission Region Radius	$R_{\rm b}$	10^{16} cm
Bulk Lorentz Factor	Γ	15
Observer's angle in the $xy-$plane	ϕ_{obs}	$0°$

Table 3.1: The fixed parameters of our model for a typical blazar.

The values of our physical parameters such as angles ψ_{obs} and ψ_B are chosen to range from 5° to 85° and 175° in increments of 10°, while an angle ϕ_B ranges from 0° to 180°. However, a slightly different approach will be employed in the calculations of the SSC polarization. As it is typically known that the dominant contribution to the seed photons for SSC emission is from synchrotron photons emitted at pitch angles around 90°, we, therefore, need to properly weighted Equation 2.44 according to the contributions that synchrotron photons from different pitch angles make to the total SSC emission. Finally, the power-law spectral index will be varied in the range of 2.0 to 3.5.

Chapter 4

Results and Discussion

This chapter presents the results and discussion of our parameter analysis using our new angle- and polarization-dependent one-zone synchrotron and SSC model. We intend to investigate the influence of three fundamental parameters, namely, the viewing angle ψ_{obs}, the orientation of the magnetic field (in terms of the angles ψ_B and ϕ_B with respect to the jet-axis and the $xy-$plane, respectively), and the power-law index. Our goal is to comprehend how these parameters impact the SED and PD of a generic blazar. Frequency-dependent degree of polarization signatures will be compared to selected previous studies.

4.1 Parallel Field

The synchrotron emissivity and polarization were studied with different viewing angles ψ_{obs} for a magnetic field closely aligned with the jet axis. Figures 4.1 and

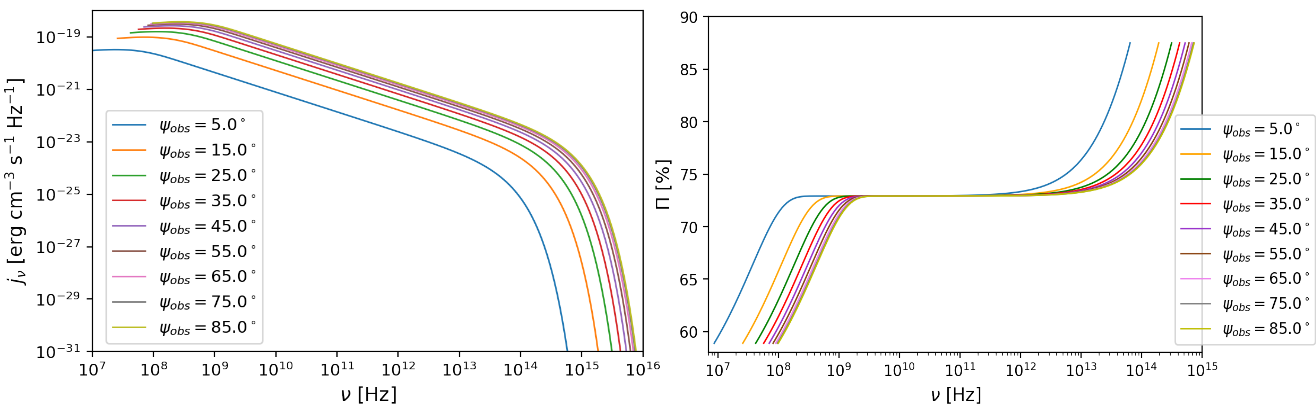

Figure 4.1: Synchrotron emissivity (left panel) and degree of polarization (right panel) for values of ψ_{obs} ranging from 5° to 85° under the influence of the magnetic field aligned with the jet axis.

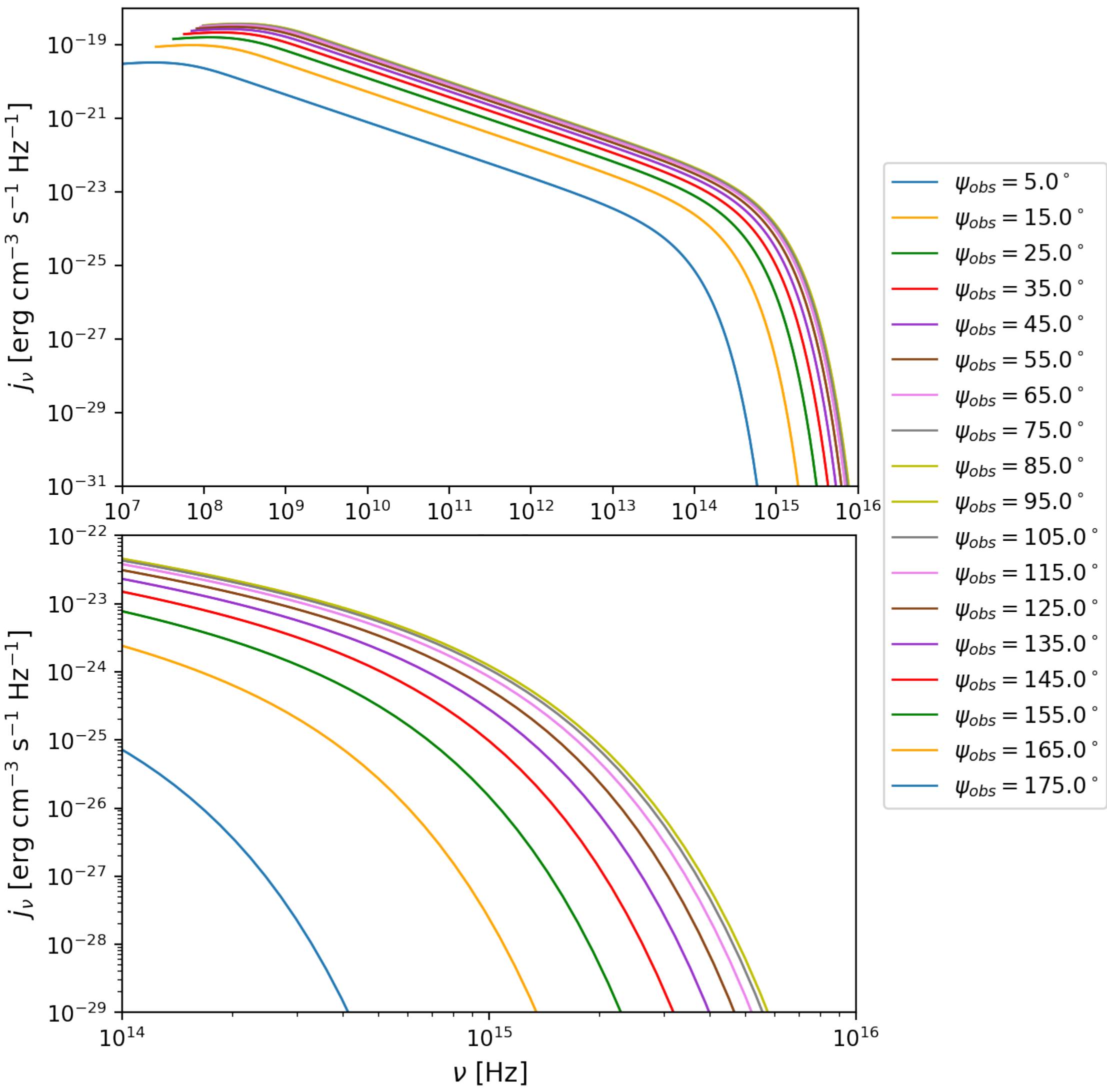

Figure 4.2: The zoomed (lower panel) and non-zoomed (upper panel) plots of the synchrotron emissivity under the influence of the magnetic field aligned with the jet axis for values of ψ_{obs} ranging from 5° to 175°.

4.2 display the outcomes, where the left-hand-side (LHS) plot of Figure 4.1 and the top panel of Figure 4.2 represent the synchrotron emissivity, the right-hand-side (RHS) plot of Figure 4.1 represents the synchrotron polarization, and the bottom panel of Figure 4.2 is the zoomed plot of the upper panel. As implied by Equation 3.5, the sine of the pitch angle ($\sin\varphi$) is equal to the sine of the viewing angle ($\sin\psi_{obs}$) when the magnetic field is parallel w.r.t. the jet axis. Thus, for the viewing angle ranging from 5° to 85°, the sine of the pitch angle increases with an increase in the viewing angle. This led to a rise in the synchrotron radiation along our LoS, with the corresponding cutoff frequencies $\nu_{\text{cut min,max}}$ shifting to higher values. However, the exact opposite happens when the viewing angle varies from 95° to 175°. The synchrotron emissivities observed at the viewing angles ranging from 5° to 85° (hereafter j_1^{syn}) are equivalent to those at angles ranging from 175° down to 95° (hereafter j_2^{syn}). This is clearly illustrated in Figure 4.2 as indicated by the colors of the curves. Additionally, the synchrotron emission shows some convergence at its maximum when the viewing angle is 75° and 85° (or when $\psi_{obs} = 95°, 105°$).

Furthermore, with regard to the polarization profiles, an increase/decrease in the sine of the pitch angle results in the shifts of the PD to the right/left. The polarization signatures when the observed angle is between 95° and 175° have been omitted since the synchrotron emissivities j_1^{syn} are equivalent to emissivities j_2^{syn}, which implies the same is true for the degrees of polarization.

4.2 Perpendicular Field

For the case when the magnetic field is perpendicular to the jet axis, the value of the sine of the pitch angle has an inverse relationship with the observed angle, according to Equation 3.6. Figures 4.3, 4.4, and 4.5 show the manifestation of this field geometry on the synchrotron emission and the synchrotron polarization (right plot of Figure 4.3). As the observed angle ψ_{obs} varies from 5° to 85°, a larger value of

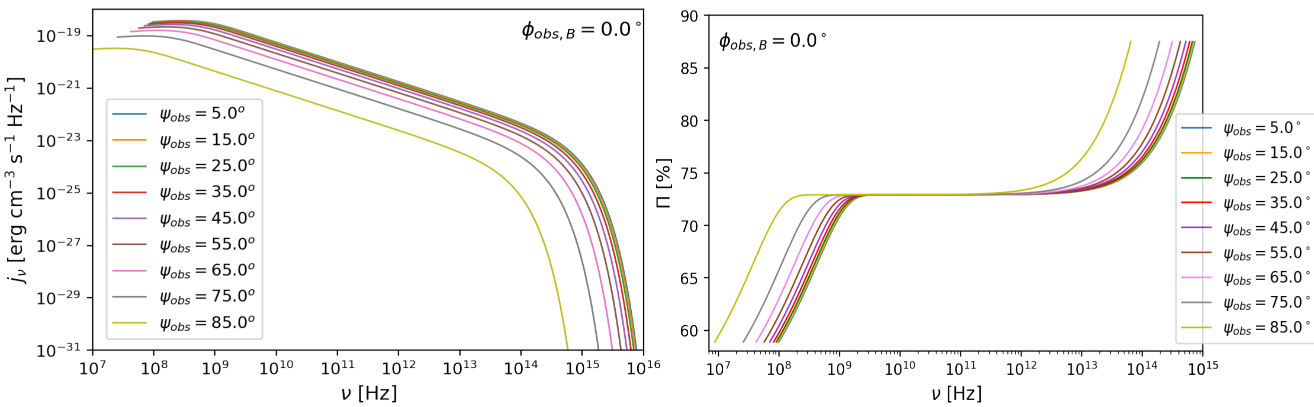

Figure 4.3: The effects of the perpendicular magnetic field w.r.t. the jet axis on the synchrotron emissivity (left panel) and degree of polarization (right panel) for values of ψ_{obs} ranging from 5° to 85° when the azimuthal angles of both the observer ϕ_{obs} and the magnetic field ϕ_B are fixed to 0°.

ψ_{obs} leads to a lower value of the sine of the pitch angle compared to that of a smaller observed angle which leads to a higher value of $\sin\varphi$, as can be seen in the LHS plot of Figure 4.3. Therefore, this leads to a decrease in synchrotron emission level with an increase in the viewing angle. The corresponding synchrotron cutoff frequencies shift to lower values compared to those of synchrotron radiation under the influence of the parallel magnetic field. In fact, the perpendicular and parallel magnetic fields produce inverse results when changing the viewing angle, while keeping the value of ϕ_{obs} the same as that of ϕ_B (see Figures 4.3 and 4.4 for the perpendicular field and Figures 4.1 and 4.2 for the parallel field), except only for the equivalence of emissivities j_1^{syn} and j_2^{syn}.

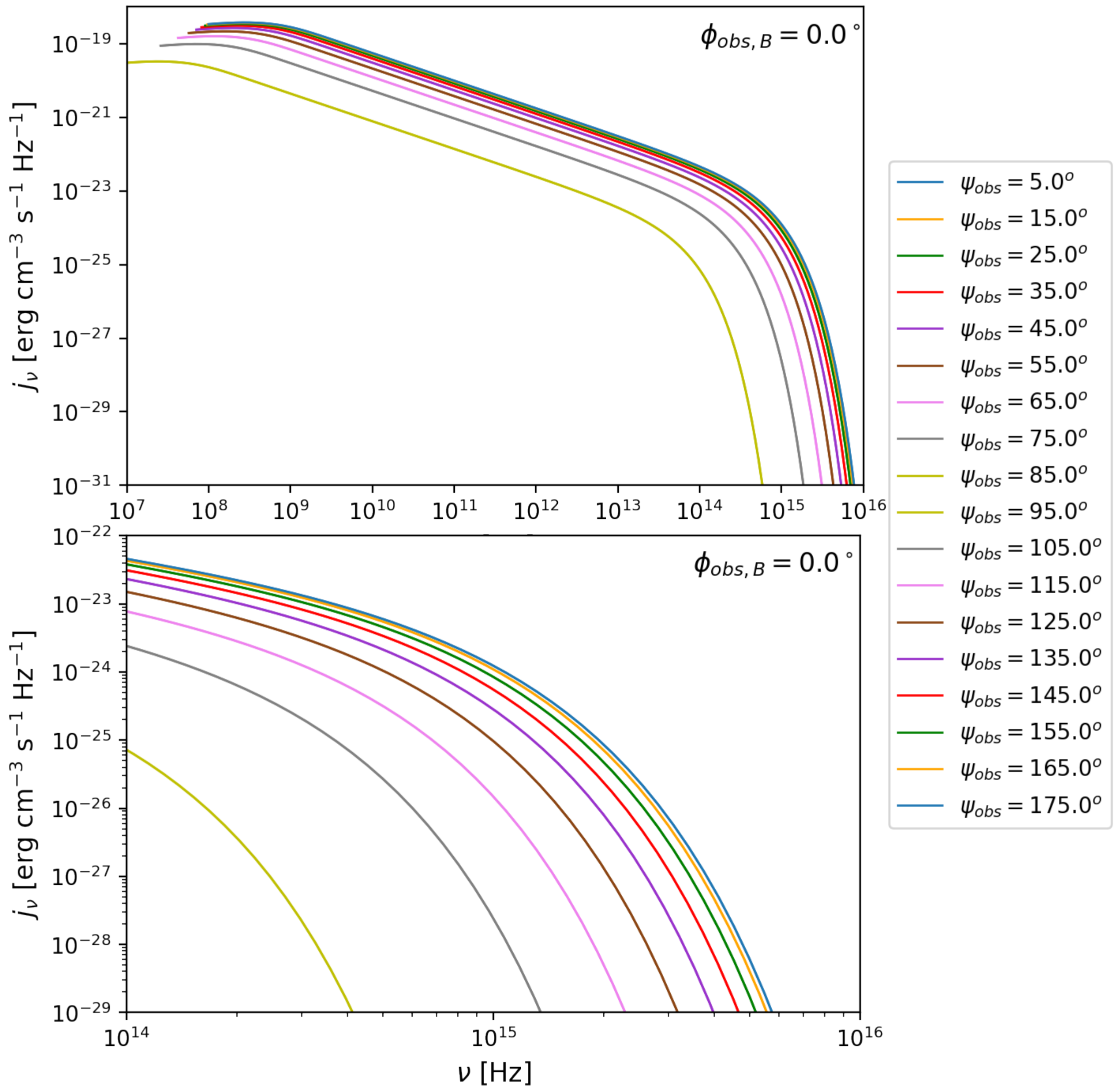

Figure 4.4: The non-zoomed (upper panel) and zoomed (lower panel) synchrotron emissivity under the effects of the perpendicular magnetic field w.r.t. the jet axis. Here, ψ_{obs} is running from 5° to 175° and $\phi_{obs} = \phi_B = 0°$.

Figure 4.5 shows the effects of varying angle ϕ_B with different viewing angles on the synchrotron emission while keeping the observer's azimuthal angle ϕ_{obs} fixed at 0°. For the $\psi_{obs} = 5°$ case, when $\phi_B = 90°$, the sine of the pitch angle is 1, and it remains close to 1 irrespective of the magnetic field azimuthal angle. As a result, the emission level remains almost the same. On the other hand, for larger viewing angles, the dependence of the sine of the pitch angle on the magnetic field azimuthal angle becomes considerably stronger. This results in noticeable variations in the synchrotron emission levels, as shown in the top-right plot and the lower plot. It is worth noting that these findings are symmetrical around the viewing angle of $\psi_{obs} = 90°$. Thus, we have omitted plots for the viewing angle ranging from 95°

to 175°. Finally, varying the observer's azimuthal angle while keeping the magnetic field azimuthal angle the same would produce similar results.

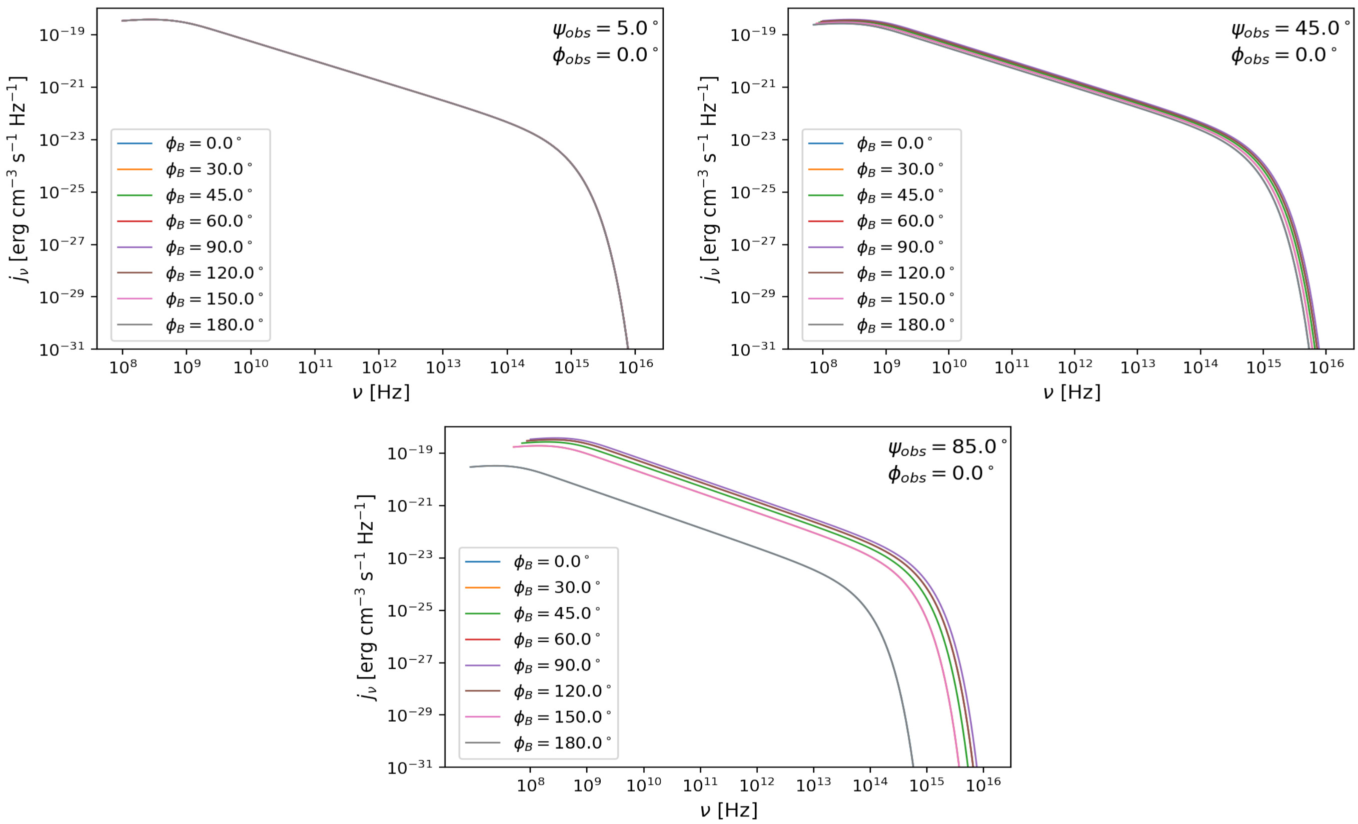

Figure 4.5: The effects of the perpendicular magnetic field's azimuthal angle ϕ_B on the synchrotron emissivity for different values of ψ_{obs} with ϕ_{obs} fixed to 0°.

4.3 Oblique Field

In this section, we discuss the effects of varying the values of angles ψ_B and ϕ_B on the synchrotron spectrum and the degree of linear polarization under the orientations of an oblique magnetic field relative to the jet axis. Meanwhile, we maintain the values of angles ψ_{obs} and ϕ_{obs} constant at 5° and 0°, respectively, except for Figure 4.6, where the viewing angle is varied.

Figures 4.6, 4.7, and 4.8 show the influence of this field geometry on the synchrotron emission and the synchrotron PD (bottom plot of Figure 4.6). In Figure 4.6, the angle ψ_B changes from 5° to 85° and from 95° to 175°, while keeping ϕ_B constant at 0° and varying the viewing angle as 5° (upper panels and lower plot), 45° (middle-left plot), and 65° (middle-right plot). In Figure 4.7, the value of ψ_B is varied from 5° up to 175°, while ϕ_B is kept the same at 0°. Finally, in Figure 4.8, ϕ_B is varied from 0° to 180° for different values of ψ_B.

The Figures show that a certain combination of angles ψ_B and ϕ_B can result in a case

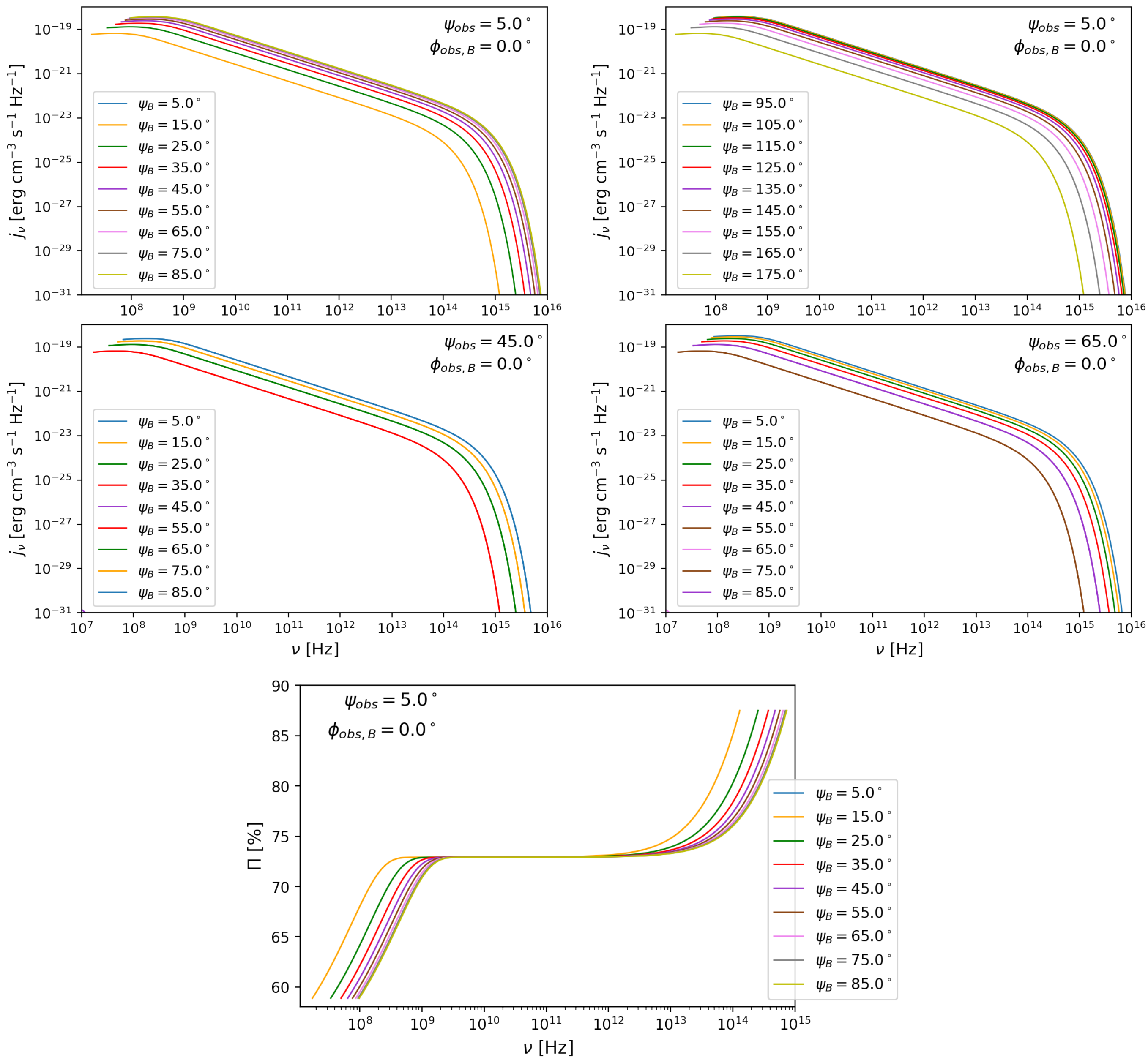

Figure 4.6: The impacts of oblique fields w.r.t. the jet axis on the synchrotron emissivity (upper panels) and degrees of polarization (lower panel) for values of ψ_{obs} ranging from 5° to 175° when $\phi_{obs} = \phi_B = 0°$.

where synchrotron emission is unobservable, depending on the orientations of oblique magnetic field lines w.r.t the jet axis. This is particularly evident when $\phi_B = 0°$ and the magnetic field is closely aligned with our LoS, e.g., when $\psi_B = \psi_{obs}$. When $\psi_B = \psi_{obs} = 5°$, as presented in the top-left plots of Figures 4.6 and 4.8, as well as in the top plot of Figure 4.7, and when $\psi_B = \psi_{obs} = 45°$ and 65° as demonstrated in the middle-left and -right plots of Figure 4.6, respectively, no synchrotron emission is observed. This situation is in agreement with the results of Joshi et al. (2020). In contrast to the scenarios of parallel and perpendicular magnetic fields, Figure

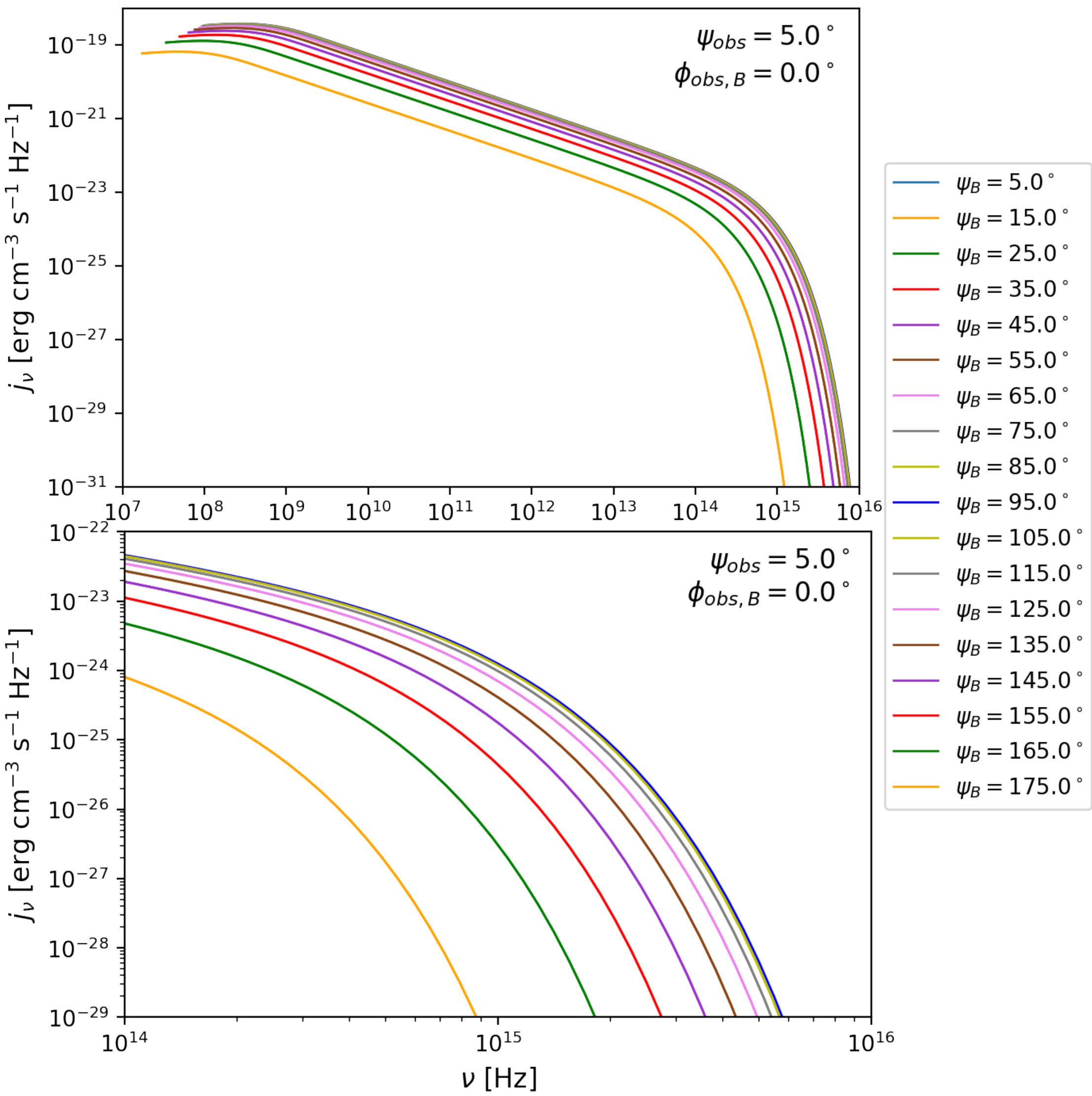

Figure 4.7: The non-zoomed (upper panel) and zoomed (lower panel) synchrotron emissivity under the effects of oblique fields w.r.t. the jet axis for ψ_{obs} ranging from 5° to 175° and $\phi_{obs} = \phi_B = 0°$.

4.7 demonstrates that only synchrotron emissivities for the field angle w.r.t. the jet axis varying from 15° to 85° (hereafter j_3^{syn}) are equivalent to those of ψ_B values changing from 175° down to 105° (hereafter j_4^{syn}), as indicated by the colors of the curves. Notice that this is an exception for the synchrotron emission at $\psi_B = 5°$ and at $\psi_B = 95°$ where the emission is absent and is at its maximum, respectively.

Furthermore, in Figure 4.6, we observe that certain synchrotron emission levels are indistinguishable from each other and hence, cannot show up individually, as demonstrated in the middle plots. At the viewing angle of $\psi_{obs} = 45°$, the emission levels are symmetrical. As the viewing angle approaches 90°, the sine of the pitch angle tends to have an inverse relationship with the angle that the magnetic field makes with the jet axis. This can clearly be seen in the middle-right plot for ψ_B

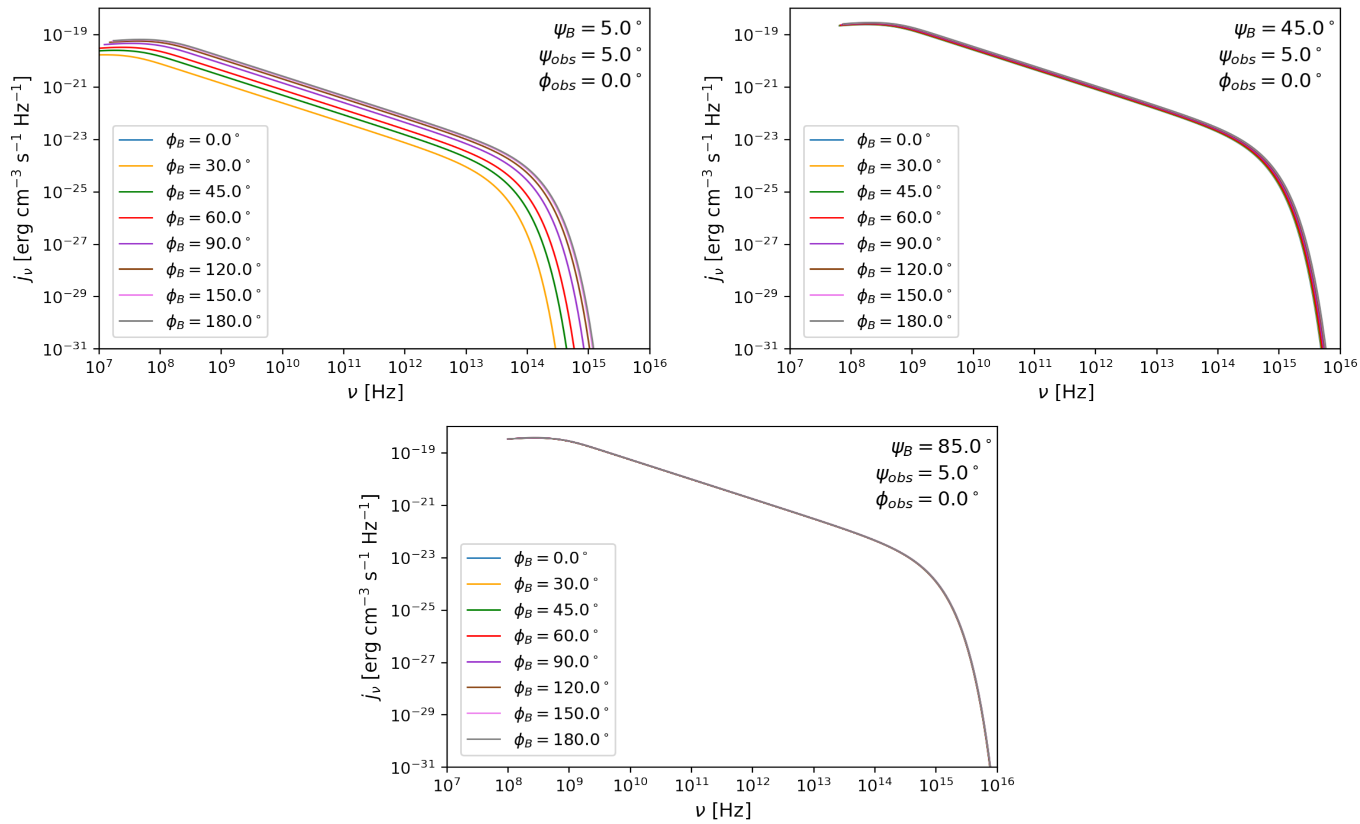

Figure 4.8: The effects of the angle ϕ_B for oblique fields w.r.t. the jet axis on the synchrotron emissivity for varying values of ψ_B with fixed ψ_{obs} and ϕ_{obs}.

values of 5°, 15°, and 25°, where the emission level decreases with an increasing ψ_B.

With regard to the polarization signatures shown in the bottom plot of Figure 4.6, there has been a significant leftward shift in the PD for a case where $\psi_{obs} = \psi_B = 5°$. This is in agreement with what is shown in the top-left plot, where the synchrotron emission level is significantly suppressed under the same case. Note that we have excluded signatures corresponding to the top-right plot since are similar to those of a perpendicular magnetic field case.

Similar to a case when the field orientation is perpendicular to the jet axis, e.g., Figure 4.5, Figure 4.8 shows the impacts of varying the magnetic field azimuthal angle as well. However, in this case, the impacts are demonstrated for different angles of the magnetic field w.r.t. the jet axis, while maintaining a viewing angle of $\psi_{obs} = 5°$. For a scenario of $\psi_B = 85°$, the sine of the pitch angle is almost independent of the azimuthal angle of the magnetic field. This results in a case where the synchrotron emission level remains nearly the same with the varying ϕ_B. However, for smaller values of ψ_B, the dependence of the synchrotron emission on the azimuthal angle of the magnetic field becomes more pronounced. These results are symmetric around an angle of $\psi_B = 90°$. Moreover, in addition to what is mentioned above, similar results will be obtained by varying the observer's angles ψ_{obs} and ϕ_{obs} while keeping the magnetic field angles ψ_B and ϕ_B the same.

4.4 Synchrotron and SSC Spectra

In this context, in addition to the above-studied impacts of varying the values of ψ_{obs}, ψ_B, and ϕ_B on the synchrotron emission, we explore the impacts of these very same angles on the total spectrum (combination of the synchrotron spectrum and the SSC spectrum) of our generic blazar and the degree of polarization of the SSC mechanism (high-energy PDs).

Figure 4.9 displays the SSC spectrum, the synchrotron spectrum, and the total spectrum under the influence of the parallel magnetic field w.r.t. the jet axis. The SSC spectrum is presented for different viewing angles ranging from 5° to 85° (see the LHS plot). As can be seen, the SSC spectrum remains nearly constant as the viewing angle varies. There are three main reasons for this according to Jamil and Boettcher (2012). These reasons are: 1) the anisotropies introduced by field orientation in the photon distribution are averaged out when scattered off an isotropic electron distribution, 2) the slight differences that do exist are due to a slight angle dependence through the presence of the $1 - \beta\mu$ factor in the calculations of the IC emissivity, and 3) the Compton scattered emissivity by an isotropic distribution of electrons is always approximately isotropic. The first reason is due to the fact that when synchrotron photons interact with the same population of relativistic electrons that produced them, their trajectories become randomized, causing photons initially oriented in a specific direction to scatter in various directions. This randomization mechanism leads to averaging out of the initial anisotropies in the photon distribution (Baring, 1990), resulting in isotropic SSC emission across different viewing angles.

The RHS plot shows both the synchrotron and the SSC spectra with their total spectrum for a viewing angle of $\psi_{obs} = 5°$. The Figure demonstrates that, as stated in Section 1.1.4.2, both the synchrotron and SSC spectra form the two broad, non-thermal humps that are associated with the low- and high-energy components of the SED of a generic blazar. The turnover from the first hump to the second hump takes place in the near-UV band at a frequency of about 4×10^{14} Hz. Moreover, the overall emission is Compton/SSC-dominated. In the following, our focus is on the total spectrum.

Figure 4.10 displays the impacts of varying the viewing angle on the SED of our generic blazar under the influence of the magnetic field lines parallel to the jet axis. In addition to what has been mentioned in Section 4.1, as the synchrotron emission

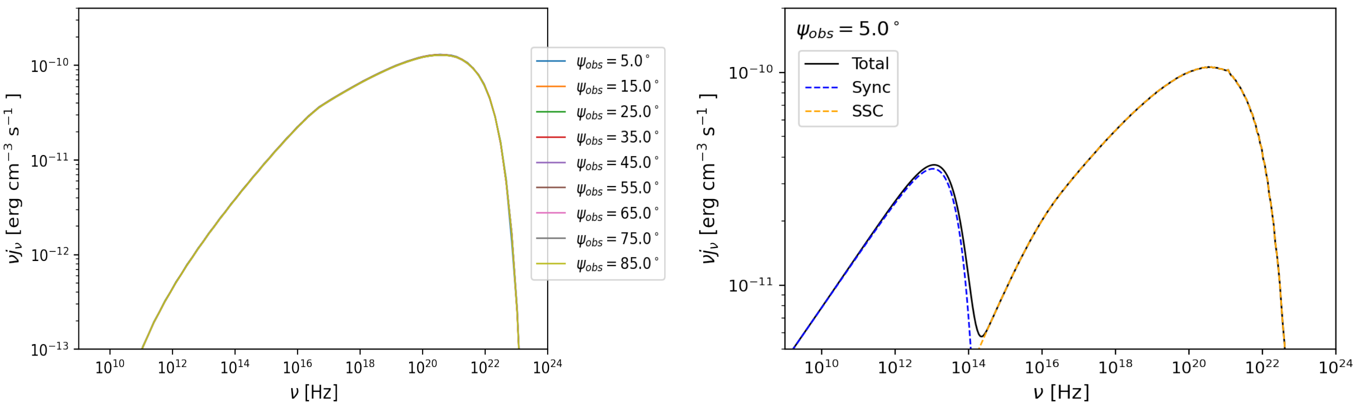

Figure 4.9: Demonstration of the SSC spectrum for various viewing angles of $\psi_{obs} \in [5^\circ, 85^\circ]$ (LHS plot) and the comparison of the synchrotron and SSC spectra and the total spectrum for $\psi_{obs} = 5^\circ$ (RHS plot). These spectra are shown for a parallel magnetic field.

component rises with increasing the observing angle, the corresponding synchrotron peak frequency shifts to higher values. As a result, this component converges at its maximum as the viewing angle approaches 90°. On the other hand, the SSC emission component maintains almost the same level as expected. Furthermore, the SED is Compton-dominated emission for the viewing angle of $\psi_{obs} = 5^\circ$. However, as the viewing angle ranges from 15° to 85°, the overall emission becomes increasingly synchrotron-dominated emission.

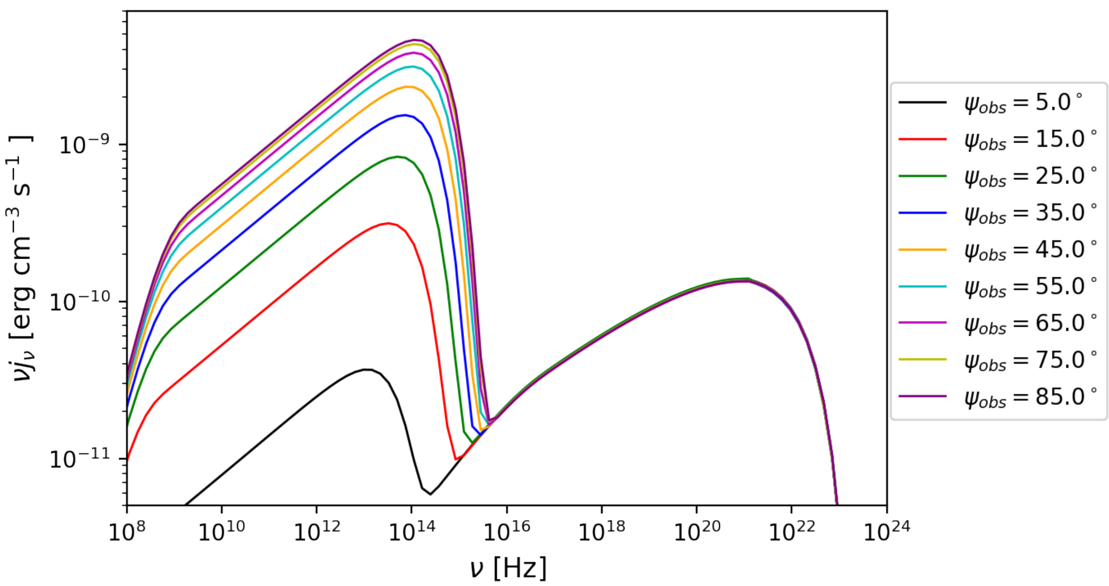

Figure 4.10: The influence of the viewing angle in the case of a parallel magnetic field on our total spectrum of a generic blazar.

In Figure 4.11, we display the impacts of the perpendicular magnetic field on our generic blazar SEDs. Here, we vary the viewing angle for different values of the

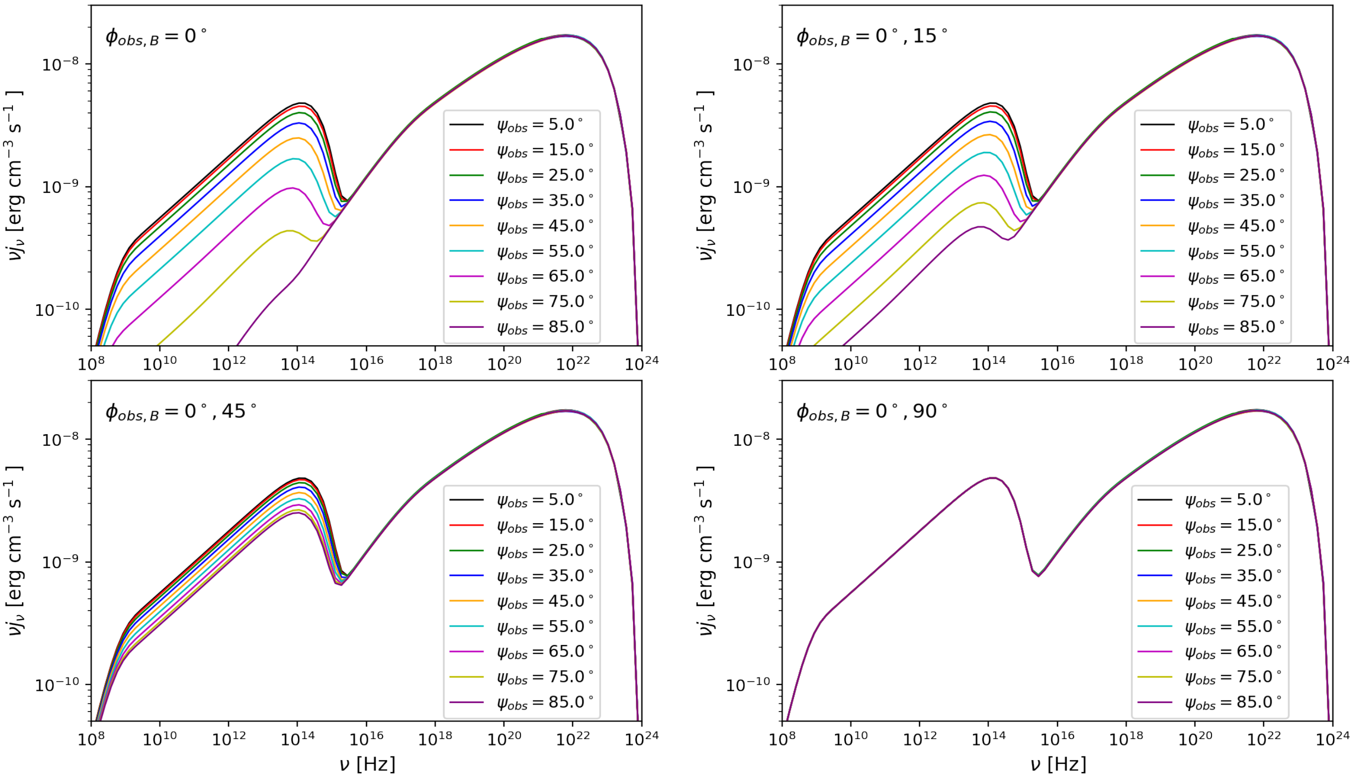

Figure 4.11: The influence of the perpendicular magnetic field orientation on the SEDs of a typical blazar.

magnetic field azimuthal angle. For a scenario of $\phi_B = 90°$ (bottom-right plot), the low-energy component shows no dependence on the viewing angle, whereas, as usual, the high-energy component is almost independent of the viewing angle. For smaller values of the field azimuthal angle, the dependence of the low-energy component on the viewing angle becomes more noticeable. As the viewing angle increases, the level of the low-energy component drops. As a result, the corresponding synchrotron peak frequency shifts to lower values. However, when the viewing angle approaches 90° for an azimuthal angle of $\phi_B = 0°$, the synchrotron emission becomes unobservable, while the SSC emission stays observed. In this magnetic field geometry case, the SED is SSC emission dominated, irrespective of the viewing angle and the field azimuthal angle.

Furthermore, Figure 4.12 shows the effects of varying the angle ψ_B on the SEDs of our typical blazar, while changing the magnetic field azimuthal angle and keeping the viewing angle fixed at 5°, for the case of an oblique magnetic field w.r.t. the jet axis. As the angle between the magnetic field and jet axis approaches 90°, the low-energy component converges at its maximum. The alignment of the magnetic-field relative to the jet axis with our LoS can lead to cases where the low-energy component is completely absent or substantially suppressed. For input parameters considered in our study, such cases arise for an angle of $\psi_B = 5°$ when the field azimuthal angle

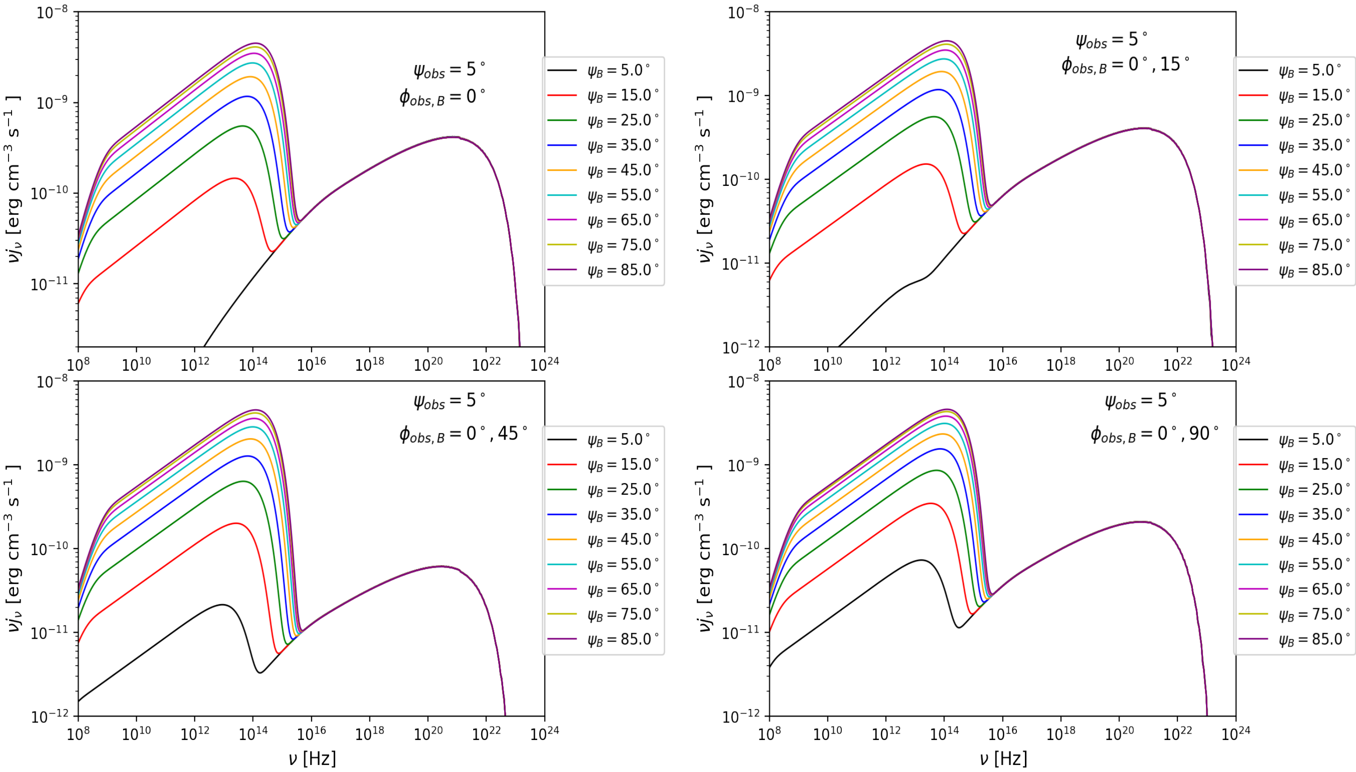

Figure 4.12: The influence of the oblique magnetic field geometry on the SEDs of our typical blazar.

is equal to 0° and 15°, as presented in the top-left and -right plots, respectively. However, despite the SED first hump being absent, the electrons continue to receive that emission and up-scatter a fraction of it to produce the high-energy component. Thus, in this direction, the high-energy component is observable, whereas the low-energy component is not. For higher values of ϕ_B, for the same ψ_B value, the low-energy component becomes more noticeable. As a result, the spread of levels of the low-energy component decreases as the dependence of the synchrotron emission on the value of ψ_B becomes significantly stronger.

Moreover, in Figure 4.12, the behavior of the peak flux of the high-energy component appears to show some irregularities that are not immediately noticeable. Initially, in the upper plots, the peak flux of the SSC component remains constant as the angle ϕ_B increases. On the other hand, in the lower-left plot, when $\phi_B = 45°$, the peak SSC flux experiences a significant drop by a factor of about $6-7$. In the lower-right plot, when $\phi_B = 90°$, the peak flux of the SSC emission rises again, but does not fully recover to the original level for $\phi_B = 0°$. Furthermore, as ψ_B varies from 15° to 85° in the lower plots and from 25° to 85° in the upper ones, the overall emission becomes more and more dominated by the synchrotron emission.

Figure 4.13 shows the PD of the SSC emission in the case of a parallel magnetic field orientation w.r.t. the jet axis. The Figure demonstrates that, similar to the SED high-energy component, the high-energy PD is almost not affected as the viewing angle and the orientation of the magnetic field relative to the jet axis varies. The polarization signatures in cases of both the perpendicular and oblique magnetic field geometries are omitted since they are indistinguishable from those observed in the parallel magnetic field case.

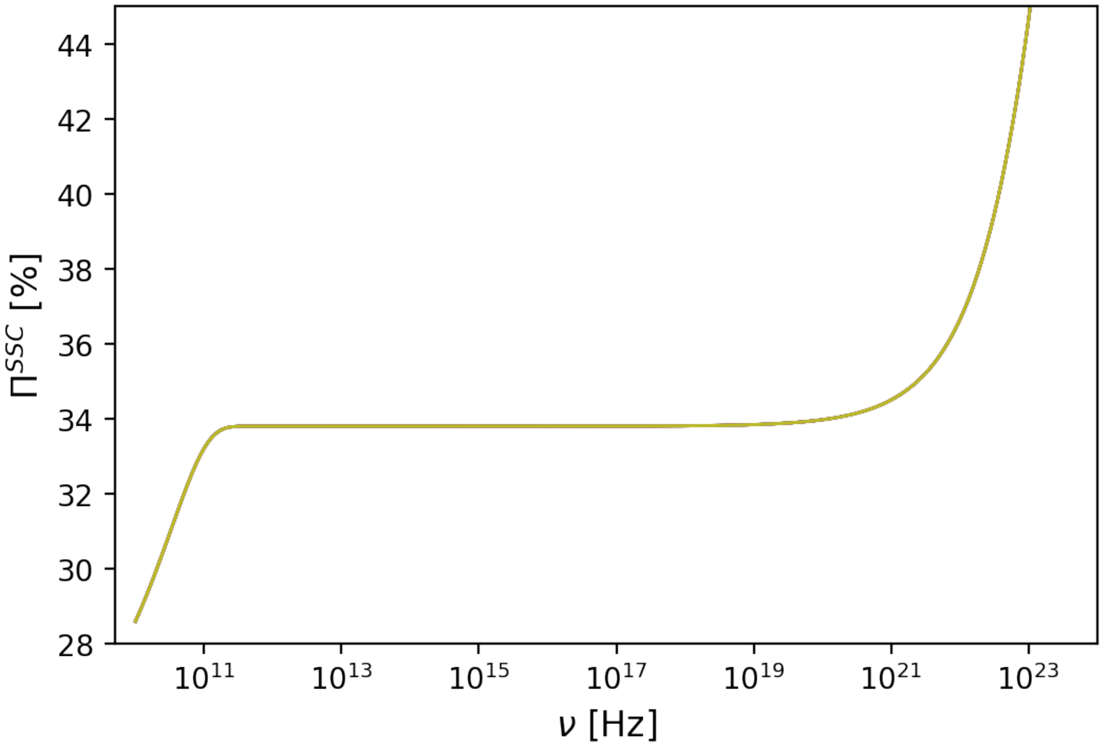

Figure 4.13: The effects of the parallel magnetic field w.r.t. the jet axis on the SSC degrees of polarization.

4.5 Variation of Power-Law Index

In this section, we present the impacts of varying the electron power-law index p on the synchrotron emission coefficient, polarization of synchrotron emission, and the total spectrum of a typical blazar. These impacts are studied only in the case of the magnetic field closely aligned with the jet-axis, while keeping the viewing angle constant at 5°. This is because the effects of changing the power-law index on the synchrotron and the SSC emissions are not altered by both the magnetic field orientation and the viewing angle.

Figure 4.14 demonstrates the emissivity (left plot) and PD (right plot) of the synchrotron emission. As implied by Equation 2.13, the steepness of the synchrotron emissivity is guided by the electron power-law index. As the value of p increases, the steeper the synchrotron spectrum becomes. The corresponding low-energy and

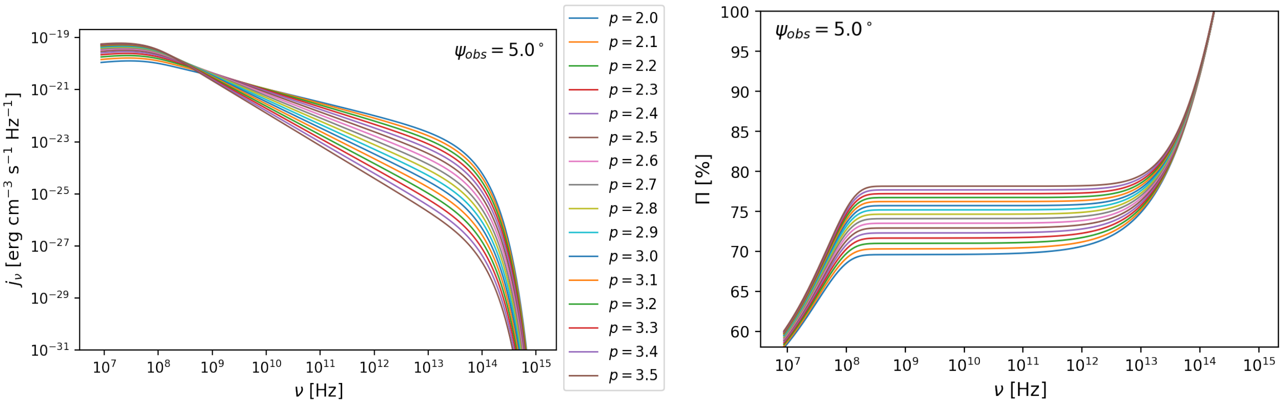

Figure 4.14: The effects of the power-law index on the synchrotron emissivity (left plot) and the synchrotron polarization (right plot) under the influence of the parallel field geometry.

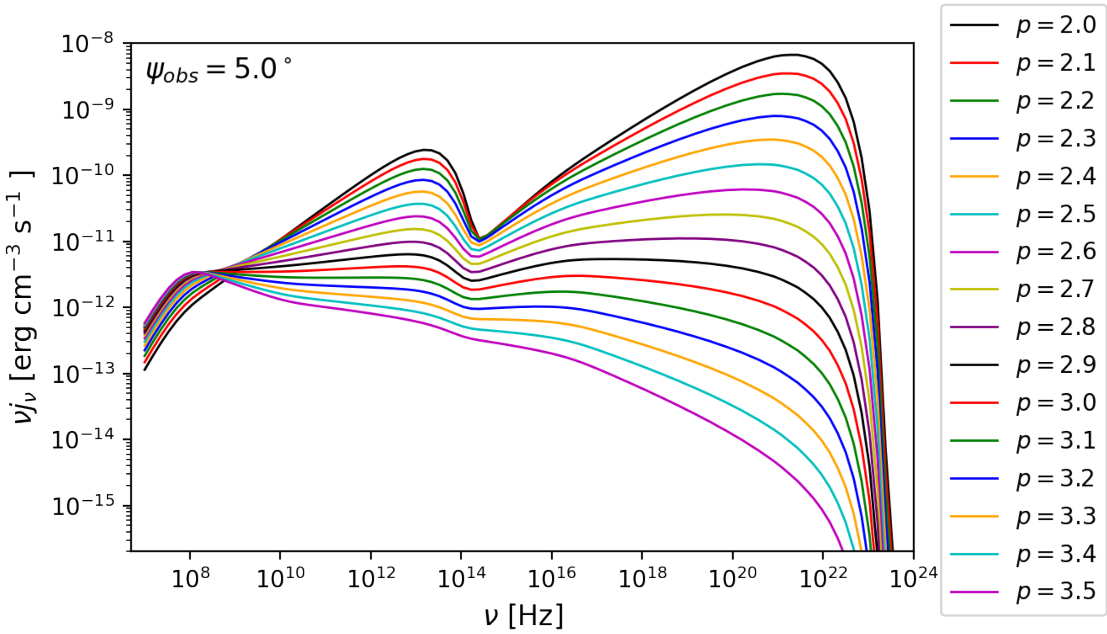

Figure 4.15: The effect of varying the power-law index on the SED of our generic blazar under the influence of the parallel field orientation.

high-energy cutoff frequencies remain the same as the power-law index varies. This is in evidence by Equation 2.16. Regarding synchrotron polarization, in contrast to the variations of the viewing angle and the magnetic field orientation, changing the power-law index alters the degree of polarization. As the power-law index increases, the linear degree of polarization rises as well. The polarization signatures corresponding to the SSC mechanism are omitted, as they show similar effects to those observed in the synchrotron polarization.

In Figure 4.15, we show the variation of the SED of our typical blazar as the electron power-law index changes. The varying power-law index has dramatic impacts on the morphology of the SED. For lower values of the power-law index, the two broad, non-thermal humps of the SED are significantly noticeable. As a result, the produced emission is Compton-dominated. On the other hand, for larger power-law index values, the doubled-hump SED becomes invisible and the entire SED is dominated by synchrotron emission. This scenario can clearly be observed for the power-law index of $p = 3.5$, where the SED declines from $\sim 1.5 \times 10^8$ Hz to higher frequencies and no longer consists of two clearly distinguishable components. However, despite the SSC component disappearing with increasing $p-$values, the location of the corresponding synchrotron peak frequency remains the same.

Chapter 5

Summary and Outlook

In this work, we have conducted a comprehensive study by investigating different parameters that may influence the multiwavelength emission of a generic blazar. Particularly, we explored the effects of the viewing angle, orientation of the magnetic field (such as parallel, perpendicular, and oblique geometries) w.r.t. the jet axis, and the electron power-law index. Our objective was to examine how these parameters affect a generic blazar's observational properties, such as SEDs and PDs. The effect can be identified in terms of the variation in the emission level, the location of the synchrotron cutoff and peak frequencies, the dominant emission mechanism, and the level or potential horizontal shift of the PD.

In order to accomplish our goal, we have made use of a single-zone synchrotron and SSC blazar model, including two basic assumptions: 1) the power-law distribution of isotropic, relativistic electrons (Equation 2.1) and 2) a perfectly ordered, uniform magnetic field of strength B with arbitrary orientation w.r.t. the jet axis in a spherical emitting region. The new aspect was to treat the anisotropy of the radiation produced and the polarization in the treatment of both the synchrotron and SSC mechanisms.

We have demonstrated that, as expected, the synchrotron emission has a significant dependence on the viewing angle and the magnetic field orientation w.r.t. the jet axis. The synchrotron emission level and the corresponding minimum and maximum cutoff frequencies are strongly affected by the variation of the viewing angle and the orientation of the magnetic field. As Joshi et al. (2020) demonstrated, we have observed that, particularly in the case of an oblique magnetic field, the synchrotron emission level will remain substantially suppressed as long as the observer's angles ψ_{obs} and ϕ_{obs} are equal to the field angles ψ_B and ϕ_B, respectively. Moreover, it is shown that the effects on the synchrotron emission are symmetric around the viewing angle that corresponds to 0° or 90° w.r.t. the orientation of the magnetic field.

The IC emissivity is calculated using the angle-dependent synchrotron radiation as a seed photon field. For the above-stated reasons in Section 4.4, as expected, the SED high-energy component is almost unaffected by the variation of the viewing angle and the magnetic field angle w.r.t. the jet axis. However, it showed some dependence on the magnetic field azimuthal angle ϕ_B in the case of an oblique magnetic field geometry. This behavior is demonstrated in Figure 4.12, where the high-energy component peaks at higher flux levels for smaller values of ϕ_B compared to that for larger ϕ_B-values.

For considered input parameters in our study, the SED of a generic blazar showed to be dominated by the SSC emission in the case of a perpendicular magnetic field geometry, irrespective of the viewing angle and the field azimuthal angle. In the parallel magnetic field case, a blazar's emission is SSC-dominated when the viewing angle is $5°$ and becomes increasingly dominated by the synchrotron radiation as the viewing angle varies from $15°$ to $85°$. The exact similar results were obtained in the scenario of an oblique magnetic field, as shown in lower plots of Figure 4.12. However, the SED is increasingly synchrotron-dominated as the viewing angle ranges from $25°$ to $85°$, as shown in the upper plots.

The impact of the electron power-law index p on a generic blazar was also explored. The variation of the power-law index had a significant impact on the SEDs and PDs of our generic blazar. As the power-law index increases, the SED components become no longer distinguishable, whereas the average PD rises. On the other hand, in the frequency range in which the synchrotron spectrum is well represented by a power-law, both the viewing angle and the magnetic field orientation had no effect on the value of the average PD. However, the synchrotron polarization was shifting horizontally with the variation of these parameters, but without changing the average PD value.

This study was the first step in the development of a comprehensive, fully angle- and polarization-dependent blazar radiation transfer code. For future analysis, in addition to synchrotron and SSC emissions, we will also include the effects of synchrotron self-absorption and gamma-ray absorption mechanisms.

Bibliography

Abramowicz, M. A. and Straub, O. (2014). Accretion discs. *Scholarpedia*, 9(8):2408. revision #145813.

Alexander, E. L. (2022). File:Emmaalexander synchrotron.png. http://en.m.wikipedia.org/wiki/File:Emmaalexander_synchrotron.png. Accessed: 2023-02-08.

Angelakis, E., Hovatta, T., Blinov, D., Pavlidou, V., Kiehlmann, S., Myserlis, I., Böttcher, M., Mao, P., Panopoulou, G., Liodakis, I., et al. (2016). Robopol: the optical polarization of gamma-ray-loud and gamma-ray-quiet blazars. *Monthly Notices of the Royal Astronomical Society*, 463(3):3365–3380.

Azadi, M. (2017). *Multi-wavelength Analysis of Active Galactic Nuclei and Host Galaxies Physical Properties*. PhD thesis, UC San Diego.

Baring, M. G. (1990). The influence of the distribution of photon and electron angles on synchrotron models of gamma-ray burst spectra. *Monthly Notices of the Royal Astronomical Society*, 244:49–57.

Blandford, R., Meier, D., and Readhead, A. (2019). Relativistic jets from active galactic nuclei. *Annual Review of Astronomy and Astrophysics*, 57:467–509.

Blinov, D., Pavlidou, V., Papadakis, I., Hovatta, T., Pearson, T., Liodakis, I., Panopoulou, G., Angelakis, E., Baloković, M., Das, H., et al. (2016a). Robopol: optical polarization-plane rotations and flaring activity in blazars. *Monthly Notices of the Royal Astronomical Society*, 457(2):2252–2262.

Blinov, D., Pavlidou, V., Papadakis, I., Kiehlmann, S., Liodakis, I., Panopoulou, G., Angelakis, E., Baloković, M., Hovatta, T., King, O., et al. (2018). Robopol: Connection between optical polarization plane rotations and gamma-ray flares in blazars. *Monthly Notices of the Royal Astronomical Society*, 474(1):1296–1306.

Blinov, D., Pavlidou, V., Papadakis, I., Kiehlmann, S., Liodakis, I., Panopoulou, G., Pearson, T., Angelakis, E., Baloković, M., Hovatta, T., et al. (2016b). Robopol: do optical polarization rotations occur in all blazars? *Monthly Notices of the Royal Astronomical Society*, 462(2):1775–1785.

Boettcher, M. (2012). Modeling the spectral energy distributions and variability of blazars. *arXiv preprint arXiv:1205.0539*.

Bonometto, S. and Saggion, A. (1973). Polarization in inverse compton scattering of synchrotron radiation. *Astronomy and Astrophysics, Vol. 23, p. 9 (1973)*, 23:9.

Böttcher, M. (2007). Modeling the emission processes in blazars. In *The Multi-Messenger Approach to High-Energy Gamma-Ray Sources*, pages 95–104. Springer.

Böttcher, M. (2019). Progress in multi-wavelength and multi-messenger observations of blazars and theoretical challenges. *Galaxies*, 7(1):20.

Böttcher, M., Harris, D. E., and Krawczynski, H. (2012). *Relativistic jets from active galactic nuclei*. John Wiley and Sons.

Böttcher, M., Reimer, A., Sweeney, K., and Prakash, A. (2013a). Leptonic and hadronic modeling of fermi-detected blazars. *The Astrophysical Journal*, 768(1):54.

Böttcher, M., Reimer, A., and Zhang, H. (2013b). Leptonic and hadronic modeling of fermi-detected blazars-spectral energy distribution modeling and high-energy polarization predictions. In *EPJ Web of Conferences*, volume 61, page 05003. EDP Sciences.

Bruss, J. (2012). Introduction to Astronomy Unit 4: Active Galaxies Part 2. http://youtube.com/watch?v=dCJEvfVGcds. Accessed: 2023-01-23.

Dermer, C. D. and Menon, G. (2009). *High energy radiation from black holes: gamma rays, cosmic rays, and neutrinos*, volume 17. Princeton University Press.

Fitzpatrick, R. (2013). Polarization of Electromagnetic Waves. http://farside.ph.utexas.edu/teaching/315/Waveshtml/node50.html. Accessed: 2023-02-09.

Fossati, G. a., Maraschi, L., Celotti, A., Comastri, A., and Ghisellini, G. (1998). A unifying view of the spectral energy distributions of blazars. *Monthly Notices of the Royal Astronomical Society*, 299(2):433–448.

Frank, J. (2016). Accretion Disk. Encyclopedia Britannica. https://www.britannica.com/science/accretion-disk. Accessed: 2022-09-15.

Ghisellini, G. (2013). *Radiative processes in high energy astrophysics*, volume 873. Springer.

Griffiths, D. J. (2021). Introduction to electrodynamics fourth edition.

Hartle, J. B. (2003). Gravity: An introduction to Einstein's general relativity.

Jackson, J. D. (2021). *Classical electrodynamics*. John Wiley & Sons.

Jamil, O. and Boettcher, M. (2012). An angle dependent ssc model for relativistic jet sources. *arXiv preprint arXiv:1209.2711*.

Joshi, M., Marscher, A., and Böttcher, M. (2016). Theoretical study of the effects of magnetic field geometry on the high-energy emission of blazars. *Galaxies*, 4(4):45.

Joshi, M., Marscher, A. P., and Boettcher, M. (2014). Seed photon fields of blazars in the internal shock scenario. *The Astrophysical Journal*, 785(2):132.

Joshi, M., Marscher, A. P., and Böttcher, M. (2020). Impact of ordered and disordered magnetic fields on multiwavelength emission of blazars. *The Astrophysical Journal*, 898(1):11.

Konigl, A. and Choudhuri, A. R. (1985). A model of the polarization position-angle swings in bl lacertae objects. *The Astrophysical Journal*, 289:188–192.

Krawczynski, H. (2011). The polarization properties of inverse compton emission and implications for blazar observations with the gems x-ray polarimeter. *The Astrophysical Journal*, 744(1):30.

Liodakis, I., Marscher, A. P., Agudo, I., Berdyugin, A. V., Bernardos, M. I., Bonnoli, G., Borman, G. A., Casadio, C., Casanova, V., Cavazzuti, E., et al. (2022). Polarized blazar x-rays imply particle acceleration in shocks. *Nature*, 611(7937):677–681.

Longair, M. S. (2010). *High energy astrophysics*. Cambridge university press.

Marscher, A. P., Jorstad, S. G., D'Arcangelo, F. D., Smith, P. S., Williams, G. G., Larionov, V. M., Oh, H., Olmstead, A. R., Aller, M. F., Aller, H. D., et al. (2008). The inner jet of an active galactic nucleus as revealed by a radio-to-γ-ray outburst. *Nature*, 452(7190):966–969.

Marscher, A. P., Jorstad, S. G., Larionov, V. M., Aller, M. F., Aller, H. D., Lähteenmäki, A., Agudo, I., Smith, P. S., Gurwell, M., Hagen-Thorn, V. A., et al. (2010). Probing the inner jet of the quasar PKS 1510$-$089 with multi-waveband monitoring during strong gamma-ray activity. *The Astrophysical Journal Letters*, 710(2):L126.

Nave, R. (2017). Classification of Polarization. http://hyperphysics.phy-astr.gsu.edu/hbase/phyopt/polclas.html. Accessed: 2022-12-07.

Netzer, H. (2015). Revisiting the unified model of active galactic nuclei. *arXiv preprint arXiv:1505.00811*.

Padmanabhan, T. (2002). *Theoretical astrophysics: volume 3, galaxies and cosmology*. Cambridge University Press.

Padovani, P. (2016). The faint radio sky: radio astronomy becomes mainstream. *The Astronomy and Astrophysics Review*, 24(1):1–61.

Padovani, P. (2017). On the two main classes of active galactic nuclei. *Nature Astronomy*, 1(8):1–2.

Padovani, P., Miller, N., Kellermann, K., Mainieri, V., Rosati, P., and Tozzi, P. (2011). The vla survey of chandra deep field south. v. evolution and luminosity functions of sub-millijansky radio sources and the issue of radio emission in radio-quiet active galactic nuclei. *The Astrophysical Journal*, 740(1):20.

Quirrenbach, A., Witzel, A., Qian, S., Krichbaum, T., Hummel, C., and Alberdi, A. (1989). Rapid radio polarization variability in the quasar 0917+ 624. *Astronomy and Astrophysics*, 226:L1–L4.

Reynolds, C., Ueda, Y., Awaki, H., Gallo, L., Gandhi, P., Haba, Y., Kawamuro, T., LaMassa, S., Lohfink, A., Ricci, C., et al. (2014). Astro-h white paper-agn reflection. *arXiv preprint arXiv:1412.1177*.

Rybicki, G. B. and Lightman, A. P. (1991). *Radiative processes in astrophysics*. John Wiley & Sons.

Schmidt, M. (1970). Space distribution and luminosity functions of quasars. *The Astrophysical Journal*, 162:371.

Schneider, P. (2006). *Extragalactic astronomy and cosmology: an introduction*, volume 146. Springer.

Tinbergen, J. (2005). Astronomical polarimetry. *Astronomical Polarimetry*.

Trippe, S. (2014). Polarization and polarimetry: a review. *arXiv preprint arXiv:1401.1911*.

Urry, C. M. and Padovani, P. (1995). Unified schemes for radio-loud active galactic nuclei. *Publications of the Astronomical Society of the Pacific*, 107(715):803.

Zhang, H. (2019). Blazar optical polarimetry: Current progress in observations and theories. *Galaxies*, 7(4):85.

Zhang, H. and Boettcher, M. (2013). X-ray and gamma-ray polarization in leptonic and hadronic jet models of blazars. *The Astrophysical Journal*, 774(1):18.

Zhang, H., Chen, X., Böttcher, M., Guo, F., and Li, H. (2015). Polarization swings reveal magnetic energy dissipation in blazars. *The Astrophysical Journal*, 804(1):58.

Appendix A

Our Code

Our developed Python code of full angle- and polarization-dependent blazar radiation transfer is presented here. Note that, the code is demonstrated only under the influence of the parallel magnetic field w.r.t. the jet axis in Gaussian units. We start with importing useful Python packages for our code, the definition of constants, and the calculation of the power-law electron distribution normalization factor, denoted as n_0, in units cm^{-3}:

```
# useful packages for our code
import numpy as np
from numpy import *
import matplotlib.pyplot as plt
from math import degrees, pi, sqrt
from mpmath import besselk

# constants
B = 1.0                 # magnetic field strength
gamma1 = 10             # low-energy cutoff
gamma2 = 1e4            # high-energy cutoff
p = 2.5                 # standard power-law index
L_e = 1e44              # kinetic power in the relativistic electrons
R = 1e16                # blob radius
Gamma = 15              # bulk Lorentz factor
c = 3e10                # the speed of light
m_e = 9.1094e-28        # electron mass
r_e = 2.8179e-13        # classical electron radius
beta_G = sqrt(1 - 1/Gamma**2) # normalized speed of the emission region
h = 6.6261e-27          # Planck's constant
t_esc = (3*R)/(4*c) # the average photon escape time for a sphere

fp = (gamma2**(2-p)-gamma1**(2-p))/(2-p) # calculation of Eq. 3.10
N0 = L_e /(pi*R**2*Gamma**2*m_e*c**3*beta_G*fp) # power-law
```

```
                                                    normalization factor
```

Subsequently, we calculate the synchrotron photon spectrum as:

```
# defining synchrotron photon spectrum
def jnuApprox(nu_sy,gamma1,gamma2,B,p,eta,N0):
    sinPsi = sqrt(1 - eta**2)

    gamma, delta1, d, sum2 = gamma1, 1.0, 1.5, 0.0
    # integrating over the electron energy
    while gamma < gamma2:
        gamma_mid = gamma * ((d + 1)/2)

        nu_psi = 4.2e6*B*(gamma_mid**2) * (sinPsi)
        x = (nu_sy/nu_psi)
        Fapprox = 1.42* sqrt(pi/2) *exp(-x) * x**(3/10)
        delta2 = gamma_mid**(-p) * Fapprox * (gamma*(d-1))
        sum2 += delta2
        gamma *= d
    sum2 *= ((2.34e-22)*B*(sinPsi)*N0)*(t_esc/(h*nu_sy))
    return sum2

# considered synchrotron photon directions
psiPh_para = array([pi/36,pi/12,pi/7.2,7*pi/36,pi/4,11*pi/36,
            13*pi/36,5*pi/12,17*pi/36,19*pi/36,7*pi/12,23*pi/36,
            25*pi/36,3*pi/4,29*pi/36,31*pi/36,11*pi/12,35*pi/36])

length = len(psiPh_para)
eta_para = zeros(length)
psiDegree_para = zeros(length)
for i in range(length):
    eta_para[i] = cos(psiPh_para[i])
    # determining angle psiPh_para in degrees
    psiDegree_para[i] = round(degrees(psiPh_para[i]),)

#------------------------------------------------------------------
# nu_min, nu_max, and N are the initial and final frequencies and
                                  number of points, respectively.
nu_min, nu_max, N = zeros(length), zeros(length), zeros(length)
#------------------------------------------------------------------
# calculating the frequency for photon directions
for i in range(length):
    nu_min[i] = (1e6*(gamma1**2)*B) * sqrt(1 - eta_para[i]**2)
    nu_max[i] = (1e8*(gamma2**2)*B) * sqrt(1 - eta_para[i]**2)
    dnu = 1.5 # increment multiplication
    N[i] = log(nu_max[i]/nu_min[i]) / log(dnu) + 2

    nuSy_para = zeros(int(N[i]))
    nuSy_para[0] = nu_min[i]
```

```
    j = 0
    while nuSy_para[j] < nu_max[i]:
        j += 1
        nuSy_para[j] = nuSy_para[j-1] * dnu
#------------------------------------------------------------------
# calculating angle- and frequency-dependent synchrotron photon spectrum
nPh2_para = zeros((length, len(nuSy_para)))
for i in range(length):
    for j in range(len(nuSy_para)):
        nPh2_para[i,j] = jnuApprox(nuSy_para[j], gamma1, gamma2, B, p, eta_para[i],N0)

# saving our calculations of the photon spectrum
np.save("nPh2_para.npy", nPh2_para)
```

Note that, in the above and following codes, the underscore "para" simply represents the parallel magnetic field orientation. Next, is the calculations of the SEDs of our generic blazar for different viewing angles when the magnetic field is parallel to the jet axis.

```
# note that, eta_s = cos(psi_s) and psi_s is the viewing angle
# synchrotron emissivity
def jnuApprox(nu_syn,gamma1,gamma2,B,p,eta_s,N0):
    sinPsi = sqrt(1 - eta_s**2)

    gamma, delta1, d, sum2 = gamma1, 1.0, 1.1, 0.0
    # integrating over the electron energy
    while gamma < gamma2:
        gamma_mid = gamma * ((d + 1)/2)

        nu_psi = 4.2e6*B*(gamma_mid**2) * (sinPsi)
        x = (nu_syn/nu_psi)
        Fapprox = 1.42* sqrt(pi/2) *exp(-x) * x**(3/10)
        delta2 = gamma_mid**(-p) * Fapprox * (gamma*(d-1))
        sum2 += delta2
        gamma *= d
    sum2 *= ((2.34e-22)*B*(sinPsi)*N0)
    return sum2
#------------------------------------------------------------------
#------------------------------------------------------------------
# loading synchrotron photon spectrum calculations
nPh2D_para = np.load("nPh2_para.npy")
# calculating the SSC emissivity for all considered
# synchrotron photon directions
def jcomp(Nu_c, eta_s):

    e_s = (h*Nu_c)/(m_e*c**2)
```

```
    # ensuring that the photon energy is always less than or
    # equal to the electron energy
    if e_s < gamma1:
        gamma = gamma1
    else:
        gamma = e_s

    Gamma, d_gam, delta6, sum6 = gamma, 1.5, 1.0, 0.0
    # integrating over the electron energy
    while Gamma < gamma2:
        Gamma_mid = Gamma*((d_gam+1)/2)

        d_eta, delta5, sum5, etA = 0.2, 1.0, 0.0, eta1
        # integrating over all synchrotron photon angles
        while etA < eta2:
            eta_mid = etA + d_eta/2

            d_phi, delta4, sum4, phi = 0.2, 1.0, 0.0, phi1
            # integrating over the photon's azimuthal angles
            while phi < phi2:
                phi_mid = phi + (d_phi)/2


                mu = (eta_mid*eta_s + sqrt(1-eta_mid**2)
                        * sqrt(1-eta_s**2)*cos(phi_mid))
                beta = sqrt(1 - 1/Gamma_mid**2)

                ErgFac = (m_e*c**2)/h
                nu1 = (e_s/(2*Gamma_mid*(Gamma_mid - e_s)
                        * (1 - beta*mu)))*ErgFac
                nu2 = ((2*e_s)/(1 - beta*mu)) * ErgFac

                d_eps, delta3, sum3, Nu = 1.5, 1.0, 0.0, nu1
                # integrating over synchrotron photon energy
                while Nu*(d_eps + 1)/2 < nu2:
                    nu_mid = Nu*((d_eps + 1)/2)

                    y = 1 - e_s/(Gamma_mid)
                    e_prime = Gamma_mid * (nu_mid*(1/ErgFac)) * (1
                                                      - beta*mu)
                    Y = y + 1/y - (2*e_s)/(Gamma_mid*e_prime*y)
                        + (e_s/(Gamma_mid*e_prime*y))**2
                    Z = (pi*r_e**2)/(Gamma_mid*e_prime)

                    for i in range(len(eta_para)):
                        if eta_para[i] > eta1:
                            break
                    for j in range(len(nuSy_para)):
                        if nuSy_para[j] > nu1:
```

```
                            break

                        delta3 = (1-beta*mu) * Z * Y
                                * nPh2D_para[i][j] * (Nu*(d_eps - 1))

                        sum3 += delta3
                        Nu *= d_eps
                    delta4 = sum3 * d_phi
                    sum4 += delta4
                    phi += d_phi
                delta5 = sum4 * d_eta
                sum5 += delta5
                etA += d_eta
            delta6 = (Gamma_mid**(-p)) * (sum5) * (Gamma*(d_gam - 1))
            sum6 += delta6
            Gamma *= d_gam
        sum6 *= N0 * ((h*c*e_s)/(4*pi))
        return sum6

eta1, eta2, phi1, phi2, m_e = -1, 1, 0.0001, 2*pi, 9.1094e-28
eta_s = 0.9961947  # = roughly 5 degrees
#-------------------------------------------------------------------
psi_s = array([pi/36,pi/12,pi/7.2,7*pi/36,pi/4,11*pi/36,13*pi/36,5*pi/12,17*pi/36])

length = len(psi_s)
eta_s = zeros(length)
psiDegrees = zeros(length)
for i in range(length):
    eta_s[i] = cos(psi_s[i])
    psiDegrees[i] = round(degrees(psi_s[i]),)
#-------------------------------------------------------------------

nu_min, nu_max = (1e5*(gamma1**2)*B), (5e8*(gamma2**4)*B)
dnu = 1.5
N = log(nu_max/nu_min) / log(dnu) + 2

nu_c2 = zeros(int(N))
# J_syn2, J_ssc2, and Total2 are synchrotron, SSC, and total spectra, respectively
J_syn2, J_ssc2, Total2 = zeros(int(N)), zeros(int(N)), zeros(int(N))
nu_c2[0] = nu_min

for j in range(length):
    i = 0
    while nu_c2[i] < nu_max:
        J_syn2[i] = nu_c2[i] * jnuApprox(nu_c2[i],gamma1,gamma2,B,p,eta_s[j],N0)
```

```
        J_ssc2[i] = nu_c2[i] * jcomp(nu_c2[i], eta_s[j])
        Total2[i] = J_syn2[i] + J_ssc2[i]
        i += 1
        nu_c2[i] = nu_c2[i-1] * dnu
    # ploting our SEDs for different viewing angles
    plt.plot(nu_c2, Total2, lw=1, label = r'$\psi_{obs} = '
                 + str(psiDegrees[j]) +'^\circ' + '$')

plt.xscale('log')
plt.yscale('log')
plt.ylabel(r'$\nu j_{\nu}~$[erg cm$^{-3}$ s$^{-1}$ ]', fontsize = 12)
plt.xlabel(r'$\nu~$[Hz]', fontsize = 12)
plt.xlim(1e8, 1e24)
plt.ylim(5e-12, 7e-9)
plt.legend(bbox_to_anchor=(0.99,0.88), loc = 'upper left')
plt.show()
```

Finally, we present a code for the synchrotron polarization calculations.

```
# here, psi_ph represents the viewing angle
# average of F(x)
def fave(nu1, gamma1, gamma2, B, p, psi_ph):
    gamma, delta1, d, sum2 = gamma1, 1.0, 1.1, 0.0
    # integration over the electron energy
    while gamma < gamma2:
        gamma_mid = gamma * ((d + 1)/2)

        nu_psi = 4.2e6 * B* (gamma_mid**2) * (sin(psi_ph))
        x = (nu1/nu_psi)
        Fapprox = 1.42* sqrt(pi/2) *exp(-x) * x**(3/10)
        delta2 = gamma_mid**(-p) * Fapprox * (gamma*(d-1))
        sum2 += delta2
        gamma *= d
    return sum2
#-----------------------------------------------------------------
#-----------------------------------------------------------------
# average of G(x)
def Gave(nu1, gamma1, gamma2, B, p, psi_ph):
    d, delta, gamma, sum = 1.1, 1.0, gamma1, 0.0
    # integration over the electron energy
    while gamma < gamma2:
        gamma_mid = gamma*(d+1)/2

        nu_psi = 4.2e6*B*(gamma_mid**2)*sin(psi_ph)
        x = nu1/nu_psi
        delta = (gamma_mid**(-p)) * x * besselk(2/3, x)
                    * (gamma*(d-1))
        sum += delta
```

```
            gamma *= d
        return sum

psi_ph = array([pi/36,pi/12,pi/7.2,7*pi/36,pi/4,11*pi/36,13*pi/36,5
                                                   *pi/12,17*pi/36])

length = len(psi_ph)
psiDegrees = zeros(length)
for i in range(length):
    psiDegrees[i] = round(degrees(psi_ph[i]),)
#------------------------------------------------------------------

nu_min, nu_max, N = zeros(length), zeros(length), zeros(length)

#------------------------------------------------------------------
for i in range(length):
    nu_min[i] = (1e6 * (gamma1**2) * B) * sin(psi_ph[i])
    nu_max[i] = (1e8 * (gamma2**2) * B) * sin(psi_ph[i])
    dnu = 1.1
    N[i] = log(nu_max[i]/nu_min[i]) / log(dnu) + 2

    # PDs_para = polarization
    nu_para, PDs_para = zeros(int(N[i])), zeros(int(N[i]))
    # F_ave = average F(x), G_ave = average G(x)
    F_ave, G_ave = zeros(int(N[i])), zeros(int(N[i]))
    nu_para[0] = nu_min[i]

    j = 0
    while nu_para[j] < nu_max[i]:
        F_ave[j] = fave(nu_para[j], gamma1, gamma2, B, p, psi_ph[i]
                                         )
        G_ave[j] = Gave(nu_para[j], gamma1, gamma2, B, p, psi_ph[i]
                                         )
        PDs_para = (G_ave/F_ave) * 100
        j += 1
        nu_para[j] = nu_para[j-1] * dnu
    # ploting our polarization
    plt.plot(nu_para, PDs_para,lw=1, label = r'$\psi_{obs} = '
                  + str(psiDegrees[i]) +'^\circ' + '$')

plt.xscale('log')
plt.ylabel(r'$\Pi~[\%]$', fontsize = 12)
plt.xlabel(r'$\nu~$[Hz]', fontsize = 12)
plt.ylim(58, 100)
plt.legend(bbox_to_anchor=(0.85,0.8), loc = 'upper left')
plt.show()
```